

1   **Imaging the voltage of neurons distributed across entire brains of larval zebrafish**

2

3   Zeguan Wang<sup>1,3,10</sup>, Jie Zhang<sup>2,4,10</sup>, Panagiotis Symvoulidis<sup>1,4</sup>, Wei Guo<sup>2,4</sup>, Davy Deng<sup>1,5</sup>, Adam  
4   Amsterdam<sup>1,7</sup>, Lige Zhang<sup>1,3</sup>, Takato Honda<sup>2,4</sup>, Steven Roche<sup>4</sup>, Matthew A. Wilson<sup>2,4</sup>, Edward S.  
5   Boyden<sup>1,3,4,6,7,8,9,\*</sup>

6

7   <sup>1</sup>McGovern Institute for Brain Research, MIT, Cambridge, MA 02139, USA

8   <sup>2</sup>Picower Institute for Learning and Memory, MIT, Cambridge, MA 02139, USA

9   <sup>3</sup>Department of Media Arts and Sciences, MIT, Cambridge, MA 02139, USA

10   <sup>4</sup>Department of Brain and Cognitive Sciences, MIT, Cambridge, MA 02139, USA

11   <sup>5</sup>Harvard-MIT Health Sciences and Technology, Cambridge, MA 02139, USA

12   <sup>6</sup>Department of Biological Engineering, MIT, Cambridge, MA 02139, USA

13   <sup>7</sup>Koch Institute, MIT, Cambridge, MA 02139, USA

14   <sup>8</sup>Howard Hughes Medical Institute, Cambridge, MA 02139, USA

15   <sup>9</sup>Center for Neurobiological Engineering, K. Lisa Yang Center for Bionics at MIT, and Yang Tan Collective,  
16   MIT, Cambridge, MA 02139, USA

17   <sup>10</sup>Co-first authors

18   \*Correspondence: edboyden@mit.edu

19

20

21   **ABSTRACT**

22

23   Neurons interact in networks distributed throughout the brain. Although much effort has focused on whole-  
24   brain calcium imaging, recent advances in genetically encoded voltage indicators (GEVIs) raise the  
25   possibility of imaging voltage of neurons distributed across brains. To achieve this, a microscope must  
26   image at high volumetric rate and signal-to-noise ratio. We present a remote scanning light-sheet  
27   microscope capable of imaging GEVI-expressing neurons distributed throughout entire brains of larval  
28   zebrafish at a volumetric rate of 200.8 Hz. We measured voltage of ~1/3 of the neurons of the brain,

29 distributed throughout. We observed that neurons firing at different times during a sequence were located  
30 at different brain locations, for sequences elicited by a visual stimulus, which mapped onto locations  
31 throughout the optic tectum, as well as during stimulus-independent bursts, which mapped onto locations  
32 in the cerebellum and medulla. Imaging the voltage of neurons distributed across entire brains may open  
33 up frontiers in the fundamental operation of neural systems.

34

35

## 36 INTRODUCTION

37

38 Advances in optical microscopy and genetically encoded calcium indicator (GECI) engineering have  
39 enabled the imaging of calcium, a proxy for neural activity, across the entire brains of larval zebrafish<sup>1–11</sup>,  
40 an important model organism in neuroscience. However, the temporal resolution of whole-brain calcium  
41 imaging, typically around several hundreds of milliseconds<sup>1,7,11</sup>, is insufficient to reveal millisecond-scale  
42 neural processes. Genetically encoded voltage indicators (GEVIs) offer the promise of imaging neural  
43 voltage from many neurons in parallel. Yet, simultaneously meeting all the technical requirements for  
44 imaging GEVI-expressing neurons distributed across entire brains is challenging. The microscope must  
45 achieve temporal resolution comparable with millisecond-scale action potential timing, while having a  
46 three-dimensional field-of-view (3D-FOV, defined as the 3D volume that a microscope can cover)  
47 sufficient to cover the whole larval zebrafish brain, together with high enough spatial resolution to resolve  
48 single cells, and high enough signal fidelity to detect individual action potentials. Optimizing for one goal  
49 often degrades the microscope’s performance in another. We here ask whether a microscope can be  
50 designed to cross the threshold of imaging voltage of neurons distributed across an entire zebrafish brain  
51 by satisfying all these criteria simultaneously.

52 Several imaging techniques hold potential for meeting these requirements, each having their own  
53 advantages and challenges. Light-field microscopy (LFM)<sup>6,12</sup> holds great promise for population-level  
54 voltage imaging<sup>13</sup> due to its high volumetric imaging rate, single-shot acquisition capability, compatibility  
55 with widefield illumination, and simple hardware setup. However, applying LFM to whole-brain voltage  
56 imaging in larval zebrafish presents two key challenges, both stemming from the intrinsic properties of  
57 LFM. The first challenge relates to LFM’s spatial resolution. In voltage imaging, the fluorescent signals  
58 emanate specifically from neurons’ membranes, which appear as cell contours in raw images. These  
59 neuronal contours contact each other in a densely labeled zebrafish brain, necessitating a spatial resolution  
60 much smaller than the neuronal cell body size (3–7  $\mu\text{m}$ )<sup>14</sup> to distinguish individual neurons labeled with

61 GEVIs. Current light-field techniques can achieve at best a lateral resolution of approximately 3  $\mu\text{m}$  when  
62 capturing the entire ~200- $\mu\text{m}$  thick larval zebrafish brain in a single snapshot<sup>15,16</sup>. This limitation comes  
63 from an inherent trade-off in LFM between its spatial resolution and axial field-of-view. While this  
64 resolution can be improved by combining LFM with optical sectioning<sup>17</sup> and galvo scanning<sup>18</sup>, doing so  
65 requires multiple snapshots to capture the whole zebrafish brain, which significantly reduces the volumetric  
66 imaging rate. The second challenge for LFM in voltage imaging is its low signal-to-noise ratio (SNR). The  
67 low SNR is caused by increased shot noise, which results from the mixing of fluorescence signals of  
68 different sample z-planes in raw light-field images. This increased shot noise is inherent and cannot be  
69 efficiently compensated for. To image the entire larval zebrafish brain with dense labeling, we estimate that  
70 LFM will have more than 4 $\times$  shot noise compared to a light-sheet microscope. (A rough estimate is, to  
71 extract signals of a neuron, the baseline fluorescence in LSM contains the fluorescence of no more than two  
72 layers (~6  $\mu\text{m}$  thick per layer, but a neuron may reside at the interface of two adjacent layers, which have a  
73 total thickness of ~12  $\mu\text{m}$ ). As a comparison, the baseline fluorescence in LFM contains superimposed  
74 fluorescence from the whole brain volume (~200  $\mu\text{m}$  thick), resulting in shot noise that is at least  
75  $\sqrt{200/12} \sim 4.08$  times of that in LSM.)

76 Light-sheet microscopy (LSM) is an another promising technique for volumetric fluorescence imaging, as  
77 it specifically excites and efficiently images fluorophores in a two-dimensional (2D) focal plane, thus  
78 offering high throughput, good optical sectioning capability and low phototoxicity, while maintaining good  
79 spatial resolution (i.e., down to 0.3  $\mu\text{m}$ , lateral)<sup>19–22</sup>. Using conventional LSM, whole-brain, cellular-  
80 resolution calcium imaging has been achieved in larval zebrafish at a volumetric imaging rate of 0.8–3 Hz<sup>1,7</sup>.  
81 However, it is difficult to improve the speed of conventional LSM to a volume rate that can be used for  
82 voltage imaging, while maintaining the 3D-FOV required to image a whole larval zebrafish brain  
83 (~900 $\times$ 370 $\times$ 200  $\mu\text{m}^3$ ) at cellular resolution<sup>19,21,22</sup>. This difficulty arises from two factors: (1) it is  
84 challenging to enhance the scanning speed of the image plane, and (2) cameras exhibit limited frame rates  
85 at the necessary camera field of view (C-FOV, defined as the number of row and column pixels captured  
86 in one frame)<sup>19,22</sup>. Regarding the first constraint: in conventional LSM, a 3-D sample is scanned plane by  
87 plane through physical translation of the detection objective. But such strategies are difficult to adapt for  
88 scanning thick biological samples (e.g., >200  $\mu\text{m}$ ) at high volume rates (e.g., >100 Hz). This is due to the  
89 scanning range and speed limitations of scanners designed for moving objective lenses. The fastest  
90 commercial objective scanner (PI P-726) can run at 560 Hz, but it can only scan across a 100- $\mu\text{m}$  range<sup>23</sup>.  
91 Other objective scanners can scan across a longer range (up to several mm), but not at a frequency >100  
92 Hz<sup>24</sup>. Regarding the second constraint: the speed of LSM is limited by the camera's acquisition rate. The  
93 volume rate of LSM can be calculated as the camera frame rate divided by the number of 2-D image planes

94 of the volume. Current state-of-the-art cameras (e.g., Hamamatsu ORCA Flash, Andor Zyla) have full-  
95 speed pixel rates of  $\sim 0.5 \times 10^9$  pixels per second. When imaging a large 3D-FOV, e.g., the whole larval  
96 zebrafish brain, such cameras can provide a frame rate up to 400 Hz (assuming a  $512 \times 1280$ -pixel C-FOV),  
97 which translates to a maximum volume rate of only 10-15 Hz.

98 Many strategies have been proposed to enhance the scanning speed of LSM<sup>25-35</sup>. One is remote  
99 refocusing<sup>25,26</sup>, which rapidly shifts the system's focal plane at a remote site using a tunable lens<sup>27</sup>,  
100 translational tertiary objective lens<sup>36</sup>, or translational mirror<sup>28,29</sup>. However, the additional aberration from  
101 tunable lenses limits the system's numerical aperture (NA) and two-dimensional field-of-view (2D-FOV,  
102 defined as the area a microscope can image in a single two-dimensional focal plane). The numerical aperture  
103 of reported tunable lens-based LSM systems is limited to 0.3 NA for a  $600\text{-}\mu\text{m}$  diameter circular ( $\Phi 600$   
104  $\mu\text{m}^2$ ) 2D-FOV<sup>27</sup>. On the other hand, spherical aberration from refocusing can be eliminated using a  
105 translational tertiary objective lens<sup>36</sup> or a translational mirror<sup>25,26</sup> at a remote site. However, scanning the  
106 tertiary objective lens has the same scanning range and speed limitations as encountered in conventional  
107 LSM; regarding the remote mirror strategy, previous studies used commercial mirrors that are several grams  
108 in weight and actuators that are designed for heavier loads (such as objective lenses), and thus achieved  
109  $< 100$ -Hz scanning rates and  $< 100\text{-}\mu\text{m}$  scanning range<sup>28,29</sup>. In addition, reported lateral 2D-FOVs in remote  
110 mirror-based LSM configurations were  $< \Phi 200 \mu\text{m}^2$ , perhaps due to high magnification ratios and system  
111 aberrations<sup>28,29</sup>.

112 Besides remote refocusing, a recently developed technique, termed swept confocally-aligned planar  
113 excitation microscopy (SCAPE)<sup>37,38</sup> or oblique plane microscopy (OPM)<sup>30-35</sup>, can also relieve the scan rate  
114 bottleneck of LSM. SCAPE and OPM laterally sweep an oblique-aligned focal plane using remote galvo  
115 or polygon mirror scanners, allowing volume scan rates up to the maximum scan rates of these mirror  
116 scanners. SCAPE 2.0<sup>37</sup> can scan a  $197 \times 293 \times 78 \mu\text{m}^3$  volume at a high rate of 321 volumes per second  
117 (VPS), or a  $345 \times 278 \times 155 \mu\text{m}^3$  volume at 100 VPS. But, the oblique alignment between the secondary and  
118 the tertiary objectives has limited the effective NA to 0.35, which means far ( $\sim 10\times$ ) less light collection  
119 than, e.g., a 1.0 NA lens. This makes whole-brain voltage imaging challenging, given that voltage imaging  
120 is far lower in signal-to-noise (SNR) than calcium imaging (indeed, as will be seen in this paper, a  $10\times$   
121 reduction in light collection for the currently proposed microscope would bring SNR for many neurons  
122 below acceptable levels). To increase effective NA, several new OPM configurations were proposed  
123 recently, where water chambers<sup>30</sup> and customized objectives<sup>31,32</sup> were used to reduce the misalignment  
124 angle between the light cones of the secondary and the tertiary objectives. These strategies have enhanced  
125 effective NAs up to the NAs of the detection objectives (e.g., NA = 1). While these OPMs possess high NA  
126 and the potential to scan volumes at high speeds, the light refraction on the secondary objective's oblique

127 image plane and the oblique tertiary objectives cause extra aberrations that reduce the diffraction limited  
128 2D-FOV. Recently, a specifically designed, glass-tipped tertiary objective lens<sup>31</sup> enabled an 800×420μm<sup>2</sup>  
129 2D-FOV at NA=0.97 in OPM. Theoretically, this SCAPE/OPM configuration could be further adapted for  
130 imaging the voltage across whole larval zebrafish brains, given sufficient optimization is made.

131 We here optimized the translational mirror-based remote refocusing strategy<sup>25,26,28,29</sup> to enhance the volume  
132 scan rate of light-sheet microscopy, using a lightweight silver-coated mirror (0.01 g), and a piezo bender  
133 actuator capable of large travel distance (270 μm), high resonant frequency (930 Hz), and sub-millisecond  
134 response time. We chose the remote refocusing configuration over SCAPE/OPM because this configuration  
135 theoretically promised less aberration, and samples the fish brain in a way closer to conventional LSMs  
136 1,7,39–41. Using optical simulation, we designed an optimal choice and arrangement of tube lenses and other  
137 optical components to enable low aberrations and large 3D-FOV simultaneously. We chose a camera  
138 capable of balancing speed, noise, and resolution and used it in a distributed planar imaging<sup>42</sup> strategy  
139 configuration. We further showed that incorporating a second remote refocusing module enabled our  
140 microscope to efficiently utilize emission light of all polarization directions (Fig. S1, Fig. S2), achieving  
141 light efficiency comparable to, or exceeding (because SCAPE/OPM requires an extra pair of scan lenses  
142 between the detection and the remote objectives), that of the SCAPE/OPM configuration equipped with a  
143 glass-tipped tertiary objective<sup>31</sup>. With our microscope, we could capture the voltage activity of neurons  
144 distributed across the brain of a larval zebrafish at 200.8 Hz. Using a 5 day post fertilization (dpf) zebrafish  
145 expressing Positron2-Kv pan-neuronally, we found that we could image ~85% of the zebrafish brain, with  
146 the remainder either shadowed by the eye, or scattering light – problems not unique to voltage imaging, but  
147 that also hold for light-sheet calcium imaging<sup>1</sup>. In this paper, we fully analyzed the imaging data of four  
148 fish (n=4, referred as Fish A – D). We identified 17,700, 25,552, 25,464, and 17,419 regions-of-interest  
149 (ROIs) corresponding to putative neurons in Fish A – D using a custom trained deep learning-based cell  
150 segmentation model based on Cellpose 3.0 (see Methods). The maximum segmented ROI number in our  
151 data reaches ~1/3 of the estimated neurons number (~78,000) in a 7-dpf fish<sup>43</sup>.

152 We next sought to explore the kinds of observations and hypotheses that could be generated using our  
153 technology. We do not intend for this to be a full scientific study, but instead to indicate the kinds of  
154 scientific observations one could make using our technology, which could be followed upon with further  
155 replicates and experiments in the context of a conventional scientific study. We exposed the fish to a visual  
156 stimulus, of UV light, and found a group of neurons that were active shortly following stimulus onset. After  
157 sorting the neurons by the timing of their peak firing rate, we observed a correlation between the timing of  
158 each neuron's peak firing rate and its location in the brain; specifically, neurons near the lateral sides of the  
159 optic tectum (OT) fired earlier than those located at the medial locations of the OT (in Fish A, B, D, both

160 side of OT, Fish C, one side of OT). In addition, we identified another group of neurons that exhibited  
161 repeated burst activity, which occurred independent of the visual stimulus. This group of neurons was  
162 found in the cerebellum and medulla oblongata. After analyzing individual neurons' activity in each burst,  
163 we observed temporal sequential patterns of neural firing; bursts were not precisely synchronized across  
164 neurons, but occurred sequentially across neurons (in all four fish). In two of the four fully analyzed fish  
165 (Fish B and C), we found a putative physical cluster of neurons at the ventral side of the medulla oblongata  
166 that consistently fired at the beginning of bursts in this group. These findings demonstrated the capabilities  
167 of our technique to study large-scale, millisecond-level neural processes in the brain. The results were from  
168 four fish, and we do not intend these findings to be taken as scientific results; rather, our emphasis was to  
169 show the kind of neuroscience that one could do, with the technology presented here. Imaging the voltage  
170 of neurons distributed across whole brains may be useful for generating many new kinds of hypothesis, that  
171 could be tested by conventional neuroscience strategies, in the future.

172

173

## 174 RESULTS

175

### 176 Rationale for the microscope design

177 Our microscope was optimized for 3-D, large-volume, high-speed, high-resolution voltage imaging through  
178 several complementary efforts (**Fig. 1a**). We optimized the translational mirror-based remote refocusing  
179 strategy<sup>25,26,28,29</sup> to enhance the volume scan rate of light-sheet microscopy. Different from previous work,  
180 we customized a lightweight silver-coated mirror that is only 0.01 g in weight, and scanned it using a piezo  
181 bender actuator that has a large travel distance (270  $\mu\text{m}$ ), high resonant frequency (930 Hz), and sub-  
182 millisecond response time. The lightweight mirror and fast piezo actuator allowed us to scan a 200- $\mu\text{m}$   
183 axial (z-axis) range at the sample at up to 300-Hz. To reduce aberrations and enhance the 3D-FOV in our  
184 microscope system, we simulated the aberrations of different optical designs. We used our results to find  
185 an optimal configuration that minimized the aberrations contributed by the remaining optical elements in  
186 the detection light path, such as tube lenses, a polarized beam splitter (PBS), and relay lenses. We borrowed  
187 the concept from earlier OPM work<sup>31</sup> to construct tube lenses with desired parameters using commercially  
188 available lenses. By simulating various combinations of these custom tube lens assemblies with other  
189 elements in our system, we identified a configuration that supported 1.0 NA and a  $\Phi 900 \times 200 \mu\text{m}^3$  3D-FOV,  
190 with 0.15  $\lambda$  (at 550 nm, root mean square) wavefront error at the 3D-FOV edge.

Having established an optical design, we next turned to the camera. The spatial resolution and the volume scan rate of the LSM are determined, in part, by the camera's frame rate and C-FOV. The C-FOV should have a sufficient number of pixels (e.g., 512×1280) to sample the 2D-FOV of the entire zebrafish brain, with an effective pixel size smaller than a neuron soma. The camera's frame rate determines the LSM's volume scan rate and z-plane step size. For instance, with a fixed camera frame rate of 6000 Hz, an LSM can scan at 300 VPS, capturing 20 z-planes per volume (200  $\mu\text{m}$  thick), with a 10  $\mu\text{m}$  z-sampling step size. Alternatively, at the same frame rate, the LSM can scan at 200 VPS, acquiring 30 z-planes per volume, with a 6.7  $\mu\text{m}$  z-sampling step size. A higher camera frame rate results in a higher VPS, more z-planes per volume, and a smaller z-sampling step size. The sCMOS cameras commonly used by the scientific community (such as the Hamamatsu ORCA Flash and Andor Zyla) can only reach a frame rate of 400 Hz for a C-FOV of 512×1280, which can only support the scan of 2 z-planes at 200 VPS. While other cameras, such as the Lambert HiCAM Fluo<sup>44</sup> and the Teledyne Kinetix<sup>45</sup> can reach a speed of 3000-4000 Hz, the HiCAM Fluo has lower than desired quantum efficiency (QE: 30 – 50%), which affects pixel sensitivity to detecting fluorescence photons; Kinetix pixels have low full well capacity (~200 e-), which is insufficient for our application, where the brightest pixels may generate up to 2000 electrons per frame at the illumination powers needed for acceptable SNR. Thus, we searched for a camera that could overcome these limits. Continued advancements in CMOS technology have resulted in the availability of commercial image sensors that meet the speed and noise specifications for our microscopy system. We used the Gpixel GSPRINT4502 image sensor that supports a high pixel rate of 4.37 GHz in 10-bit mode, with a full well capacity of 7.4k e-, a readout noise of ~7e-, and a QE of 60% at 550 nm. This sensor enables us to capture a C-FOV of 512×1280 pixels at a speed of 3900 FPS, effectively covering the entire brain of a larval zebrafish. To further boost imaging speed, we implemented the distributed planar imaging strategy<sup>42</sup>, dividing a 2D-FOV into multiple smaller 2D-FOVs recorded separately using multiple image sensors. Utilizing two GSPRINT4502 image sensors in a dual-camera system, we can improve the frame rate to 7300 Hz for a C-FOV of 512×1280 pixels. This enhancement, in principle, can enable the LSM to scan 30 image planes at a maximum volume rate of 243 VPS.

217

## 218 **Implementation of the microscope design**

219 We devised a high-speed remote scanning light-sheet microscope to address the technical demands of  
220 whole-brain distributed voltage imaging in larval zebrafish (**Fig. 1**). This innovation caters to the needs of  
221 imaging a whole zebrafish brain volume (~900×370×200  $\mu\text{m}^3$ ) at a volume rate of 200.8 Hz, and ensures  
222 1.46- $\mu\text{m}$  (effective pixel size limited; effective pixel size: 0.73  $\mu\text{m}$ , *effective pixel size =*  
223 
$$\frac{\text{camera pixel size}}{\text{system magnification ratio}} = \frac{4.5}{6.16} \mu\text{m}$$
) lateral and 11.7- $\mu\text{m}$  (z sampling step size limited, z sampling step

size: 5.86  $\mu\text{m}$ ) axial resolution across the whole 3D-FOV. To enhance the volumetric imaging rate, we leveraged the concept of remote refocusing<sup>25,26</sup>. We used a piezo bender scanner (270- $\mu\text{m}$  scan range, 930-Hz resonant frequency) to scan a lightweight mirror ( $\sim 0.01 \text{ g}$ ) at a remote site (**Fig. 1a**) in the detection arm of our light-sheet microscope. This remote scanning design facilitates rapid scanning of the microscope's focal plane along the zebrafish brain's dorsal-ventral (z) axis. It avoids disturbance of the sample potentially caused by rapidly translating the detection objective lens. In our microscope (**Fig. 1a**), the sample is excited by a laterally illuminated light sheet (515 nm wavelength) that was generated using a Powell lens and scanned using a galvo mirror (see **Methods** section, **Fig. S17**). The emitted fluorescence from the sample was collected by a high-NA (water immersion, NA=1.0) detection objective lens. An upright, isotropically magnified image of the sample was generated at a remote location using a remote objective lens (air, NA=0.8). This image was then reflected by a lightweight mirror, essentially repurposing the remote objective as a virtual tertiary lens for reimaging. By swiftly actuating the lightweight mirror ( $\sim 0.01 \text{ g}$ ) with a piezo bender scanner—akin to scanning the tertiary virtual lens—we achieved fast scanning of the focal plane across a 200- $\mu\text{m}$  axial range at rates of up to 300 Hz. The magnification ratio between the remote image and the sample was designed to be 1.33 to match the ratio between refractive indices in the sample space (water) and in the remote image space (air). This magnification ratio-refractive index ratio match ( $\text{Mag}_{\text{remote}} = n_{\text{sample}}/n_{\text{remote}}$ ) allows eliminating the spherical aberrations resulted from refocusing<sup>25,26</sup>.

As the emitted fluorescence passes through a polarized beam splitter (PBS) twice in our setup, emitted fluorescence of a particular polarization ( $\sim 50\%$  assuming the emitted fluorescence is fully unpolarized) will be lost. Although we did not find the image brightness to be limiting in our experiments, enhanced light efficiency is unquestionably beneficial as it would support higher SNR, reduced excitation power, and slower photobleaching. In this paper, we demonstrated an approach to restore the lost fluorescence by installing a secondary remote scanning module that is identical to the first module (i.e., a remote objective lens, a quarter wave plate, and a piezo-driven remote mirror) at the other port of the PBS and driving the secondary piezo scanner in synchrony with the first piezo scanner (**Fig. 1a, Methods**). The images formed from each of the two remote scanning modules could be aligned on the image sensor with sub-pixel precision across a 200- $\mu\text{m}$  thick volume (**Fig. S1, Methods**). When imaging the neural voltage in zebrafish brains, this dual remote scanning module approach increased the fluorescence intensity by 75% (**Fig. S2**, see **Supplementary Table 2** for the imaging conditions for each dataset). The enhancement in fluorescence intensity was less than 100% because the emission light of GEVIs was partially polarized due to the linearly polarized excitation light (this is because linearly polarized light can more efficiently excite transition dipoles of GEVI fluorophores that align with the excitation light's polarization axis<sup>46</sup>), and we oriented the PBS to guide the emission light with the same polarization axis as the excitation light to the first remote

257 scanning module. In other words, in our voltage imaging experiments using a single remote scanning  
258 module, more than 50% (1/1.75 ~ 57%) emission light was already utilized at the polarized beam splitter.

259 Although remote refocusing theoretically does not introduce aberration, with so many high NA optical  
260 elements in the detection path, accumulated aberrations from each optical element could reduce the  
261 effective 2D-FOV by decreasing the spatial resolution at the 2D-FOV edges, particularly along the rostral-  
262 caudal (x) axis of the zebrafish brain, which spans ~900  $\mu\text{m}$ . To obtain a sufficient 3D-FOV with low  
263 aberration for whole-brain cellular-resolution imaging, we used Zemax to simulate the aberrations in a  
264  $\Phi 900 \times 200 \mu\text{m}^3$  3D-FOV of a series of configurations with various parameters and optical elements. Due  
265 to the unavailability of Zemax models for the detection and the remote objective lenses, in this simulation,  
266 we only evaluated the aberrations from all the remaining optical elements in the detection path, including  
267 three tube lenses, a polarized beam splitter, and a relay lens pair. The relay lens pair was used to reduce the  
268 system magnification ratio to ~6.16 $\times$  so that the whole zebrafish brain could fit into the C-FOV on the  
269 image sensor ( $2.30 \times 5.76 \text{ mm}^2$ , 512 $\times$ 1280 pixels). The relay pair was also used to relay the split half images  
270 onto the two cameras in the distributed planar imaging system, as described in the “**Rationale for the**  
271 **microscope design**” section. According to our simulation results, we found that proper choice of tube lenses  
272 in the detection path is important to reduce system aberrations. We identified an optimal microscope  
273 configuration that achieved a diffraction-limited  $\Phi 900 \times 200 \mu\text{m}^3$  3D-FOV at a high NA of 1.0, with the  
274 wavefront error at the 3D-FOV edge to be 0.15  $\lambda$  RMS (at 550 nm). Although the detection and the remote  
275 objective lenses were not considered in our simulation, the identified configuration can still efficiently  
276 reduce the aberrations in our real system. This is because the aberration in an imaging system is the  
277 summation of the aberration contributed by each optical element in the system<sup>47</sup>. Because commercial tube  
278 lenses cannot fully satisfy our parameter requirements (e.g., focal plane and aperture), we borrowed the  
279 idea from previous OPM work<sup>31,48</sup> and customized several tube lenses with desired parameters by  
280 assembling multiple commercially available lenses. According to our tests, these engineering efforts  
281 yielded a  $\Phi 900 \times 200 \mu\text{m}^3$  three-dimensional volume with spatial resolutions that are only limited by the  
282 lateral effective pixel size (0.73  $\mu\text{m}$ ) and the z sampling step size (5.86  $\mu\text{m}$ ) (**Fig. 1b**, **Fig. S3**). The 6.16 $\times$   
283 magnification ratio was chosen to keep a balance between the camera frame and the spatial resolution: with  
284 this magnification ratio, the whole zebrafish brain can fit into a 512 $\times$ 1280 pixel C-FOV to allow the camera  
285 to run at high frame rates (in our case, up to 7300 FPS); on the other hand, the 0.73- $\mu\text{m}$  effective pixel size  
286 corresponding to this magnification ratio is ~1/9 of the average neuron soma diameter (6.62  $\mu\text{m}^1$ ) in larval  
287 zebrafish, which is sufficiently small so that it will not be a bottleneck for resolving single cells. Increasing  
288 the system magnification ratio will increase the spatial resolution but will also increase the C-FOV and  
289 reduce the camera frame rate.

We empirically characterized the system resolution by imaging the 3-D point spread functions (PSFs) of 200-nm diameter red fluorescent beads (emission wavelength = 605 nm) that were randomly distributed in 1% agarose. We did not find <500 nm diameter beads with 550-nm emission wavelength to mimic the emitted fluorescence of the Positron<sub>525</sub>-Kv indicator that we used (see below for details of voltage indicator choice, in “**Performance of the microscope**”). We chose to image red (605 nm emission) beads instead of green beads (515 nm emission) because longer emission wavelengths, which enlarge the PSF, avoid overestimation of the microscope’s resolution, and because green beads cannot be efficiently excited by our light sheet (515 nm wavelength). To accurately reflect the effective resolution affected by motion blur due to continuous translation of the focal plane during exposure, we imaged the PSF while the microscope continuously scanned across a 206-μm axial range at 200.8 Hz. Due to our microscope’s low magnification ratio (6.16×), the lateral effective pixel size (0.73 μm) could not adequately sample PSFs in the x and y axes (here x-axis is defined as the axis in the raw images that roughly aligns with the rostral-caudal axis of the fish brain, and y-axis is defined as the axis in the raw images that roughly aligns with the medial-lateral axis in the fish brain. Here we say “roughly aligns” because the fish’s brain can be slightly rotated in the raw images due to imperfect embedding.). This sub-optimal sampling can be seen in **Fig. 1b**, where some x-y PSFs were sampled as a single bright pixel (**Fig. 1b**, cyan arrows). To measure the full-widths-at-half-maximum (FWHMs) of the lateral PSF (x-y), we fitted the PSF using a 2-D Gaussian function (**Fig. S3a**). The x-y position and the shape of the Gaussian function were iteratively updated until the correlation was maximized between the measured lateral PSF and the 2-D Gaussian function image that was down-sampled to the same 0.73-μm effective pixel size (**Fig. S3a**). Then lateral FWHMs of the PSF were measured as the FWHMs of the fitted Gaussian function. To measure the axial (z-axis, defined as the axis perpendicular to the microscope’s focal plane. Z-axis roughly aligns with the ventral-dorsal axis in the fish brain.) FWHM of the PSF, we used a one-dimensional dual-Gaussian function to fit the axial line profile that contained the brightest pixel of the 3-D PSF. Then, the FWHM was measured on the fitted profile (**Fig. S3**). According to our measurements, a lateral FWHM of ~1 μm and an axial FWHM of ~3.5 μm of the PSF were maintained across the full measured 3D-FOV of  $\Phi 900 \times 200 \mu\text{m}^3$  (**Fig. S3b-f**). These values are larger than the theoretical FWHMs (0.37 μm lateral and 1.21 μm axial). This difference comes from the motion blur of continuous scanning and the lateral effective pixel size: (1) when imaging the PSF, the microscope’s focal plane continuously translated across ~3 μm during the exposure of each frame, so that each measured pixel was blurred as an average of the intensity of the real PSF across a ~3-μm axial range, significantly increasing the 3-D size of the measured PSF. (2) The lateral effective pixel size (0.73 μm) in the images is larger than the real PSF’s lateral (xy) size. Therefore, each pixel in the images acted as an averaging window applied to the real PSF, which smoothed the intensity peak of the real PSF and lowered the half maximum threshold to measure FWHMs, increasing the FWHM values. Nevertheless, considering the 0.73-μm lateral

324 and 5-6  $\mu\text{m}$  axial (z) sampling step size, our system maintains spatial resolution that is only bounded by  
325 effective pixel size and the z sampling step size across a  $\Phi 900 \times 200 \mu\text{m}^3$  3D-FOV. According to Nyquist's  
326 theorem, the 0.73  $\mu\text{m}$  effective pixel size in our system corresponds to a lateral resolution of 1.46  $\mu\text{m}$ ,  
327 around one-fifth of the average diameter (6.62  $\mu\text{m}^1$ ) of neuron somas in zebrafish.

328 The acquisition system employs a distributed planar imaging strategy<sup>42</sup> utilizing two Gpixel GSPRINT4502  
329 image sensors. As commercially available cameras incorporating this newly available image sensor were  
330 lacking **when we started the project**, we designed a custom camera system using this image sensor (**Fig.**  
331 **S4**). This camera achieved a spatial resolution of  $512 \times 1024$  with 10-bit output at 3900 FPS. This capability  
332 allowed us to conduct prototype measurements for screening GEVI indicators, establish microscope control  
333 systems, and perform volumetric imaging of the zebrafish brain with 15 imaging layers at 200 VPS.  
334 However, the main drawback of our custom camera was its size, a consequence of utilizing a PCIe link that  
335 requires the PC to be in close proximity to the camera (**Fig. S4**). The large size posed challenges for its  
336 integration into a distributed planar imaging setup (**Fig. S5**). While the camera's size could be reduced by  
337 adopting existing PCIe cable connectors, such as the Molex iPass connector system, this would necessitate  
338 additional time for design modifications. As an alternative, we opted for a commercial camera (Ximea  
339 CB024MG-GP-X8G3), which became available during the construction of the distributed planar imaging  
340 system. Using two cameras, the distributed planar imaging system achieved a spatial resolution of  
341  $512 \times 1280$  at 7300 FPS. This allows our LSM to scan 30 image planes at a maximum volume rate of 243  
342 volumes per second (VPS).

343 To synchronously drive all hardware devices for rapid volumetric imaging at 200.8 Hz, we developed a  
344 high-speed control system with 4- $\mu\text{s}$  temporal precision, along with image-guided calibration and tuning  
345 pipelines, to align and synchronize the positions of the remote translational mirror and the light sheet.  
346 Considering the high scanning rate of our system, we used open-loop control. To compensate for the  
347 hysteresis of the piezo scanner and control its motion at high precision, we designed and built a  $20 \times$   
348 magnification, line-camera imaging system that could continuously measure the position of the piezo  
349 scanner at 70000 Hz and 350 nm precision. The measured scanning positions of the piezo scanner were  
350 used as feedback to adjust the piezo's control signals, which were generated using a real-time FPGA I/O  
351 device. Following this calibration and tuning pipeline, we drove the piezo to scan across a 113  $\mu\text{m}$  range  
352 (170  $\mu\text{m}$  at the sample) at 200.8 Hz and achieved a displacement curve over time that resembled a triangle  
353 wave (**Fig. 1c**). More specifically, this displacement curve was the superposition of a series of sinusoidal  
354 waves with 200.8-Hz, 602.4-Hz, and 1,004-Hz frequencies, which are the first, second, and third sinusoidal  
355 terms in the Fourier transform of the triangle wave. Compared to a sinusoidal wave, this displacement curve  
356 of the piezo allowed more even sampling of z-planes in time and more efficient use of the camera speed.

357 After calibrating the motion of the piezo scanner, we adjusted the control signals of the galvo mirror to  
358 synchronize the light sheet with the scanning focal plane. To do so, we imaged a 3-D agarose sample that  
359 contained 500-nm diameter fluorescent beads. During continuous high-speed scanning, we pulsed the light  
360 sheet in synchrony with the scanning cycles to excite and image only a specific z-plane in real-time. Then  
361 the control signal of the galvo was adjusted until the image was focused. This adjustment process was  
362 iteratively repeated for different z-planes until all z-planes were in focus during scanning.

363 Each scan cycle consists of both an upward and a downward scanning phase, corresponding to the rising  
364 and falling slopes in the displacement curve of the piezo scanner (**Fig. 1c**). To utilize the camera speed at  
365 both scanning phases, we exploited an interleaved sampling strategy to image z-planes in a volume. In a  
366 volume scan, we imaged 30 z-planes that were evenly spaced from  $z_1 = -85 \mu\text{m}$  to  $z_{30} = 85 \mu\text{m}$ . During the  
367 upward phase, we imaged z-planes at  $z_2 = -79.14 \mu\text{m}$ ,  $z_4 = -67.41 \mu\text{m}$ , ...,  $z_{30} = 85 \mu\text{m}$ , while during the  
368 downward phase, we imaged z-planes at  $z_1 = -85 \mu\text{m}$ ,  $z_3 = -73.28 \mu\text{m}$ , ...,  $z_{29} = 79.14 \mu\text{m}$  (**Fig. 1c**). To  
369 minimize motion blur in the image caused by continuous translation of the focal plane during exposure, we  
370 flashed the light sheet (43 mW within the flash period) for 40  $\mu\text{s}$  to capture each frame. During this 40- $\mu\text{s}$   
371 period, the focal plane traveled across an axial distance of approximately 2.7  $\mu\text{m}$ , about half of the thickness  
372 of the light sheet (measured to be  $5.3 \pm 1.4 \mu\text{m}$ , full width at half maximum, mean  $\pm$  standard deviation,  
373 across 400  $\mu\text{m}$  in y-axis). The resulting volumetric microscopy system thus combines high volume rate,  
374 large 3D-FOV, and high spatial resolution.

375

### 376 **Performance of the microscope**

377 To demonstrate the utility of our microscope, we sought to choose a voltage indicator with sufficient  
378 performance to explore the kinds of insights that could be derived. There is, admittedly, no perfect voltage  
379 indicator at the current moment, and each voltage indicator incurs specific tradeoffs and sacrifices. For  
380 example, one voltage indicator may be very bright or exhibit high SNR, but the kinetics may be challenging  
381 to capture. Another may have more ideal kinetics but be too dim. Acknowledging that voltage indicators  
382 are improving rapidly, and thus, the best voltage indicator by the time this paper is written might be much  
383 better than the ones available today, we focused our attention on the question of whether whole-brain  
384 voltage imaging was crossing the threshold of being feasible, rather than focusing on any one voltage  
385 indicator. Specifically, we wanted to know if whole-brain voltage imaging could reveal patterns of neural  
386 activity that one could not observe with whole-brain calcium imaging, which might provoke new  
387 hypotheses of neural computation.

388 Using our microscope, we imaged the voltage of neurons distributed across the entire brains of 5-6 day-  
389 post-fertilization (dpf) larval zebrafish that have pan-neuronal expression of the Positron2-Kv<sup>49</sup> voltage  
390 indicator (**Fig. 1d**, **Fig. 2**). We chose to use Positron2-Kv after we tested and compared five different  
391 voltage indicators in larval zebrafish. The five indicators were ASAP3-Kv<sup>50</sup>, Voltron2-Kv<sup>51</sup>, Ace-mNeon2-  
392 Kv<sup>52</sup>, pAce-Kv<sup>52</sup>, and Positron2-Kv<sup>49</sup>. We first transiently expressed the five indicators in larval zebrafish  
393 using embryonic micro-injection<sup>53</sup>. We imaged their spontaneous activity and compared their SNRs per  
394 action potential ( $SNR_{AP}$ ), which were calculated as the ratio between the fluorescence intensity change per  
395 action potential and the shot noise at the spike peak per neuron per frame ( $SNR_{AP} = (N_{peak} - N_0) /$   
396  $\sqrt{N_{peak}}$ ,  $N_{peak}$  the detected photon number at the spike peak per neuron per frame,  $N_0$  the detected photon  
397 number at the resting potential right before the measured spike per neuron per frame; these peaks and resting  
398 potentials were estimated by eye). We observed that, compared to ASAP3-Kv, Positron2-Kv and Voltron2-  
399 Kv exhibited  $\sim 10\times$  brightness, while Ace-mNeon2-Kv and pAce-Kv showed  $\sim 5\times$  brightness. This  
400 brightness difference might result from a difference in molecular brightness when expressed in the zebrafish  
401 milieu, or a difference in expression density on zebrafish neural membranes. We found that Voltron2-Kv  
402 and Positron2-Kv exhibited the highest SNRs among all tested indicators, in the zebrafish that we made,  
403  $\sim 1.4\times$  of those of Ace-mNeon2-Kv and pAce-Kv, and  $\sim 2.4\times$  of that of ASAP3-Kv. We then constructed  
404 transgenic zebrafish lines with pan-neuronal expression of Voltron2-Kv and Positron2-Kv using the Tol2  
405 transposon system<sup>53</sup>. We used the Gal4/UAS system<sup>54</sup> to express Voltron2-Kv and Positron2-Kv, with the  
406 Gal4 gene driven by the pan-neuronal promoter HuC<sup>55</sup>. For each of the Positron2-Kv and Voltron2-Kv  
407 indicators, we made one fish line. We didn't observe much voltage activity in the Voltron2-Kv fish line we  
408 made, which could have been due to any number of factors, many of which have nothing to do with  
409 Voltron2 itself; given that our goal was simply to probe whether our microscope was capable of imaging  
410 voltage in neurons distributed across an entire zebrafish brain, we used the Positron2-Kv fish line in our  
411 experiments, as a somewhat arbitrary choice.

412 In our transgenic Positron2-Kv fish, we saw well localized fluorescence on the membranes of individual  
413 neurons in the brain (**Fig. 2a, b**). Specifically, neurons on the ventral side of the brain (**Fig. 2a**,  $z=-108\ \mu m$ ,  
414  $-136\ \mu m$ ) were densely packed, as expected for pan-neuronal expression. However, on the dorsal side of  
415 the brain, we sometimes observed dark areas where neurons seemed to be unlabeled (**Fig. 2a**,  $z=-23\ \mu m$ ,  $-51\ \mu m$ ,  $-79\ \mu m$ , cyan arrows). These unlabeled areas could have resulted from several possibilities. First,  
416 the transgenes might not have been inserted at optimal locations in the zebrafish genome, so their expression  
417 could have been suppressed in specific types of neurons. To remedy this, in the future, we could perform  
418 more embryonic micro-injections to generate a large pool of larval zebrafish with random transgenic  
419 insertions in the genome, and screen for the fish with the most pan-neuronal expression. Second, because

the Positron2-Kv indicators need to be stained with a chemical dye solution to gain fluorescence<sup>49,51,56</sup>, indicator proteins synthesized during the period (~4 hours in our experiments) between the staining and the light-sheet imaging would not be labeled with dye. This period is needed to incubate the fish in fresh water to remove excess dye molecules that did not bind voltage indicator proteins and to mount the fish in a customized water chamber for imaging. Third, in transgenic larval zebrafish, fluorescent reporter genes regulated by tandem UAS copies often display variable expression, likely as a result of transcriptional silencing mediated by DNA methylation<sup>57</sup>. We chose to use the Gal4/UAS expression system due to its high expression strength<sup>58,59</sup>, but this might also make our transgenic Positron2-Kv fish susceptible to this silencing effect. As a comparison to the Gal4/UAS promoter, we tried directly expressing Positron2-Kv using a HuC promotor. We found that directly expressing Positron2-Kv using the HuC promoter, compared to using HuC:Gal4 and tandem UAS, did result in more pan-neuronal expression, but this also decreased fluorescent brightness (**Fig. S29**, showing a comparison of confocal images of a 6 day-post-fertilization (dpf) F2 generation Tg(HuC:Gal4; 2xUAS:Positron2-Kv) fish and a 5-dpf F1 generation Tg(HuC:Positron2-Kv) fish), potentially making brain-wide voltage imaging more difficult. The images of the two fish were acquired using the same microscope settings. Compared with the Tg(HuC:Positron2-Kv) fish, the Tg(HuC:Gal4; 2xUAS:Positron2-Kv) fish had higher brightness (~1.1× averaged over the whole brain, ~1.7× averaged over the whole optic tectum (OT), and ~2.6× averaged over the whole habenula (HB)). The Tg(HuC:Gal4; 2xUAS:Positron2-Kv) fish brain also showed more varied levels of expression across different brain regions. (Please note, these were not systematic explorations: we did not control for precise fish age or generation, and examined only one fish for each type. We did not image the Tg(HuC:Positron2-Kv) fish under our light-sheet microscope, either. The Tg(HuC:Positron2-Kv) fish could potentially be used in future experiments to improve the number of imaged neurons, given that our modified microscope's light efficiency was enhanced in a way that could make up for reduced neuron brightness (we demonstrated a 75% improvement in light efficiency using dual remote mirrors in the modified microscope, see **Fig. S1**, **Fig. S2**). In any case, fish transgenic line generation is an ongoing area of innovation for the entire fish community, and as that field continues improving, so will the performance of voltage imaging.

We imaged intact, awake larval zebrafish mounted using 3% low-melting agarose on a 3-D printed holder in a customized water chamber (**Fig. 1d**), with the fish's head exposed and the tail free. We recorded the tail movement at 500 Hz using a behavior camera. When analyzing the light-sheet images, we observed significant motion artifacts due to tail movement and muscle contractions, which corrupted the neural voltage activity. This motion was multidirectional and non-rigid, complicating correction efforts. To mitigate these artifacts, we paralyzed the fish using a muscle relaxant before imaging, as per methods from prior studies<sup>1,7</sup>, effectively reducing motion to sub-pixel levels. Future endeavors could try to compensate

454 for these motion artifacts through software, better immobilization procedures, or by monitoring fictive  
455 behavior.

456 We chose to image 30 z-planes across a volume of  $930 \times 370 \times 170 \mu\text{m}^3$ , once every 4.98 ms. This translated  
457 to a volume rate of 200.8 Hz and a frame rate of 6024 FPS. Given the 4.98-ms interval between two  
458 successive samplings of the same z-plane, ideally, we would use a voltage indicator that has slow kinetics  
459 (activation time + deactivation time  $\approx 5$  ms) to avoid the possibility of missing a narrow spike that falls  
460 within the 4.98-ms interval. As noted above, there is no perfect indicator, and for the purposes of this study,  
461 we chose to value SNR over kinetics. Positron2-Kv, being essentially Voltron with the mutations used in  
462 pAce<sup>60</sup>, would be anticipated to have the same kinetics as pAce, meaning activation and deactivation time  
463 constants of 0.51 and 0.61 ms at room temperature<sup>52</sup>. We note that this means there is a possibility of  
464 missing spikes, at our volumetric scan speed of 200 Hz; in the current paper, we confine our observations  
465 to those that would be robust to such a loss. Spike loss could have potentially been reduced by using  
466 ASAP3-Kv, which has slower kinetics - 3.7-ms activation and 16-ms deactivation time constants. But, as  
467 noted above, ASAP3-Kv has lower SNR compared with Positron2-Kv, which could in principle result in  
468 spike loss of a different kind. Thus, for the purposes of this microscope validation, we chose to go with  
469 Positron2-Kv.

470 Given the possibility of missing spikes due to the mismatch between the sub-millisecond kinetics of  
471 Positron2-Kv and the 200-Hz sampling rate of our microscope, we quantified the percentage of missed  
472 spikes by analyzing the neural voltage activity in a single z-plane video recorded at 1000 Hz with a 40- $\mu\text{s}$   
473 exposure time. We downsampled the 1000-Hz video by extracting a 200-Hz discrete frame series from the  
474 video, and quantified how many spikes were missed in the downsampled video compared with the 1000-  
475 Hz video. After excluding neurons showing no spikes and neurons affected by moving stripe artifacts, traces  
476 of a total of 201 neurons in the z-plane were analyzed. Note we did not count the neurons showing no spikes,  
477 which had 'perfect' spike detection in a sense. On average, 30.0% of the spikes (out of all spikes of the 201  
478 neurons) observed in the 1000-Hz traces were missed in the 200-Hz traces (**Fig. S6**). This is not surprising  
479 as the Positron2-Kv indicator we used has sub-millisecond rise and fall times. As we discussed in our  
480 original manuscript, to reduce spike loss, we could potentially use GEVIs with slower kinetics. We  
481 validated this approach through simulation and experiments (**Fig. S7**). In the simulation, we compared the  
482 detected spikes reported by ASAP5-Kv<sup>61</sup>, which has ~2.6-ms depolarization and ~4.3-ms repolarization  
483 time constants at room temperature, between 1-kHz and 200-Hz imaging rates (see **Methods** in the  
484 manuscript). The results show that ASAP5-Kv significantly reduced the chance of missing spikes in the  
485 200-Hz traces: 99.7% of all the spikes observed in the 1-kHz traces (n=201 neurons) were reliably retrieved  
486 from the 200-Hz traces (**Fig. S7c**). Experimentally, we also imaged transiently expressed ASAP5-Kv

487 indicator in larval zebrafish at 1000 Hz with a 40- $\mu$ s exposure time. Because the expression was transient  
488 and sparse, we only captured several neurons with spike activity. But still, the spikes observed in the 1000-  
489 Hz traces were well preserved in the 200 Hz traces, which were obtained by extracting discrete, evenly  
490 spaced points in the 1000-Hz traces (**Fig. S7d,e**). In the future, a voltage indicator that combines the kinetics  
491 of ASAP5-Kv and the brightness of Positron2, used in a stable panneuronal fish line, could potentially be  
492 used to prevent spike loss while maintaining high SNR.

493 As the ventral side of the larval zebrafish brain is primarily occupied by neurites<sup>41,62</sup>, imaging beyond a 170  
494  $\mu$ m axial (z) range yields only 5.4% more neuron somas in the 3D-FOV<sup>41,62</sup>. By sampling a 170- $\mu$ m thick  
495 volume with 30 image planes, we achieved a step size between adjacent z-planes of 5.86  $\mu$ m, smaller than  
496 the average diameter of neuron cell bodies ( $6.62 \pm 0.14 \mu\text{m}$ , mean  $\pm$  standard error of the mean<sup>1</sup>) and slightly  
497 larger (by 17%) than the 5- $\mu$ m axial (z) sampling step size that was used to achieve single-cell resolution  
498 in previous studies<sup>1,7</sup>. Under these conditions, we quantified that, on average, the cameras detected  
499  $2.1 \pm 0.8 \times 10^4$  (mean value  $\pm$  standard deviation, n=15 neurons in 1 fish) photons per neuron per frame. Given  
500 the reported ~10% fluorescence response of Positron2-Kv indicator to action potentials<sup>12</sup>, this photon  
501 number corresponds to a theoretical SNR per action potential of 13.8.

502 Due to the obstruction of the fish's eyes, the light sheet cannot illuminate the ventral telencephalon (TL)  
503 region (**Fig. 2a**, yellow dashed lines and arrows, **Fig. 2e**, yellow dashed lines). We also saw blurred regions  
504 (**Fig. 2a**, magenta arrows) in the light-sheet images where single neurons cannot be visually resolved. This  
505 blurring could have resulted from refraction of the light sheet at the sample, or tissue scattering. We visually  
506 examined the raw light-sheet images of a larval zebrafish brain, and on all individual z-plane images, drew  
507 contours of the whole brain (**Fig. S8**, left, orange), the regions that were shadowed by fish's eyes (**Fig. S8**,  
508 middle, cyan), and the blurred regions (**Fig. S8**, right, magenta). We found that single neurons were visually  
509 distinguishable within individual z-planes in 84.7% of areas of the imaged brain (**Fig. S8**). The remaining  
510 areas were either shadowed by the fish's eyes (8.55% **Fig. S8**, cyan contours) or too blurred to resolve  
511 single cells (6.74%, **Fig. S8**, magenta contours). The blurred regions were more concentrated at the lateral  
512 right side of the zebrafish brain, as the light sheet entered the brain from the left side (**Fig. S8**, green arrows).  
513 (We note that this is a problem for calcium imaging as well<sup>63</sup>.) The locations and the proportions of these  
514 regions may vary from fish to fish, possibly due to different developmental stages. The difference in image  
515 quality between the left and right sides of the fish brain also affected the distribution of neurons recorded  
516 on each side of the brain, with more neurons found on the side of light-sheet incidence (**Fig. S9**). In Fish  
517 A–D, 59%, 59%, 62%, and 58% of their putative neurons, respectively, were located on the left side of the  
518 brain—the side from which the light sheet was delivered. In principle, this asymmetric neuron distribution  
519 could be ameliorated by implementing dual light-sheet illumination from both sides of the brain.

520 Many factors, in addition to shot noise, can influence the stability of the fluorescence baseline of neurons  
521 when monitoring voltage activity. Some of these factors can include the readout noise (~7e- in our case) of  
522 camera pixels, limitations in the repeatability of galvo and piezo scanning, small vibrations of the setup and  
523 the sample, and fluctuations in the excitation laser power. To evaluate the extent to which these factors  
524 impact the fluorescence baseline stability in our experiments, we quantified the baseline noise of neurons  
525 that visually did not overlap with any moving stripe artifact (see “Characterization of and dealing with the  
526 “stripe” artifacts in light-sheet images” section below) by imaging the brain of a larval zebrafish pan-  
527 neuronally labeled with a cytosolic fluorescent marker Kaede (Tg(HuC:Gal4; UAS:Kaede)) at 200 Hz (**Fig.**  
528 **S12**). We chose to use Kaede because we happened to have that fish line, and because the excitation and  
529 emission spectra of Kaede matched our current microscope. Kaede fish imaging was performed using the  
530 same protocols as during imaging whole brains of Positron2-Kv fish, except that we adjusted the excitation  
531 power to match the raw image intensity to that in our voltage imaging experiments. We extracted the  
532 average intensity traces of 72 (an arbitrary number) neuron ROIs distributed across a randomly selected  
533 brain plane (out of 30). To obtain these ROIs, an experimenter randomly searched around the areas in the  
534 brain plane that did not visually overlap with any moving stripe in the raw video and manually annotated  
535 them. After correcting for photobleaching by applying a high-pass filter to the raw traces (cut-off frequency:  
536 15 Hz), we calculated the standard deviations of the traces to quantify the measured noise. Moreover, as a  
537 reference, we calculated the theoretical shot noise for each trace. To do that, we first calculated the mean  
538 intensity of each trace and converted the value to photon number by dividing it by the camera’s conversion  
539 factor (0.13 in our case). The theoretical shot noise of each trace was calculated as the square root of the  
540 photon number. The measured noise of these neurons (quantified by the standard deviation of the traces)  
541 was on average  $1.58 \pm 0.45$  (mean  $\pm$  standard deviation, n=72 neurons) times their theoretical shot noise (**Fig.**  
542 **S12b**). The measured noise was on average  $0.83 \pm 0.28\%$  (mean  $\pm$  standard deviation, n=72 neurons) of the  
543 baseline intensity (**Fig. S12b,c**).

544 To obtain ROIs corresponding to putative neurons for extraction and analysis of neural activity and to  
545 quantify the number of individual neurons our methods could monitor in the zebrafish brain, we trained a  
546 deep learning model to automatically segment ROIs corresponding to putative neurons using the deep  
547 network models in Cellpose 3.0<sup>64</sup>. We first used the pre-trained Cellpose 3.0 model<sup>64</sup>, but realized the model  
548 performed poorly on our dataset, likely due to challenges with out-of-distribution generalization to our  
549 dataset. We therefore manually segmented a few thousand neurons and trained our own Cellpose model in  
550 the grayscale mode. In our manual segmentation process, we identified and outlined objects that were  
551 approximately the size of a neuron (~6.6  $\mu\text{m}$ ) and had ring-like boundaries due to membrane labeling.  
552 During the training, we also adopted their iterative bootstrapping idea<sup>64</sup>, where we trained the model with  
553 labelled data, and iteratively fed manually-corrected predictions back into the model (see **Methods**).

554 We evaluated the performance of the segmentation model on a randomly selected fish dataset that had not  
555 been previously labeled (**Fig. S18**). For each test layer, the segmentation model was applied to identify and  
556 annotate the ROIs. Next, an experienced experimenter visually inspected each layer to add ROIs that the  
557 model missed and removed incorrectly labeled ROIs. We used a flow threshold of 0, which disabled the  
558 mask rejection. This will result in an increased number of cells segmented but also increase the number of  
559 false positives. The visual inspection used the same criteria to identify ROIs as during our manual  
560 segmentation process, i.e., annotating objects that were approximately the size of a neuron (~6.6  $\mu\text{m}$ ) and  
561 that had ring-like boundaries. On average, per layer, the experimenter added  $80.2 \pm 27.5$  (mean  $\pm$  standard  
562 deviation, n=30 layers) ROIs and removed  $10.9 \pm 9.4$  (mean  $\pm$  standard deviation, n=30 layers) ROIs from  
563 the model's output. In addition to this evaluation dataset, all fully analyzed datasets in the paper underwent  
564 this same automatic annotation and manual correction process to identify their ROIs.

565 Using the ROIs labeled by the model and refined with manual correction (**Fig. S18**), we processed whole-  
566 brain imaging datasets with VolPy<sup>65</sup>, an automatic analysis pipeline for voltage imaging datasets. Neural  
567 activity traces were extracted by VolPy from the ROIs. **Fig. 2** shows raw images (**Fig. 2a, b**) and example  
568 spontaneous activity traces (**Fig. 2c, d**) from a 5.5-dpf larval zebrafish. **Fig. 2c,d** display the activity traces  
569 of 120 exemplar putative neurons in six brain regions (**Fig. 2e**). These regions include the olfactory  
570 epithelium (OE, red), telencephalon (TL, cyan), habenula (HB, purple), optic tectum (OT, green),  
571 cerebellum (CB, blue), and medulla oblongata (MO, orange) (**Fig. 2c-e**), from different lateral locations  
572 and axial depths, demonstrating our microscope's capability to monitor voltage dynamics from locations  
573 across the whole brain.

574 We observed different temporal patterns from these activity traces. Specifically, we saw single spiking  
575 events (**Fig. 2d**, black arrow on the red traces), burst spiking (**Fig. 2c**, orange arrows on the green and blue  
576 traces, **Fig. 2d**, the bottom two traces), and oscillatory activity (**Fig. 2d**, black arrow on the orange traces).  
577 These traces exhibited high  $SNR_{AP}$ , ranging from 5 – 10.

578 In our experiments, the total excitation power for the fish brain was approximately 10mW at 515 nm  
579 wavelength. This power is much higher (~33.3  $\times$ ) than the power (0.3mW) used in previous whole-brain  
580 calcium imaging experiments<sup>1</sup>. This higher power is required for our voltage imaging experiments to ensure  
581 sufficient photons are collected in each frame, as our imaging rate is 250 times higher than that in whole-  
582 brain calcium imaging experiments<sup>1</sup>. We used an opaque optical mask to block illumination to the fish's  
583 eyes, which have high absorbance of light due to the pigment cells of the retina. To examine whether this  
584 power induced any abnormality to the fish's tissues and cells, we performed immunostaining against four  
585 markers of cellular and synaptic health and compared their levels in fish with and without light-sheet  
586 exposure. These markers were the apoptotic marker cleaved caspase-3, the DNA damage marker H2AX,

587 the neuronal nucleus marker NeuN, and the synaptic marker Synaptophysin, as we and others have used in  
588 prior neurotechnology safety assays<sup>66,67</sup>. The exposed fish were illuminated by a light sheet scanning across  
589 the fish brain at 200.8 Hz, with a total power of 10.4 mW, for a continuous duration of 70 s. This exposure  
590 duration corresponded to the total exposure time of two 35-second imaging trials in our visual stimulation  
591 experiments. For H2AX, we fixed the fish ~1 hour after exposure, as H2AX signals reflecting DNA damage  
592 can be detected just minutes after damage occurs<sup>68</sup>. For the other three markers, we kept fish overnight  
593 before fixing them for immunostaining, as apoptosis, neuron number change and synaptic change are not  
594 instantaneous. Our results showed no significant difference in the levels of these markers between the  
595 exposed fish and the non-exposed fish (**Fig. S19**).

596

#### 597 **Characterization of and dealing with the “stripe” artifacts in light-sheet images**

598 In the raw light-sheet imaging videos, we observed bright and dark “stripe” patterns that were parallel to  
599 the illumination axis (y) of the light sheet (**Fig. 2a,b**, red arrows). Such “stripe” artifacts are a common  
600 issue when using light-sheet microscopes to image non-fully transparent samples<sup>69,70</sup>. Here non-fully  
601 transparent means that some structures, objects, or regions of the sample can absorb, refract, or scatter the  
602 excitation light sheet, altering its propagation. These structures, objects, or regions therefore will “cast”  
603 stripe-shaped artifacts extending from themselves to the edge of the sample, along the light-sheet  
604 illumination direction. While translucent, the larval zebrafish brain is non-fully transparent. The fish’s skin  
605 has different refractive index than water, and a non-flat surface, so it will refract the light sheet in a non-  
606 uniform way; zebrafish brain tissue is non-uniform and has heterogenous refractive indices, which can  
607 refract and scatter the light sheet; blood cells have round shapes and different intracellular refractive index  
608 than their surrounding environment, which could make them act as micro-lenses<sup>71</sup> to converge or diverge  
609 light passing through them. While we used a pigment mutant fish (mitfa<sup>-/-</sup>, also known as nacre), the fish  
610 still developed some opaque tissues at 5 dpf, for example, on the skin above the hindbrain, which could  
611 potentially affect the light-sheet illumination when imaging the top layers of the hindbrain.

612 In our experiments, these stripe artifacts can be seen all over the brain (**Fig. 2a, b**, red arrows). These stripe  
613 artifacts affect the observed images by increasing or decreasing the fluorescent intensity in stripe-shaped  
614 regions. Within the majority part (this number varies from ~50% to near 100% in different fish, probably  
615 due to their difference in blood flow and blood cells’ optical properties) of the imaged brain volume, these  
616 stripe artifacts remained stationary (referred to as “stationary stripes”), meaning that the observed traces  
617 can still reliably reflect actual neural traces over time, despite potential alternations in signal amplitude and  
618 SNR. For the rest of the regions of the brain (varying between near 0% to ~50%, scattered across the whole

619 brain), such stripe patterns exhibited dynamic behavior, “moving” and “flickering” over time (referred to  
620 as “moving stripes”) (Supplementary Video 1; Fig. S10). These moving stripes contaminated neural traces  
621 by rapidly modulating their baselines. The contaminated neural activity traces exhibited pulse-like and fast-  
622 fluctuating temporal artifacts (Fig. S10c; Fig. S11, orange arrows). The prevalence and location of the brain  
623 regions where the extracted neural traces were contaminated by the temporal artifacts varied between  
624 individual fish, possibly due to developmental differences in their circulatory systems.

625 To get a better understanding of the sources of the “stripe” artifacts (unless otherwise specified, the term  
626 “stripe artifacts” refers to both stationary and moving stripe artifacts), we conducted a series of control  
627 experiments (Figs. S13-S15). We asked the question: are the “stripe” artifacts caused by the optical setup  
628 alone, or by an issue related to the animal? To answer this, we first imaged a 3D agarose sample containing  
629 evenly distributed JF525 fluorescent dye following the same protocols that we used to perform 200-Hz  
630 voltage imaging of neurons distributed across entire brains in larval zebrafish. The raw images of the  
631 fluorescent agarose are shown in Fig. S13a. In these agarose images, we saw a gradual variation ( $\sim\pm20\%$   
632 along an 800- $\mu\text{m}$  x-axis range) of intensity along the x-axis, which is perpendicular to the illumination axis  
633 (Fig. S13c). This gradual intensity variation was caused by the non-uniformity of the Powell lens-generated  
634 light sheet, due to imperfections on the lens surfaces. The intensity variation pattern was consistent across  
635 different depths (Fig. S13a), did not change over time, and exhibited low spatial frequency along the x-axis  
636 ( $<0.05 \mu\text{m}^{-1}$ , meaning the intensity changes in space were gradual and smooth) (Fig. S13d). In contrast, the  
637 stripe artifacts observed in zebrafish brain images differed between different brain layers (Fig. S14b) and  
638 featured sharp bright and dark bands (highlighted by red arrows in Fig. S13e). These stripe artifacts were  
639 characterized by high spatial frequencies ranging from  $0.05 \mu\text{m}^{-1}$  to  $0.2 \mu\text{m}^{-1}$  along the x-axis (Fig. S13f,  
640 red arrows). We did not observe such stripe artifacts in the agarose images. In addition, we also added 200-  
641 nm diameter fluorescent beads in the agarose. Sharp, in-focus images of these beads were clearly visible  
642 (Fig. S13a, orange arrows), indicating the absence of stripe artifacts was not due to defocusing. This result  
643 showed that the stripe artifacts were not generated by the imaging setup itself.

644 The  $\sim\pm20\%$  gradual intensity variation along the x-axis, mentioned in the previous paragraph, is unlikely  
645 to pose challenges for imaging and extracting the voltage activity of neurons in the fish’s brain. This is  
646 because: 1) the intensity variation was smooth and gradual across space, meaning that it does not corrupt  
647 the boundaries of individual neurons, and 2) the intensity variation stays stationary over time, ensuring that  
648 no temporal artifacts are introduced to the neural activity traces. If needed, this gradual intensity variation  
649 could be in principle corrected in the raw sample images by using reference images of a uniform fluorescent  
650 sample, such as a 3D fluorescent agarose sample.

651 We performed another control experiment to test if the stationary stripes were sample vs. hardware  
652 dependent (**Fig. S13b**). In this experiment, we shifted the fish along the x-axis (roughly aligned with the  
653 rostral-caudal axis, perpendicular to the illumination axis) in the lateral plane while imaging the zebrafish  
654 brain at 200.8 Hz. The raw images of the same brain plane at two different locations along the x-axis are  
655 shown in **Fig. S13b**. The stripe patterns between the two brain images were highly consistent and remained  
656 at the same locations relative to the fish's brain (**Fig. S13b**, magenta arrows), and not relative to the  
657 microscope's field-of-view. This result suggested that the stationary stripes were dependent on the samples,  
658 not the imaging setup.

659 Some stripe artifacts “flickered” and “moved” during imaging, causing temporal artifacts on the extracted  
660 neural traces. These moving stripes were hypothesized by us to be caused by blood flow in the fish brain<sup>69,70</sup>,  
661 i.e., circulating blood cells passing through the light sheet and altering the propagation of the excitation  
662 light that passed through these cells. To test this hypothesis, we conducted three control experiments. In the  
663 first experiment, we imaged the brain of a paraformaldehyde (PFA)-fixed 5-dpf transgenic Positron2-Kv  
664 larval zebrafish at 200 Hz. We did not observe any moving stripe artifact in the recording (**Fig. S14a**). To  
665 better visualize and map moving stripes' distributions in the fish brain, we computed the normalized  
666 temporal standard deviation map (NTSDM, see **Methods**) of a given time-series recording. In brief,  
667 NTSDM can highlight moving stripe artifacts as bright “stripes” along the illumination direction. In the  
668 second experiment, we stopped the zebrafish heart (thus stopping blood flow) temporarily during imaging  
669 using 2,3-butanedione monoxime (BDM), as used in a previous study<sup>69</sup>. The moving stripes observed prior  
670 to BDM treatment disappeared once the fish's heart was stopped (**Fig. S14b, Supplementary Video 2**).  
671 The stopped heart started again after incubating the BDM-treated fish in fresh water for ~20 mins.  
672 Following the recovery of the fish's heartbeat, moving stripes reappeared in the video. (**Fig. S14b,**  
673 **Supplementary Video 2**) This experiment clearly demonstrated that the moving stripes were dependent on  
674 the zebrafish's heart pulsing, and thus blood flow. In the third experiment, we examined the spatial  
675 correlation of moving stripes and the animal's blood vessels (**Fig. S15**). To do so, we crossed our transgenic  
676 GEVI fish with Tg(flk:DsRed) fish, which have red vascular labeling, and imaged both the green GEVI  
677 signals and red blood vessels in the same imaging session by alternating emission filters. We correlated the  
678 spatial locations of moving stripes with blood vessels in the fish's brain (**Fig. S15**). We found that every  
679 moving stripe (**Fig. S15**, cyan stripes) originated near a corresponding blood vessel (**Fig. S15**, magenta  
680 arrows). This finding strongly supports the conclusion that the moving stripes were caused by blood flow  
681 that altered the light-sheet propagation in a dynamical way.

682 We aim to address the stripe artifact issue as early as possible in the process. In this paper, we demonstrated  
683 an optical approach to remove both the stationary and moving stripe artifacts (**Fig. S16, Fig S17b**). This

approach shares a concept used in earlier works, of using multidirectional illumination<sup>72–75</sup>. In this experiment, we used a resonant mirror scanner to rapidly pivot the light-sheet in the image plane during each camera exposure. By doing this, the stripe artifacts were dispersed and averaged out over broader areas. In more detail: to efficiently remove stripe artifacts, the light sheet must be pivoted across a sufficiently large angle during a single frame exposure, so that stripe artifacts can be averaged out across sufficiently large areas. One specific challenge we encountered was that our microscope acquires images at a rate of several thousand frames per second—tens of times faster than those reported in previous studies<sup>72–75</sup>. This high frame rate (and thus short exposure time) requires high pivoting speed, as well as precise timing control of the light-sheet pivoting to prevent frequency aliasing artifacts. To provide sufficient pivoting speed, we employed an 8-kHz resonant mirror scanner (RESSCAN, Sutter Instruments), which has a scan period of 127 μs, to pivot the light sheet. We set the camera exposure time to be the same as the resonant scanner's scan period (127 μs), ensuring that the light sheet completed a full pivoting cycle during each frame exposure, regardless of when the exposure started. Additionally, to prevent temporal artifacts caused by frequency aliasing between the volumetric light-sheet z-scanning and light-sheet pivoting, we synchronized the start of each volumetric z-scan with the start of a pivoting scan.

In our voltage imaging experiments, we deliberately shortened the frame exposure time to minimize motion blur caused by axial (z-axis) movement of the imaging plane during exposure. In our 30-plane, 200-Hz zebrafish brain imaging experiments, we set an exposure time of 40 μs while operating the camera at 6025 frames per second, resulting in an approximately 24% duty cycle for active exposure time. During a 40-μs exposure, the image plane shifted in z-axis by ~2.7 μm. However, as discussed in the previous paragraph, for our stripe removal experiments utilizing a resonant scanner, we had to match the exposure time to the resonant scan period (127 μs) to ensure completion of a full pivoting scan per frame exposure. Therefore, to reduce the motion blur in the stripe removal experiment, we reduced the axial scan range to 120 μm in the zebrafish brain and imaged 20 planes at 203 Hz. This corresponded to a frame rate of 4060 Hz and a 52% duty cycle for the active exposure time, and the focal plane shifted in z-axis by ~6.1 μm during each 127-μs exposure. We would like to note that, in principle, the number of imaged planes can scale linearly with an increase in the resonant frequency. For example, employing a 12-kHz resonant mirror scanner would enable this stripe removal approach to support imaging of  $20 \times 12 \text{ kHz} / 8 \text{ kHz} = 30$  planes of the zebrafish brain at 200 Hz. The shifting distance of the focal plane in the z-axis could also be potentially reduced using a faster resonant scanner that has a shorter scan period. For example, a 12-kHz resonant scanner has a scan period of 83.3 μs. This would reduce the exposure time and the focal plane shifting distance per exposure by  $1 - \frac{83.3}{127} = 34\%$ .

716 In the stripe removal experiments, we imaged 20 planes of a zebrafish brain at 203 Hz for a duration of 50s.  
717 During the first 30s, the resonant scanner was on. Then the resonant scanner was turned off for the  
718 remaining 20s. **Fig. S16** compares the images and the neural traces of the same image planes between the  
719 periods when the resonant scanner was on and off. When resonant scanner was running, both the static and  
720 the moving stripe artifacts were eliminated in the zebrafish brain (**Fig. S16a,b,d,e, h,i,k,l**). Moreover,  
721 neuron activity spikes that were previously obscured by the temporal artifacts from the moving stripes  
722 became detectable (**Fig. S16c,f,j,m**, red arrows).

723 The temporal standard deviation (TSD) can be used to approximate the noise of neural traces contaminated  
724 by the moving stripe artifacts, which is the dominant cause of temporal deviation in these traces (see  
725 **Methods**). To evaluate the performance of our stripe removal approach, we measured the temporal standard  
726 deviations (TSDs) of the traces of moving-stripe affected neurons (meaning these neurons were affected by  
727 moving stripes when the resonant scanner was off)—as a way to quantify the strength of the moving stripe  
728 artifacts—and compared the TSDs with and without light-sheet pivoting. When the resonant scanner was  
729 activated, the TSDs of the traces of moving-stripe affected neurons decreased by an average of 42%, and  
730 the traces of more than 90% of these neurons showed reduced TSDs (**Fig. S16g,n**). Additionally, we noticed  
731 that a small subset of neurons (<1% of all imaged neurons, **Fig. S16c,f,j,m**, trace 11) that did not exhibit  
732 moving-stripe-induced artifacts in their traces when the resonant scanner was off, showed temporal artifacts  
733 in their traces when the resonant scanner was active. Why did this light-sheet pivoting approach fail to  
734 remove all moving stripe-caused temporal artifacts, or even exacerbate such artifacts in the traces of certain  
735 neurons? Conceptually, this light-sheet pivoting approach removes a stripe artifact by dispersing and  
736 averaging out the stripe over a broader, fan-shaped region behind the stripe source. Therefore, a larger  
737 pivoting angle generally leads to better artifact removal. However, our illumination objective's numerical  
738 aperture (NA=0.28) limited our maximum pivoting angle to 32.5 degrees. This angle might not be  
739 sufficiently large to eliminate the moving-stripe-induced temporal artifacts in the traces of all affected  
740 neurons, particularly those right behind a moving stripe source. Furthermore, by dispersing the moving  
741 stripe artifact into previously unaffected regions, light-sheet pivoting might inadvertently introduce  
742 temporal artifacts to the traces of a minority of neurons that were originally artifact-free. In principle, these  
743 limitations could be addressed in the future by employing an illumination objective lens with a larger NA.  
744 While we demonstrated the effectiveness of the stripe removal method using a resonant scanner, due to the  
745 limited resonant frequency (8 kHz), our resonant scanner only allows us to record 20 planes across a 120-  
746  $\mu\text{m}$  thick volume in the zebrafish brain at 200 Hz. Therefore, when we imaged the voltage activity across  
747 entire fish brains (30 planes across a 170- $\mu\text{m}$  thick volume), we did not use this stripe removal method. As  
748 a result, similar to previous LSM studies<sup>69,70</sup>, the extracted neural activity traces from our whole-brain

749 datasets were susceptible to varying intensity artifacts caused by the movement of small objects (e.g. blood  
750 cells in the vasculature or dust particles in the water) obstructing, refracting, or scattering the excitation  
751 light. In our setup, the excitation light sheet enters the larval zebrafish brain from one lateral side (**Fig. 1d**;  
752 **Supplementary Video 1**, green arrow). When the light sheet encounters a moving object in the sample, the  
753 object disrupts the light sheet's propagation and casts a stripe-shaped artifact extending from the object's  
754 location to the other lateral edge of the brain along the illumination direction of the light sheet (**Fig. S10b**,  
755 along the cyan ROIs and along the red ROIs; **Fig. S11**, green arrows; **Supplementary Video 1**, white  
756 arrows). As the object moves, this stripe artifact varied dynamically, introducing pulse-like and rapidly  
757 fluctuating artifacts into the temporal traces of the segmented ROIs (**Fig. S10c**; **Fig. S11**, orange arrows).  
758 Pulse-like artifacts could, in principle, be mistakenly identified as spikes by the automatic spike detection  
759 process. Therefore, any ROIs containing even a single pulse-like artifact should be excluded from further  
760 analysis (future analyses could, in theory, enable pulse-like artifacts to be subtracted away, sparing these  
761 ROIs for downstream analysis). To identify them, we looked for ROIs with highly correlated pulse-like  
762 activities distributed along the fish's medio-lateral axis (**Fig. S10b,c**). To facilitate the identification of  
763 contaminated ROIs, we clustered ROIs with similar temporal traces. We first applied a 250-ms moving  
764 Hanning window to each ROI's spike raster for smoothing and estimating its firing rate. Subsequently, we  
765 used the Uniform Manifold Approximation and Projection<sup>76</sup> (UMAP) algorithm to map the smoothed raster  
766 of each ROI onto a 2-dimensional manifold (**Fig. S24a**). Following this mapping, we utilized the Density-  
767 Based Spatial Clustering of Applications with Noise<sup>77</sup> (DBSCAN) algorithm to separate the ROIs into  
768 clusters.

769 Each cluster on the 2-dimensional UMAP manifold contained ROIs with similar spiking activities (**Fig.**  
770 **S11**; **Fig. S24a**). Next, we visually inspected each cluster's ROIs' temporal traces and their spatial  
771 distributions within the fish (**Fig. S11**). Our criteria to identify an artifact cluster were: 1) the temporal  
772 traces of the cluster's ROIs exhibited synchronous pulse-like patterns (**Fig. S11**, orange arrows); 2) the  
773 spatial distribution of the cluster's ROIs had the same spatial features of the artifact stripes or shadows, i.e.,  
774 the ROIs were concentrated in a region (or regions) that was narrow in the x and z axes (< 100 µm) and  
775 spanned from a certain location (possibly in the middle of the brain, as there are blood vessels) to the edge  
776 of the brain opposite to the edge of light sheet incidence, along the y axis (light sheet illumination axis)  
777 (**Fig. S11**, green arrows). A cluster was identified as an artifact cluster only when it satisfied both these  
778 criteria. To better illustrate these criteria, three artifact-contaminated clusters and three non-artifact clusters,  
779 both randomly selected from Fish B, are presented in **Fig. S11**. Once we determined a cluster was  
780 contaminated by artifact, we removed all the corresponding ROIs, and used the remaining ROIs to repeat  
781 the UMAP-DBSCAN process until all the clusters with artifact contamination were removed (see **Methods**).

782 In the future, specific algorithms might be developed to identify and decompose these highly correlated  
783 pulse-like artifacts as independent components, easily separated from the neural activity, so that artifact-  
784 contaminated ROIs can also be used.

785

## 786 Imaging of voltage activity of neurons distributed through entire brains

787 Zebrafish larvae, like other fish species, possess UV-sensitive photoreceptors<sup>78</sup>. Due to the differential  
788 propagation of light of various colors in water, multicolor visual processing in zebrafish may help detect  
789 stimuli such as those related to prey and predators<sup>78</sup>. Additionally, zebrafish larvae exhibit intensity-  
790 dependent negative phototaxis away from UV light, perhaps to avoid damage<sup>79</sup>. Whole-brain calcium  
791 imaging studies<sup>15,17</sup> (including one by a first author of this work) have revealed that the onset of high-  
792 intensity 405-nm light illumination (~0.6 mW/mm<sup>2</sup>) – a higher level of illumination than in the  
793 aforementioned behavioral studies, chosen for its salience - can induce brain-wide activity in larval  
794 zebrafish, within one second. Here we adapted this light stimulation paradigm to deliver light stimulus to  
795 5-6 dpf larval zebrafish and imaged their neural voltage activity. The fish were imaged at a volume rate of  
796 200.8 Hz for 35 seconds. During the 35-s imaging trial, we turned on the light stimulus for the 10-s period  
797 from t =13 s to t=23 s (Fig. 3a). We performed two identical trials for each fish, with a 20-min dark interval  
798 in between.

799 This visual stimulation experiment was conducted on a total of 8 fish over 3 separate days. Of these, one  
800 fish exhibited a slow heart rate. We therefore didn't continue trial 2 in that fish. Additionally, 3 fish were  
801 excluded from the analysis due to large fish position drift between trials (>5 pixels on the x- or y-axes),  
802 possibly because the fish moved slightly. For the rest of the fish (n=4), minor drift on the x- and y-axes was  
803 observed during the experiments (<1 pixel or <0.73 μm on both x- and y-axes within a trial, and <2 pixels,  
804 or <1.46 μm on both x- and y- axes between two trials) (Fig. S20). This drift was corrected using a motion  
805 correction method (NoRMCorre<sup>80</sup>), ensuring that the neurons remained aligned across trials, and that the  
806 same neurons could be reliably compared between the two trials. The four fish presented in the paper are  
807 referred to as Fish A, B, C, and D. We delivered the UV stimulus from the lateral right side in Fish A, B  
808 and lateral left side in Fish C, D (Fig. 3a). By having UV stimulation from either side, we could better  
809 assess the impact of one-sided light-sheet illumination.

810 Although we set each trial's time to be 35s, we were able to continuously image the whole fish brain for a  
811 much longer period, which, in principle, is limited by photobleaching and storage. We demonstrated this  
812 capability by performing a 200-s recording of the whole zebrafish brain at a 200.8 Hz volume rate (Fig.  
813 S22). We showed traces from two arbitrarily selected neuron ROIs (Cell A, Cell B) from this dataset, and

814 found that voltage spikes (extracted through VolPy) could still be detected at the end of the recording, with  
815 somewhat lower amplitudes due to photobleaching (32% lower in Cell A, 6% lower in Cell B). We further  
816 quantified the photobleaching curve of Positron2-Kv (stained with JF525) fluorescence in our experiments  
817 for a 10-min period of time (**Fig. S23**). The fluorescence dropped by 50% after imaging for approximately  
818 210 s. We noticed that in **Fig. S22**, the spike amplitude reductions of Cell A and Cell B were slower than  
819 the photobleaching curve shown in **Fig. S23**, which decreased by 42% over the same time period. Several  
820 factors could explain this: 1) The filtering and denoising steps in Volpy may boost spike amplitudes,  
821 counteracting the effect of photobleaching. 2) The photobleaching measurement in **Fig. S23** represented an  
822 average response, whereas these two cells provided only individual examples.

823 During light-sheet imaging, excitation light can enter the fish's eyes as a visual stimulus. To reduce the  
824 visual stimulus from the light sheet, we placed a customized opaque optical mask ( $\Phi$  900  $\mu\text{m}$ , optical  
825 density >5, see **Methods**) in the illumination light path to block direct light from the fish's eyes. This mask  
826 reduced the direct excitation light by a factor of at least  $10^5$  in a 225- $\mu\text{m}$  diameter circular area ( $\Phi$  900  $\mu\text{m}$   
827 reduced by 4 times through a tube lens and the 4 $\times$  illumination objective lens) at the fish's eyes (~250  $\mu\text{m}$   
828 in diameter). Excitation light might also enter the fish's eyes through scattering, but we did not quantify the  
829 amount of this scattered light due to the difficulty of quantifying light scattering in the fish's brain. Adding  
830 the optical mask did not increase the brain volume shadowed by the fish's eyes.

831 The datasets of four fish (Fish A, B, C, and D) were fully analyzed in the visual stimulation experiment.  
832 Regions-of-interest (ROIs) corresponding to putative neurons were segmented using a custom-trained deep  
833 learning model based on Cellpose, followed by manual corrections (see **Methods**). This resulted in  
834 identification of 17700, 25552, 25464, and 17419 ROIs in Fish A through Fish D, respectively. The  
835 segmented ROIs were subsequently processed through VolPy's temporal trace extraction pipeline, which  
836 includes background removal, trace denoising, and spike extraction. For spike detection, an adaptive  
837 thresholding approach was employed within VolPy.

838 Given the existence of moving stripe artifacts in our whole-brain datasets, the extracted neural activity  
839 traces from these segmented ROIs were affected by temporal intensity artifacts caused by the moving stripe  
840 artifacts. These temporal artifacts exhibited pulse-like or rapidly fluctuating patterns that could, in principle,  
841 be mistakenly identified as spikes by the automatic spike detection process. Therefore, for each dataset, we  
842 identified artifact-contaminated ROIs by visually inspecting ROIs that were grouped based on similarity of  
843 their temporal traces' patterns (see "**Characterization of and dealing with the "stripe" artifacts in light-**  
844 **sheet images**" section above). We excluded these ROIs from subsequent analysis.

845 The remaining ROIs (n=12935, 15135, 19039, 15998 for Fish A-D, respectively) after removing ROIs  
846 corrupted by moving stripe artifacts were treated as putative neurons. We calculated neuron density of all

847 putative neurons in Fish A (arbitrarily chosen). To assess the spatial distribution of putative neurons (after  
848 artifact-contaminated ROI removal), we measured the average distance between each putative neuron's  
849 centroid and its 10 nearest neighbors' centroids in the same Z-plane, and plotted the results as a histogram  
850 (**Fig. S21**). The putative neurons in Fish A had separation distances ~31% larger than the literature-based  
851 estimate (13.6  $\mu\text{m}$ , see **Methods**), with a mean distance of  $17.8 \pm 15.2 \mu\text{m}$  (mean  $\pm$  SD,  $n = 12935$  putative  
852 neurons). The larger separation distance is possibly due to expression variation in different brain regions  
853 (see **Fig. S29**), removal of moving-stripe-contaminated ROIs, and reduced image quality in certain brain  
854 regions due to tissue scattering (see **Fig. S8**). To examine the effects of one-sided illumination on the  
855 distribution of putative neurons (defined as all segmented ROIs after removing the artifact-contaminated  
856 ones), we analyzed the spatial distributions of all putative neurons along the lateral left-right axis (y-axis)  
857 in the brains of Fish A,B,C, and D. For each fish, we plotted three histograms: one for all putative neurons,  
858 and two for putative neurons that passed two  $\text{SNR}_{\text{VolPy}}$  thresholds ( $\text{SNR}_{\text{VolPy}} > 2$ ,  $\text{SNR}_{\text{VolPy}} > 4$ ). The two  
859 thresholds were chosen somewhat arbitrarily, but hopefully give the reader a sense of what the data quality  
860 is like. Here  $\text{SNR}_{\text{VolPy}}$  is a parameter that VolPy calculates for each extracted neural trace.  $\text{SNR}_{\text{VolPy}}$  is  
861 defined as the ratio between the average detected spike amplitude and the standard deviation of the negative  
862 portions of the trace filtered by a 15-Hz high-pass filter<sup>65</sup>. We found almost all (98.4%,  $n=4$  fish) putative  
863 neurons had  $\text{SNR}_{\text{VolPy}} > 2$  (**Fig. S9a-d**), probably because VolPy's denoising and footprint optimization  
864 algorithms automatically increased the  $\text{SNR}_{\text{VolPy}}$  of the extracted traces<sup>65</sup>.

865 We applied UMAP to project the putative neurons onto a 2D manifold (**Fig. 3b, S24b**) and utilized  
866 DBSCAN to partition the neurons into distinct clusters. This analysis revealed a specific group of neurons  
867 (Group 1, **Figure 3b**, blue) that demonstrated increased spiking activity following the onset of UV (405  
868 nm) light stimulation during each of the two trials. Notably, this response was triggered by the light turning  
869 ON, but not OFF, aligning with previous findings from calcium imaging studies<sup>81</sup>. Another cluster (Group  
870 2, **Figure 3b**, orange) exhibited recurring burst activity throughout the recordings, which appeared  
871 uncorrelated with the stimulus. The remaining neurons, which lacked distinct temporal patterns, were  
872 classified as Group 3 (**Figure 3b**, gray). Neurons in different groups exhibited different spatial distributions  
873 in the brain. Averaged across all 4 fish, Group 1 neurons were located mostly (~92%) in the optic tectum  
874 (**Figure 3c**, blue). Group 2 neurons were mostly (~90%) located in the hindbrain of the fish (**Figure 3c**,  
875 orange). Group 3 neurons were scattered across the brain (**Figure 3c**, gray). Please note – we do not intend  
876 these groups to be considered as fundamental scientific classes of cell type; they are simply meant to  
877 represent the kind of pattern our technology can unveil. Such patterns could lead to hypotheses that could  
878 be tested with further investigations, e.g. causal perturbation, and varying behavioral and other contexts.

Upon examining the raw ROI traces, in addition to photobleaching (**Fig. S25a**, black arrows), we noticed a decay in the overall fluorescence intensity of all ROIs as the 405 nm LED turned on (**Fig. S25**, orange curve and red curves). After the LED was turned off, the decreased fluorescence recovered. We hypothesized that this decay and recovery in fluorescence intensity might result from reversible photoswitching of the Positron2 indicator when being exposed to 405-nm light. Previous studies<sup>82</sup> showed that shining 488-nm blue light could reversibly increase the fluorescence intensity of paQuasAr3, an opsin-based voltage indicator. Positron2 is based on the opsin-FRET design, which means the observed fluorescence from Positron2 is the fluorescence emitted by the fluorophore donor minus the fluorescence absorbed by the opsin acceptor. Therefore, assuming that 405-nm light could reversibly increase the absorbance efficiency of the opsin acceptor of Positron2, there would be a decay of the fluorescence at the onset of the light stimulus and a recovery of the fluorescence after the light stimulus was turned off, as what we observed in our experiments. Further biophysical studies of voltage indicators in such contexts may be helpful in the future, but here we simply note that the phenomenon was reversible and easily isolated from the true signal. Since this LED-induced fluorescence intensity change affected the entire fish, its impact on neuronal temporal traces could be effectively mitigated during the background removal step of VolPy (**Fig. S25**). Despite the LED-induced intensity change, the rise of activity at the onset of LED stimulation was visible in Group 1 neurons' raw traces and the VolPy-extracted traces (**Fig. S25a,b**, orange arrows). In contrast, non-Group 1 neurons did not exhibit this sudden increase of activity following the onset of the light stimulus (**Fig. S25a,b**, green arrows).

We examined the temporal dynamics of Group 1 neurons in response to the onset of UV stimulation. We found that there were more Group 1 neurons (70%, 79%, 57%, and 67% in Fish A-D, respectively) located on the left side of the OT region than on the right (**Fig. 3c**, **Fig. S9e-h**). In all four fish, the excitation light-sheet illuminated from the left of the brain. In Fish A and B, UV stimulation was delivered from the right side, whereas in Fish C and D, UV stimulation was delivered from the left. These observations suggest that the predominance of neurons on the left side is likely due to the incident direction of the excitation light-sheet. The left side exhibited better SNR (**Fig. S9**), as the light sheet traveled through thinner brain tissue and maintained better quality in this region. In principle, this one-sided heavy neuron distribution could be resolved by implementing dual light-sheet illumination from both sides of the brain.

Next, we examined the temporal structure of Group 1 neurons to identify potential patterns in their activity. We smoothed each Group 1 cell's spike raster with a 100-ms Hanning window to estimate its spiking rate. We then determined the peak firing rate of each Group 1 neuron and its timing relative to the UV stimulation onset, which we called the latency. We ordered the cells by their mean latencies, averaged across the two trials, with smaller IDs indicating earlier timing of the respective neuron's peak activity (**Fig. 4a,e**, **Fig.**

912 S26a,e). The same ordering persisted across the two trials (confirmed by correlation analysis of the cells'  
913 mean latencies across two trials, Fig. 4b,f, Fig. S26b,f), revealing a consistent temporal sequence spanning  
914 approximately 200 ms in response to the onset of the UV stimulus (Fig. 4a,e, Fig. S26a,e).

915 Curiously, the temporal sequence of the neurons' activities corresponded to distinct locations within the  
916 brain. We observed the cells' mean latency to peak firing was correlated with neurons' location on the  
917 medial-lateral axis (Fig. 4c,g). Neurons that fired earlier were located at lateral locations of the OT, whereas  
918 those that fired later were situated in more medial locations (Fig. 4d,h). The spatiotemporal firing patterns  
919 elicited by the UV stimulus were largely consistent across all four fish, on both the left and right sides of  
920 the OT. One exception occurred in Fish C on the right lateral side, where neurons in the medial portion of  
921 the OT fired earlier in the sequence. This deviation may be influenced by the lower SNR observed on the  
922 optic tectum's right side, or factors we did not control in this experiment, e.g., the animal's behavior.

923 This result showcases that imaging the voltage of neurons distributed across entire brains can be used to  
924 create novel hypotheses, in this case, a mapping of time onto space. How do these across-brain voltage data  
925 compare to known anatomical and physiological data? In a recent review of discoveries based on classical  
926 techniques, Isa et al.<sup>83</sup> synthesized an anatomical map of the tectum along with visual processing pathways  
927 for various stimuli, including small and large objects and dimming. We note that this study did not explicitly  
928 isolate UV light responses; recent studies on multicolor visual circuits<sup>78,81,84</sup> showcased the activation of  
929 optic-tectum-wide neuronal populations for both visible and UV stimuli using calcium imaging. The  
930 observed similarities between activation maps between UV and visible light suggest that UV-processing  
931 circuits might follow the (better described) organizational principles of visible light ones. One principle is  
932 the optic tectum's multilayered organization<sup>85</sup>, with the first layer being the most lateral, followed by  
933 successive layers, each progressively more medial. Retinal ganglion cell axons have synapses with neurons  
934 in more lateral layers. The neurons of the first tectal layer have neuronal connections with neurons in more  
935 medial optic tectum layers, and in brain regions outside the tectum. In summary, we observed a sequential  
936 activation of neurons, starting from the lateral locations (known to receive direct retinal input), and  
937 progressing to more medial regions (probably through synaptic connections). While the purpose of our  
938 current experiment was not to do a full scientific study, but rather to show the kind of hypotheses that one  
939 could generate with our new technology, such hypotheses could be validated by registering our data to  
940 zebrafish brain atlases<sup>14,86</sup> or through downstream experiments using techniques such as optogenetics,  
941 synaptic tracing, and ablations, were this to be a full scientific study.

942 With the hope of seeing more detailed structures of the optic tectum, we acquired high resolution images  
943 of the optic tectum of Fish C (randomly chosen) using a confocal microscope right after the UV stimulation  
944 experiment. The confocal imaging provided smaller pixel size ( $0.16 \times 0.16 \times 1 \mu\text{m}$ ) compared to our light-

sheet setup ( $0.73 \times 0.73 \times 5.86 \mu\text{m}$ ), allowing for more detailed visualization of the optic tectum. We successfully co-registered the functional light-sheet data with the confocal images and now include overlays of firing neurons' centroids in multiple z-sections of the brain (Fig. S30). Although the functional data from this dataset (Fish C) exhibited slightly more complex neuronal firing patterns compared to Fish A, B, and D, the overall trend—lateral neurons firing before medial ones—remained consistent with our original findings. While the confocal data did not qualitatively improve our understanding of optic tectum structures, it does show that functional imaging can be augmented with high-resolution structural data. This integration showcases the potential for future research to employ advanced techniques such as expansion microscopy, ExFISH<sup>87</sup>, or ExSEQ<sup>88</sup>.

Next, we examined the temporal characteristics of Group 2 neurons, present in all four fish, which exhibited multiple bursts within their activity patterns (Fig. 5). To define a burst event, we first smoothed each neuron's spike raster with a 70-ms moving Hanning window to estimate its spiking rate. The population spiking rate was then determined by averaging the smoothed raster across all Group 2 neurons (Fig. 5a). A burst was detected when the spiking rate increased above a threshold, set at five times that of the average population spiking rate across two trials (Fig. 5a). This threshold was chosen somewhat arbitrarily, to isolate burst events. Upon inspection, we noted that these bursts were not fully synchronized across neurons, but instead occurred at slightly different times, across the population of neurons involved in bursts. Curious to see if the slight differences in timing were consistent, we investigated whether there was a reliable temporal ordering of Group 2 neurons' activities during bursts. We identified each Group 2 neuron's peak firing rate, and timing thereof, within every burst event. We then ordered the Group 2 neurons based on their peak firing rate timing averaged across all the burst events (Fig. 5a,b,f,g, Fig. S27). Smaller IDs indicate that the respective neuron's peak activity occurred earlier in the burst event.

Indeed, neurons that fired earlier in the first burst of a series, fired earlier in later bursts of the series (Fig. 5a,b,f,g, Fig. S27) — there was a consistent ordering of firing of neurons, within these nearly, but not-quite, synchronized bursts. We asked whether the temporal features of Group 2 neurons also corresponded to any spatial characteristics, as in the case of light stimulus-evoked activity, above. We noticed that in Fish B and C, a specific region in the MO contained many neurons that fired early during burst events, and were concentrated within a defined volume ( $\sim 20 \times 110 \times 40 \mu\text{m}^3$ , x by y by z) (Fig. 5c, h, magenta arrows, 5d,e,i,j, magenta color). Through visual inspection, the spatial position of these earliest-firing neurons (Fig. 5d,e,i,j, magenta color) coincided with a specific physical neuronal cluster, potentially in rhombomere 5, close to or potentially the same as the cluster of MiD2 reticulospinal neurons<sup>41</sup>. By recording their activity using calcium imaging in fictively swimming larval zebrafish, Chen et. al.<sup>41</sup> found that the MiD2 neurons are involved in bilateral swimming, with no selectivity for turning actions. However, that study could not

978 determine the order of activation across different neuron populations in these motor pathways, due to the  
979 limited speed of calcium indicators and the slow optical sampling rate used (2 to 3 Hz). Our study lacks  
980 fictive swimming recordings to establish any behavioral correlates of the neuronal activities we observed,  
981 so we cannot make any conclusions regarding the precise identity of the neurons we have pinpointed. But  
982 if this were a full scientific study, optogenetics, anatomical tracing, and other kinds of experiments could  
983 be used to pinpoint the identity and causal role of the neurons observed. For the purposes of the current  
984 study, we simply highlight the ability of our technology to reveal the precisely timed operation of this  
985 cluster of neurons, relevant to other circuitry.

986 Curiously, the putative physical cluster of neurons identified in Fish B and C that fired early in the bursts  
987 was not observed in Fish A and D (**Fig. S27**). This variation across fish is not unexpected. Unlike Group 1  
988 neurons, whose activities are elicited by the controlled UV stimulus, the burst patterns of Group 2 neurons  
989 do not correlate with the UV stimulus. The distinct burst patterns observed in Fish A and D may reflect  
990 different underlying neural computations or behaviors compared with those in Fish B and C. Our  
991 experiment did not monitor possible behaviors. Therefore, we were unable to explore the differences  
992 between these burst patterns. Nevertheless, the observed consistency and variability in these burst patterns  
993 could lead to new hypotheses for future research.

994

## 995 DISCUSSION

996

997 We here present a microscope optimized for the imaging of the voltage of individual neurons distributed  
998 throughout the entire larval zebrafish brain. The microscope utilizes an optimized form of remote  
999 refocusing, in conjunction with an optimized optical train and an optimized camera strategy, so as to enable  
1000 the imaging of the entire volume of the larval zebrafish brain, at 200 volumes per second, with single-cell  
1001 resolution, with sufficient SNR to image action potentials in GEVI-expressing neurons distributed  
1002 throughout the brain. Our technique was able to reveal sequences of neurons that fire in consistent order,  
1003 over timescales of milliseconds, both in response to visual stimuli and in stimulus-independent bursts, and  
1004 to map those sequences onto defined locations distributed throughout regions in the larval zebrafish brain,  
1005 revealing novel time-space mappings. Thus, our microscope can reveal novel patterns that would be too  
1006 fast, yet too distributed, to detect with prior technologies. Combined with other stimuli, and fictive behavior  
1007 paradigms (and, potentially in the future, freely moving behavior paradigms), our technique could be  
1008 immediately applied to confront a variety of systems neuroscience questions (some that immediately come  
1009 to mind include the mechanisms of “up” and “down” states during sleep, and excitatory-inhibitory balance

1010 in the brain<sup>1</sup>). Using red-shifted dyes<sup>89</sup> and blue-shifted opsins, perhaps in conjunction with holographic  
1011 optogenetic control<sup>90</sup>, our technique could in principle, support the integration of voltage imaging and  
1012 optogenetics, enabling simultaneously monitoring and manipulating the voltage activity of neurons  
1013 distributed across entire brains.

1014 While at the conceptual level, our microscope follows the widespread idea of light-sheet microscopy with  
1015 remote refocusing, there were several necessary innovations in the design and implementation of the  
1016 microscope, that brought its capabilities to the level required for voltage imaging of neurons distributed  
1017 across entire brains. First, we have designed a new remote scanning module, and the software and pipeline  
1018 for calibration and control. We combined a large shift, high resonant frequency piezo bender scanner with  
1019 a lightweight mirror for remote scanning, to enable 200- $\mu\text{m}$  axial scanning at up to 300 Hz (or >100  $\mu\text{m}$  at  
1020 500 Hz). We also developed the hardware, software, and pipeline (see “Implementation of the microscope  
1021 design” section) to allow accurately calibrating and controlling the remote mirror movement. This is a  
1022 nontrivial design, because accurately calibrating and controlling the movement of a piezo bender scanner—  
1023 which operates at hundreds of hertz in open-loop mode, and exhibited hysteresis—was challenging. To  
1024 achieve the desired waveform, we had to measure the piezo bender’s movement at a rate of tens of kilohertz,  
1025 and at sub-micrometer precision, and conduct iterative fine adjustments of the driving signals that contained  
1026 multiple unconstrained parameters. Second, remote refocusing enhances the microscope’s optical scanning  
1027 rate, but exacerbates the mismatch between the microscope’s optical scanning speed, and the camera’s  
1028 acquisition speed. To alleviate this mismatch and improve imaging speed, we combined distributed planar  
1029 imaging<sup>42</sup> with remote-refocusing light-sheet microscopy, efficiently doubling the volume rate for voltage  
1030 imaging. This strategy could in principle be further scaled up, by chaining multiple distributed planar  
1031 imaging modules and splitting the image to more cameras, to achieve even higher volume rates. Third, we  
1032 are the first (to the best of our knowledge) to use sensors designed to combine high frame rates with large  
1033 camera pixel numbers, for high-speed microscopy imaging. Indeed, we had to build a custom camera using  
1034 this sensor, for our initial microscope implementation, and to assess its performance. Our custom camera’s  
1035 firmware and software integrate open-source architectures widely used in the neuroscience community  
1036 (Firmware: Open-Ephys ONIX; Software: Bonsai), and could significantly accelerate future high-speed  
1037 camera development, reducing the time required to adapt novel sensor chips into microscope architectures.  
1038 Since our initial work, commercial camera manufacturers have now introduced cameras based on this  
1039 sensor, easing its adoption by other labs.

1040 Our microscope shows that we are crossing the threshold where imaging of voltage of neurons distributed  
1041 across an entire brain is possible, but there is much room for improvement in essentially every aspect of the  
1042 technology. Improved GEVIs, with better brightness, SNR, and kinetics, are always welcome. Higher

1043 spatial and temporal resolutions, and better SNRs, of the optics, would always be desirable. Currently the  
1044 imaging rate of our technique is limited by the camera's pixel rate. However, higher imaging rates, up  
1045 to >1000 hertz, could be achieved in principle with our current setup, to image a 3D-FOV smaller than the  
1046 entire zebrafish brain. In practice, the 200-Hz voltage imaging of neurons distributed across entire brains  
1047 shown here, and kilohertz regional imaging, could be performed in the same experiment at different times  
1048 as part of an overall strategy to tackle a biological problem across scales and resolutions. As faster, more  
1049 sensitive image sensors are developed, we expect the speed bottleneck to be alleviated, and whole-brain  
1050 voltage imaging with temporal resolutions down to sub-milliseconds will almost certainly become possible.  
1051 An additional light sheet illuminating from the front of the fish could be added to excite the brain volume  
1052 between the fish's eyes, which is currently shadowed by the physical eye mask from the laterally  
1053 illuminated light sheet. To reduce light scattering in the tissue, GEVIs with long excitation wavelength, or  
1054 multi-photon light-sheet excitation could be exploited. Post hoc analysis of zebrafish brains via expansion  
1055 microscopy<sup>91</sup>, perhaps with barcoded neurons for easy tracing<sup>92,93</sup>, and with *in situ* sequencing of gene  
1056 expression patterns<sup>88</sup>, could help link brain structure and molecular composition to emergent dynamics.

1057 The large datasets produced through large scale voltage imaging necessitate specialized algorithms and  
1058 software for efficient processing and analysis. While existing software packages and denoising algorithms,  
1059 such as VolPy, can be modified for these purposes, there is room for new algorithms to help more efficiently  
1060 segment neuron ROIs from densely labeled brain images, as well as for extracting and demixing voltage  
1061 signals from densely packed neurons. Of course, interpreting whole-brain neural codes through machine  
1062 learning and simulation, also presents unique opportunities for understanding how entire brains work  
1063 together to generate emergent dynamics and behavior.

1064

1065

## 1066 METHODS

1067

### 1068 High-speed remote scanning light-sheet microscopy

1069 In our high-speed light-sheet microscope, we employed a remote refocusing strategy to rapidly scan the  
1070 focal plane at hundreds of hertz without physically moving the detection objective.

1071 For the microscope's detection arm, we used a high NA objective lens (OL1, f=9mm, NA=1.0,  
1072 XLUMPLFLN20XW, Olympus) to efficiently gather emitted fluorescence. The fluorescent light passes a  
1073 4F system consisting of two tube lenses (L1, f=200mm, TTL200MP, Thorlabs; L2, f=150mm, TTL200-A  
1074 + 2× AC508-750-A, Thorlabs), and then is directed into a polarized beam splitter (PBS, PBS241, Thorlabs).

1075 The polarized light beam deflected by the PBS propagates through a quarter wave plate (QWP, AQWP10M-  
1076 580, Thorlabs) and then a remote objective lens (OL2, f=9mm, NA=0.8, UPLXAPO20X, Olympus),  
1077 forming a virtually spherical aberration-free 3D image of the sample. This image is then reflected by a  
1078 lightweight mirror ( $2 \times 2 \times 1$  mm $^3$ , Chroma) glued to a piezo bender actuator (PB4VB2S, Thorlabs). The  
1079 reflected emitted light then revisits the quarter-wave plate (QWP) and the PBS. Adjusting the orientation  
1080 of the QWP allows a 90-degree rotation of the emission light's polarization upon its second encounter with  
1081 the PBS. Consequently, instead of being deflected back, the emission light passes through the PBS,  
1082 subsequently enters a tertiary tube lens (L3, f=176mm, TTL200MP + AC508-1000-A, Thorlabs), and forms  
1083 an in-focus image on its focal plane. A band-pass filter (FF01-571/72-25, Semrock) was positioned between  
1084 the PBS and L3 as an emission filter.

1085 To achieve the kilohertz frame rate essential for imaging the voltage of neurons distributed across entire  
1086 brains, we split and captured the images using two ultrafast cameras (Ximea CB024MG-GP-X8G3, or in  
1087 original prototype form, our customized camera, **Fig. S4**), effectively doubling the camera frame rate. The  
1088 in-focus images produced by L3 were divided into two halves using a knife-edge mirror (KEM, MRAK25-  
1089 P01, Thorlabs), with its edge aligned with the image's central longitudinal axis. The mirror deflected half  
1090 of the image into an ultrafast CMOS camera though a two-component relay system (f=211mm, ACT508-  
1091 1000-A + 3× ACT508-750-A, Thorlabs; f=50mm, Thorlabs TL4X-SAP or Nikon CFI Plan Apo 4X). The  
1092 other half was relayed by an identical system and then imaged by another ultrafast camera of the same  
1093 specifications.

1094 For fluorescence excitation, we built two versions of the light-sheet excitation arm: the first configuration  
1095 for standard, non-light-sheet-pivoting voltage imaging (**Fig. S17a**) and the second configuration with a  
1096 resonant mirror scanner to pivot the light sheet for stripe removal (**Fig. S17b**).

1097 In the first configuration (**Fig. S17a**), a collimated laser beam (515nm, beam diameter ~1.5 mm, Cobolt 06-  
1098 MLD, HÜBNER Photonics) first passed a Powell lens (5 degrees fan angle, Laserline Optics) to form a  
1099 divergent fan of light in the horizontal plane. This fan beam then traveled through a pair of 4f relay lenses  
1100 (RL2, f=50mm, Thorlabs, RL1, f=75mm, Thorlabs) and reached a single-axis galvo mirror (mirror  
1101 aperture=5mm, Saturn 5B, ScannerMAX). The galvo mirror reflected the fan beam to a scan lens (CLS-SL,  
1102 Thorlabs), which focused the light into a horizontal light sheet at its focal plane. Finally, this light sheet  
1103 passed through a 0.25×, reversed microscope composed of a tube lens (ITL200, Thorlabs) and an excitation  
1104 objective lens (Plan Apo Lambda 4x, Nikon) to illuminate the sample. The light sheet illuminated at the  
1105 sample has an approximate width of 1mm, around 20% larger than the fish brain's length. During imaging,  
1106 the galvo mirror scanned the excitation beam vertically, resulting in axial shifts of the light sheet at the  
1107 sample. This galvo mirror can support a sinusoidal scan frequency exceeding 2000 Hz with our desired

1108 scan range. To prevent excitation light from directly entering the fish's eyes, we installed an optical mask  
1109 (3-mm thick glass) with a 900- $\mu\text{m}$  diameter disk-shaped chrome coating (optical density>5,  
1110 PhotomaskPORTAL) on it at the scan lens's focal plane. The optical mask was made by applying a circular  
1111 chromium coating with a diameter of 900  $\mu\text{m}$  on one side of a square glass piece. This glass is 3 mm thick  
1112 and measures 14 mm on each side.

1113 The second configuration (**Fig. S17b**) of the excitation light-sheet arm was constructed based on the first  
1114 configuration's design. Several modifications were made to enable it to rapidly pivot the light sheet for  
1115 stripe removal. First, a resonant mirror scanner (resonant frequency=8 kHz, RESSCAN, Sutter Instrument)  
1116 was installed between the two relay lenses (RL3, RL4). Second, a galvo mirror with a larger, 10-mm  
1117 aperture size (Saturn 9B, ScannerMAX) was used. This larger, 10-mm aperture was required because before  
1118 the excitation light reached the galvo mirror, it was rapidly scanned by the resonant scanner along the  
1119 horizontal axis. This made the excitation light rapidly move back and forth across an ~8-mm range on the  
1120 galvo mirror along the horizontal axis. To ensure the excitation light always was deflected by the galvo  
1121 mirror, a larger mirror aperture was needed. Third, an illumination objective lens (XLFLUOR4X/340,  
1122 Olympus) with a larger numerical aperture (NA=0.28) was used, which allowed a larger pivoting angle.  
1123 Fourth, we changed the focal lengths of the relay lens pair (RL3, f=100mm, achromatic doublet, Thorlabs;  
1124 RL4, f=75mm, achromatic doublet, Thorlabs), to match the excitation beam size to the resonant scanner's  
1125 aperture. Finally, an adjustable mechanical slit (VA100CP, Thorlabs) was installed between RL3 and the  
1126 galvo mirror to control the thickness and divergence of the light sheet. This slit was not required for the  
1127 first light-sheet arm configuration as the light sheet's thickness and divergence was already optimized for  
1128 larval zebrafish by carefully selecting the focal lengths of the optical elements. However, in the second  
1129 light-sheet arm configuration, we found slightly reducing the slit width, thus the light-sheet divergence,  
1130 enhanced the image quality. This is probably because in our stripe removal experiment, the focal plane  
1131 shifted by a larger axial distance of 6.1 $\mu\text{m}$  during each exposure. So compared to using the first light-sheet  
1132 arm configuration, the motion blur was more prominent. When imaging the zebrafish brain, at locations  
1133 near the light-sheet waist (the thinnest location), the motion blur became a more limiting factor and  
1134 consequently the light-sheet thickness became a less limiting factor. This gave us some room to reduce the  
1135 light-sheet's thickness at locations far from the light-sheet waist within the sample, where light-sheet  
1136 thickness was a more limiting factor for image quality, by slightly reducing the light-sheet divergence, at  
1137 the cost of increasing the thickness near the light-sheet's waist.

1138 To upgrade the microscope for enhanced light efficiency, we installed a second remote scanning module,  
1139 identical to the first one, on another side of the PBS (**Fig. 1a**). Each remote scanning module consisted of  
1140 a quarter-wave plate, a remote objective lens, and a piezo-driven remote mirror. To ensure alignment of

1141 images from the two modules on the image sensors during volumetric imaging, we implemented a two-step  
1142 calibration process using a 3D fluorescent bead sample. In the first step, we adjusted the X-Y positions  
1143 (perpendicular to its optical axis) of the second remote objective lens to align the two fluorescent bead  
1144 images across a series of static z-planes (**Fig. S1**). This alignment achieved sub-pixel accuracy across a  
1145 200- $\mu\text{m}$  thick volume. In the second step, while the microscope was running, we iteratively adjusted the  
1146 local values of the second piezo bender's driving signals to synchronize the image focus of the second  
1147 module with that of the first module, on a plane-by-plane basis. This step resembled the process to  
1148 synchronize the axial scanning of the light sheet with the movement of the first remote mirror.

1149

## 1150 **Volumetric scanning control and hardware synchronization**

1151 To achieve high-frequency scanning of the remote mirror, we used an open-loop controlled piezo bender  
1152 actuator. To address the hysteresis of the piezo, we rapidly measured the mirror's motion using a customized  
1153 microscope and adjusted the piezo's control signals via LabVIEW software. The mirror's motion was  
1154 captured at a rate of 70000 Hz by a line camera through a 20 $\times$  microscope. For precise measurement of the  
1155 mirror's shifts, we 3D printed a tiny imaging target with fine grid patterns using two-photon polymerization  
1156 and attached it to the side of the mirror. While the mirror's movement was being monitored, we adjusted  
1157 the piezo's control signals, especially the amplitudes and phases of its high-order sinusoidal components,  
1158 to counteract the hysteresis. By doing this, we could calibrate the mirror's movement and match it to the  
1159 desired waveform. The adjustments were made until the discrepancy between the observed and the intended  
1160 waveforms was less than 0.1% of the total scanning span.

1161 For improved uniformity in camera frame intervals, we used non-sinusoidal scanning. Specifically, we  
1162 added sinusoidal waves with odd-integer multiple frequencies (e.g., 602.4 Hz, 1004 Hz) to the volume scan  
1163 rate (200.8 Hz). This allowed us to design a remote mirror scanning curve resembling a triangle wave up  
1164 to its 3rd order Fourier transform. This waveform, in comparison to a basic sinusoidal one, facilitates more  
1165 even axial scanning of the sample. Our tests indicated that the piezo scanner exhibited high displacement  
1166 consistency when driven by periodic voltage waveforms (with a max deviation of less than 0.5% over a  
1167 minute) in an open-loop control. This ensured long-term stable scanning of the fish brain.

1168 Scanning the remote mirror corresponds to scanning the microscope's focal plane. For consistent in-focus  
1169 imaging, the light sheet must remain overlapped with the scanning focal plane beneath the detection  
1170 objective lens. To align the light sheet with the focal plane, we introduced a 40- $\mu\text{s}$  light-sheet pulse with a  
1171 specific time delay relative to each scan cycle while the remote mirror and the galvanometer were in  
1172 operation. The short excitation pulses temporally "sampled" a stationary image plane on the camera. By

1173 adjusting the control signals of the galvanometer at the exact moments of the light sheet pulse, we ensured  
1174 the “sampled” plane was in-focus. Repeating this process with various time delays allowed the light sheet  
1175 to coincide with the focal plane throughout the whole scanning process.

1176 Within a full scan cycle of 4980 µs, which comprising both upward and downward scans, the 30 planes of  
1177 the zebrafish brain were imaged in an interleaved sequence (**Fig. 1c**). To mitigate the blur induced by  
1178 continuous axial scanning during exposure, the light sheet was pulsed for short durations of 40 µs during  
1179 an exposure of each image plane. The timings of the laser pulses were calibrated to ensure uniform sampling  
1180 along the axial axis. The exposure of individual camera frames was synchronized with the light-sheet pulses.  
1181 To ensure the exposure time comprehensively encompassed the excitation period, the camera exposure time  
1182 was set to be 10 µs longer than the light sheet pulse’s duration and the relative timing of the exposure to  
1183 the light sheet pulse was carefully adjusted.

1184 For high-speed, low-latency, coordinative control of various hardware components in our microscope, a  
1185 real-time LabVIEW program was developed and implemented in a compactRIO system equipped with an  
1186 FPGA (cRIO-9038, National Instruments). This program enables simultaneous analog and digital outputs  
1187 through I/O modules (NI-9262, NI-9401, National Instruments). The output signals were updated every 4  
1188 µs, one tenth of the exposure time for each frame, ensuring control precision. These output signals were  
1189 repeated every 4980 µs, corresponding to a volumetric scan rate of 200.8 Hz.

1190

## 1191 **Ultrafast camera system**

1192 The custom camera uses the Gpixel GSPRINT4521/10/02 image sensors. The camera system’s hardware  
1193 employs a two-board stacked design, comprising the TOP and BOTTOM boards (**Fig. S4a**). The TOP board  
1194 (**Fig. S4b**), an 18-layer printed circuits board (PCB), houses the image sensor chip and a Xilinx Spartan 6  
1195 FPGA (Opal-Kelly XEM6010) used for camera control and acquisition trigger synchronization. The TOP  
1196 board accommodates 144 pairs of LVDS lines for high-speed data output from the image sensor. These  
1197 LVDS line trace lengths are carefully matched to minimize propagation delays during data transmission,  
1198 operating at 1.2 Gbps/pair in double data rate (DDR) format. The data lines are connected to the BOTTOM  
1199 board via two high-pin count FPGA mezzanine card (FMC) connectors.

1200 The BOTTOM board (Numato Nereid K7) contains a Xilinx Kintex-7 FPGA, which buffers the high-speed  
1201 data from the image sensor and transmits it to the host computer. Each LVDS’ line data delays are measured  
1202 relative to the data clock at power-up. This delay is then compensated at the FPGA side to ensure data  
1203 integrity at receiving high-speed data stream at 1.2Gbps. The received data are buffered and re-arranged  
1204 using the onboard RAM, before transmission to the host computer using a PCIe link. The PCIe

1205 communication firmware is modified based on open-source projects: RIFFA28 and Open-Ephys ONIX29.  
1206 The host PC receives the data using an ANSI-C API from Open-Ephys ONIX<sup>94</sup>. The data is displayed, and  
1207 storage is designed using the Bonsai<sup>95</sup> reactive programming language.

1208 The custom camera satisfied our design requirements of spatiotemporal resolution (>6000 FPS with  
1209 258×1280) and noise (< 7e-). The only drawback is its large size as the camera prototype requires the PC  
1210 to be placed nearby to access the PCIe slot. This could be solved in the future by adopting existing PCIe  
1211 cable connectors, such as the Molex iPass connector system.

1212 Commercially available cameras using GSPRTING 4521/10/02 sensors became available near the end of  
1213 our custom camera's development. We found that both our custom camera and the commercial camera  
1214 (Ximea CB024MG-GP-X8G3) had the same readout noise performance at our microscope's speed  
1215 specification. This was quantified using root-mean-square noise measurement in dark, which is calculated  
1216 by taking the standard deviation of the pixel's values with no incoming light.

1217

## 1218 **Transgenic zebrafish line construction and transient ASAP5-Kv expression**

1219 The Tg(HuC:Gal4; 3×UAS:Positron2-Kv); nacre and Tg(HuC:Gal4; 2×UAS:Positron2-Kv); nacre  
1220 transgenic zebrafish lines were generated through embryonic micro-injections using the Tol2 transposase  
1221 system<sup>31</sup>. We designed the Positron2-Kv plasmids for micro-injection and synthesized the plasmids through  
1222 a company (Epoch). In our design, DNA constructs consisting of tandemly linked copies of UAS  
1223 sequences<sup>54</sup>, the Positron2 gene, and a Kv2.1 soma-targeting sequence<sup>56</sup> were inserted between the two  
1224 Tol2 arms in a Tol2 plasmid vector<sup>53</sup>. We also inserted Kir2.1 and ER export sequences between the  
1225 Positron2 gene and the Kv2.1 sequence to facilitate membrane trafficking<sup>96</sup>. The DNA sequences of the  
1226 Positron2-Kv constructs are provided in the **Supplementary Table 3**. To construct the Positron2-Kv fish  
1227 line, the synthesized Tol2 plasmids (40 ng/μL) were co-injected with transposase mRNA (synthesized using  
1228 SP6 Transcription Kit, ThermoFisher) into single-cell stage zygotes from Tg(HuC:Gal4); nacre transgenic  
1229 fish. At 3 days post-fertilization (d.p.f.), zebrafish embryos were incubated in fish facility water containing  
1230 3 μM JF<sub>525</sub>-HaloTag for two hours. Residual dye molecules were then gently washed off using fresh fish  
1231 facility water before the embryos were visually screened for green fluorescence under a fluorescence  
1232 stereoscope. Fish larvae exhibiting fluorescence, known as F0 fish, were isolated and raised to maturity.  
1233 Once they reached 3 months post-fertilization, these F0 fish were out-crossed with either Tg(HuC:Gal4);  
1234 nacre or nacre adult fish. Their progeny was stained with JF<sub>525</sub>-HaloTag dye solution and screened at 3-4  
1235 d.p.f. Fish larvae with pan-neuronal fluorescence were selected and raised to establish a transgenic line.

1236 To transiently express ASAP5-Kv in the larval zebrafish brain, we injected DNA plasmids containing the  
1237 2×UAS:ASAP5-Kv construct flanked by Tol2 transposon arms, together with Tol2 transposase mRNA,  
1238 into single-cell stage zygotes of Tg(HuC:Gal4); nacre zebrafish. At 3 d.p.f., the injected embryos were  
1239 screened for fluorescence to identify positive larvae. These positive larvae were then paralyzed and  
1240 embedded in agarose for imaging at 5 d.p.f.

1241

#### 1242 **Larval zebrafish preparation for imaging**

1243 Pan-neuronally labeled larval zebrafish at 5-6 d.p.f. were embedded and imaged under our high-speed  
1244 microscope. For Positron2-Kv fluorescence labeling, the fish were incubated in JF<sub>525</sub>-HaloTag ligand dye  
1245 solution for two hours prior to imaging. We tried to minimize the time gap between staining and imaging,  
1246 thereby reducing the likelihood of having neurons that were born post-staining and remained unlabeled.  
1247 Subsequent screening identified and isolated the positive fish for imaging. To mitigate motion-induced  
1248 artifacts, we paralyzed the fish by briefly incubating the fish in fish facility water containing 0.3 mg/mL  
1249 pancuronium bromide (Sigma) until the fish showed no movement in response to tactile stimuli applied  
1250 using closed forceps tips. Then the fish was mounted on a 3D-printed holder (**Fig. S28**) in 3% low-melting  
1251 agarose (Sigma), all within a petri dish (**Fig. 1d**). The holder design allowed the fish's torso to be cradled  
1252 within a groove and the fish's tail end extended out of the holder. Upon the solidification of the agarose,  
1253 fresh fish facility water was added into the petri dish, and agarose around the fish's head, especially agarose  
1254 on the side intended for light-sheet illumination, was carefully removed using forceps. The fish's body was  
1255 still restrained in agarose. Following this, the holder, along with the embedded fish, was transferred to a  
1256 3D-printed sample chamber (**Fig. S28**). The chamber was designed with transparent glass coverslip walls  
1257 and filled with fish facility water. The holder was adhered to the inside of the chamber using tiny magnets.  
1258 The sample chamber was attached to a 3D translation stage under the detection objective lens for imaging.  
1259 All procedures related to zebrafish husbandry and handling were conducted in accordance with the US  
1260 National Institutes of Health Guide for the Care and Use of Laboratory Animals and approved by the MIT  
1261 Committee on Animal Care (protocol number: 1221-100-24).

1262

#### 1263 **Imaging the spontaneous voltage activity and the voltage activity in response to light stimulation 1264 distributed across the entire brains**

1265 Spontaneous voltage activity of neurons distributed across the entire zebrafish brain was captured at a  
1266 volume rate of 200.8 Hz for 35s in an imaging trial, which produced approximately 250 GB image data.  
1267 For a volumetric scan, each brain slice was illuminated with a light sheet for a duration of 40 μs. The light

1268 sheet had a temporal power of 43 mW, corresponding to an average excitation power of 10.4 mW on the  
1269 sample during imaging.

1270 We recorded activity of **neurons distributed across the entire zebrafish brain** in response to light stimulation  
1271 using the same settings as the spontaneous activity recording, with the only difference being that the fish  
1272 was exposed to the light stimulus during imaging. For the light stimulation, we focused the light from a  
1273 405-nm LED (M405L4, Thorlabs) onto the fish, producing a light spot of an approximate diameter of 5  
1274 mm. The measured intensity of this light was  $0.6 \text{ mW/mm}^2$ . To avoid interference on recorded images from  
1275 the long-wavelength emissions of the LED, the LED light was passed through a 450 nm short-pass filter  
1276 (FELH0450, Thorlabs). The light stimulus was turned on 13s post-laser activation, lasting for a duration of  
1277 10 seconds, and then subsequently turned off until the 35s imaging trial ended. To diminish possible effects  
1278 of sensory adaptation, we kept the fish in the dark for 20 minutes between consecutive imaging trials with  
1279 light stimulation.

1280

### 1281 **Neuron density estimation**

1282 Based on the literature<sup>43</sup>, for a 7-dpf zebrafish, there are on average 78000 neurons in a volume of  
1283 approximately  $0.20 \text{ mm}^3$ . Assuming the neurons are distributed evenly, we can calculate the volume  
1284 occupied per neuron as  $2.6 \times 10^{-6} \text{ mm}^3$ . If we assume each neuron occupies a cubic volume, then the length  
1285 of each side of this cube is the cube root of the volume per neuron, which is  $14 \mu\text{m}$ . This can be interpreted  
1286 as the average distance between the centroids of neurons in the zebrafish brain.

1287

### 1288 **Data processing**

1289 Pre-processing: We first parsed the data stream from the camera into 30 videos corresponding to 30 z-stack  
1290 layers. Due to the high data throughput from the camera to the host computer through the PCIe bus (~2.6  
1291 GBps per camera), there were rare occasions of lost frames (drop rate: roughly 1 per every 2000 frames, or  
1292 0.05%) attributed to data buffer overflow. Frame drops rarely occurred for two consecutive frames. To  
1293 rectify a lost frame, we simply replaced it with linearly interpolated pixel data from the frames immediately  
1294 preceding and following it.

1295 We first synchronized videos from the two cameras by time-aligning them at the light-sheet excitation laser  
1296 onset at the beginning of the experiment. We then merged individual frames from the two cameras into a  
1297 single frame for each time point. Each C-FOV captures approximately half of the fish's brain from the  
1298 midline to the left and right lateral sides (**Fig. S5**). The combined frame size is  $512 \times 1280$  pixels, with C-

1299 FOV encompassing the entire brain. Lastly, we concatenated corresponding z-stack frames from successive  
1300 trials in time into a single video for motion correction, ROI segmentation, and temporal trace extraction.

1301 Motion correction: We applied motion correction to each z-stack layer separately using a rigid motion  
1302 correction method (NoRMCorre<sup>32</sup>).

1303 ROI segmentation: We trained a deep learning model to automatically segment regions-of-interest (ROIs)  
1304 corresponding to putative neurons using the deep network models in Cellpose 3.0<sup>64</sup>. To prepare the training  
1305 data, motion correction was first applied to the video of each z-layer, followed by generating a static image  
1306 by averaging the first 100 frames of the same layer. These static images were then spatially upsampled and  
1307 interpolated by a factor of 2 in the x-y direction to enhance pixel density, facilitating easier cell labeling in  
1308 the Cellpose 3.0 graphical user interface (GUI).

1309 We first used the pre-trained Cellpose 3.0 model<sup>64</sup>, but realized the model performed poorly on our dataset,  
1310 likely due to challenges with out-of-distribution generalization to our dataset. We therefore manually  
1311 segmented a few thousand neurons and trained our own Cellpose model in the grayscale mode. In our  
1312 manual segmentation process, we identified and outlined objects that were approximately the size of a  
1313 neuron (~6.6  $\mu\text{m}$ ) and had ring-like boundaries due to membrane labeling. Using a "diam\_mean" parameter  
1314 value of 15 (to match the neuron size) and a learning rate of 0.02 (chosen somewhat arbitrarily, but we  
1315 found it allowed the model to converge well during training), we observed that the model could correctly  
1316 segment over 70% neurons after 1000 training epochs, treating the hand annotation as the ground truth.  
1317 During testing, one can adjust parameters including "flow threshold", "cellprob threshold" and "diameter  
1318 pixel" in the Cellpose GUI to increase the number of neurons detected. "Cellprob threshold" and "flow  
1319 threshold" are two parameters controlling how sensitive the model is to detect ROIs<sup>64</sup>. Increasing the  
1320 "flow threshold" or decreasing the "cellprob threshold" can result in more ROIs, but also more false  
1321 positives. "Diameter pixel" refers to the average diameter the model uses to identify ROIs, in pixel units.  
1322 Because increasing the ROI detection sensitivity will also raise the false positive detection rate, a user must  
1323 choose the right balance to minimize the amount of manual correction. For this paper, we chose a "diameter  
1324 pixel" of 18, "flow threshold" of 0.4 and "cellprob threshold" of 0. Diameter pixel of 18 was chosen to  
1325 match the average size of the neuron in our dataset. We noticed that using other values could lead to over  
1326 or under segmentation. "Flow threshold" and "cellprob threshold" were chosen as the default values given  
1327 by the Cellpose GUI. We also adopted their iterative bootstrapping idea<sup>64</sup>, where we trained the model with  
1328 labelled data, and iteratively fed manually-corrected predictions back into the model. In total, training data  
1329 from five fish, comprising >80,000 ROIs, were used in training of our custom CellPose model. The model's  
1330 performance (i.e. the number of ROIs labeled) improved as we expanded the training dataset. Eventually,

1331 it reached a point where adding more training ROIs did not improve the model's performance significantly.  
1332 Therefore, we stopped the training after using 5 fish's ROIs for training, totaling over 80,000 ROIs.

1333 ROI temporal trace extraction: The extracted ROIs are processed by VolPy's temporal trace extraction  
1334 pipeline, which is composed of background removal, trace denoising and spike extraction. We used an  
1335 adaptive threshold for spiking detection in VolPy. To avoid the possible effect of Volpy filters on the edge  
1336 of the signal, we cut the first 1s and last 1s of the 35s Volpy extracted time-series from subsequent analysis.

1337 Artifact removal: After extracting putative spiking activity from each Region of Interest (ROI), we  
1338 employed the Uniform Manifold Approximation and Projection (UMAP) algorithm to identify and remove  
1339 ROIs that may have been influenced by recording artifacts, such as those caused by excitation intensity  
1340 variation due to blood flow. To achieve this, we first applied a 250-ms moving Hanning window to each  
1341 ROI's spike raster for smoothing and estimation of its firing rate. The entire recording data was structured  
1342 into an  $N \times D$  matrix, where  $N$  represented the number of ROIs and  $D$  represented the number of temporal  
1343 samples. This matrix was fed to the UMAP algorithm and transformed into an  $N \times 2$  matrix, where each  
1344 ROI was represented as a point within a 2-dimensional manifold. We then employed the Density-Based  
1345 Spatial Clustering of Applications with Noise (DBSCAN) algorithm to identify clusters within the 2D  
1346 representations of ROIs, effectively sorting ROIs with similar temporal spiking patterns into groups. We  
1347 then visually identified the ROI cluster that was most well-separated from the main cluster in the 2D UMAP  
1348 representation. We then labeled the ROIs of the identified cluster with a unique cluster ID and removed  
1349 them from the total set of ROIs. The remaining ROIs were then mapped and clustered again using UMAP  
1350 DBSCAN for the next iteration. The iteration was continued until the 2D UMAP representation became  
1351 near Gaussian distributed. Following this clustering step, we scrutinized the temporal patterns and spatial  
1352 distributions of ROIs within each cluster to detect any indications of artifacts resulting from recording  
1353 imperfections, which were excluded from further analysis. Our criteria to identify an artifact-contaminated  
1354 cluster were: 1) the temporal traces of the cluster's ROIs exhibited synchronous pulse-like patterns (**Figure**  
1355 **S11**, orange arrows); 2) the spatial distribution of the cluster's ROIs had the same spatial features as the  
1356 artifact moving stripes or shadows, i.e., the ROIs were concentrated in a region (or regions) that is narrow  
1357 in the x and z axis ( $< 100 \mu\text{m}$ ) and spanned from a certain location (possibly in the middle of the brain, as  
1358 there are blood vessels) to the edge of the brain opposite to the edge of light sheet incidence, along the y  
1359 axis (light sheet illumination axis) (**Figure S11**, green arrows). A cluster was identified as an artifact cluster  
1360 only when it satisfied both these two criteria. The remaining ROIs, after moving stripe artifact removal,  
1361 were putatively treated as neurons, sorted into different groups using the same UMAP DBSCAN algorithm,  
1362 and awaited further analysis.

1363 Clustering based on neuron putative spiking activity: After removing all the ROIs with artifacts, we  
1364 clustered the rest of the ROI again using UMAP and DBSCAN, based on their temporal characteristics.  
1365 This analysis revealed a specific group of neurons (Group 1, **Figure 3b**, blue) that demonstrated increased  
1366 spiking activity following the onset of 405 nm light stimulation during two trials. Notably, this response  
1367 was triggered by the light turning ON, but not OFF, aligning with previous findings from calcium imaging  
1368 studies<sup>81</sup>. Another cluster (Group 2, **Figure 3b**, orange) exhibited recurring burst activity throughout the  
1369 recordings, which appeared uncorrelated with the stimulus. The remaining neurons, which lacked distinct  
1370 temporal patterns, were classified as Group 3 (**Figure 3b**, gray).

1371

### 1372 **Normalized temporal standard deviation map (NTSDM)**

1373 To better visualize the moving stripes' distributions in of the brain, we generated a normalized temporal  
1374 standard deviation map (NTSDM) of each time-series recording. To obtain this map, we first corrected for  
1375 photobleaching by normalizing each frame's intensity using the mean intensity of the frame. Then we  
1376 calculated the standard deviation of each pixel's intensity over time, and normalized this standard deviation  
1377 map by dividing it by the square root of each pixel's temporal mean intensity, which corresponds to the  
1378 theoretical shot noise. The rationale behind this calculation is:

1379 The temporal standard deviation (TSD) of a pixel's intensity trace is contributed to by shot noise, real neural  
1380 activity, moving-stripe induced temporal artifacts, and other noise (e.g., camera noise) whose contribution  
1381 assumingly remains unchanged during an imaging trial. In our imaging, each pixel within a neuron ROI on  
1382 average detected ~250 photons per frame, providing a shot noise more than two times of the camera noise  
1383 (~7e-). Assuming there was no neural activity or moving stripe, each pixel's noise could be approximated  
1384 using its shot noise. We calculated each pixel's noise using its intensity trace's temporal standard deviation.  
1385 Therefore, if there were no neural activity or moving stripe, by normalizing the recording's standard  
1386 deviation map using its shot noise, we would obtain a near solid color map that does not highlight anything.  
1387 In real imaging experiments, both neural activity and moving stripes cause fluctuations in a pixel's intensity  
1388 trace, which increases the standard deviation of the trace and the value in the normalized temporal standard  
1389 deviation map. As the intensity fluctuation caused by moving stripes usually has much higher amplitude  
1390 compared to the fluorescent changes caused by real neural voltage activity (otherwise the moving stripe  
1391 will not be a big issue), these moving stripes will stand out in the normalized temporal standard deviation  
1392 map (NTSDM) as bright stripes along the direction of light-sheet illumination.

1393 We found this NTSDM in general worked well in highlighting the moving stripes in time-series recordings.  
1394 But this method also has some limitations. It neglects low-intensity pixels where shot noise is not dominant.

1395 It also highlights areas that exhibit a lot of neural activity. Its photobleaching correction algorithm might  
1396 also be improved. Probably due to these limitations, the normalized standard deviation maps of the top and  
1397 bottom brain layers showed higher background resembling the shapes of brain sections in the raw images  
1398 (Fig. S14b, top and bottom rows). Despite these limitations, NTSDMs were sufficient for visualizing the  
1399 moving stripe locations and comparing moving stripes in the same layer over time. We did not intend to  
1400 use these maps for any quantitative analysis in this paper.

1401

#### 1402 **Simulation of ASAP5-Kv neural traces at different imaging rates**

1403 For simulation of ASAP5-Kv neural traces at different imaging rates, we used the spikes detected in the  
1404 1000-Hz Positron2-Kv fish imaging data as the ground truth. To simulate ground truth voltage traces, we  
1405 convolved these spikes with an action potential curve generated using the Hodgkin–Huxley model. Each  
1406 action potential curve has a duration of 0.5 ms (full width at half maximum). We chose this short 0.5 ms  
1407 duration to represent faster action potentials, as action potentials with longer durations generate wider  
1408 fluorescent spikes and are easier to detect. To model the fluorescent traces in response to these voltage  
1409 traces, we used the kinetic parameters of ASAP5-Kv at room temperature according to<sup>61</sup>. These parameters  
1410 include the fast depolarization time constant  $\tau_{D,fast} = 2.6\text{ ms}$ , the slow depolarization time constant  
1411  $\tau_{D,slow} = 45.3\text{ ms}$ , the fast repolarization time constant  $\tau_{R,fast} = 4.3\text{ ms}$ , and the slow repolarization time  
1412 constant  $\tau_{R,slow} = 55.9\text{ ms}$ , along with their respective proportions in the biphasic depolarization and  
1413 repolarization processes. We calculated the fluorescent traces  $F(t)$  using the following formula with a time  
1414 step of 0.1 ms.

$$1415 \quad F(t) = \int_0^t \frac{dV(\tau)}{d\tau} \cdot R(t - \tau) d\tau \quad (1)$$

$$1416 \quad R(t) = \begin{cases} 1 - a_1 \exp\left(-\frac{t}{\tau_{D,fast}}\right) - (1 - a_1) \exp\left(-\frac{t}{\tau_{D,slow}}\right), & \text{if } \frac{dV}{dt} \geq 0 \\ a_2 \exp\left(-\frac{t}{\tau_{R,fast}}\right) + (1 - a_2) \exp\left(-\frac{t}{\tau_{R,slow}}\right) - 1, & \text{if } \frac{dV}{dt} < 0 \end{cases} \quad (2)$$

1417 Here  $V(t)$  is the simulated voltage traces,  $t$  is time, and  $a_1$  (0.92) and  $a_2$  (0.75) denote the proportions of  
1418 the fast exponential components in the depolarization and the repolarization processes, respectively. We  
1419 assumed ASAP5-Kv's fluorescence to be linearly related to the neural voltage and set the scaling factor to  
1420 1. The 1000-Hz and 200-Hz traces were generated by sampling discrete points in the high temporal  
1421 resolution (0.1 ms) traces at 1-ms and 5-ms intervals, respectively. Prior to spike detection, we added

1422 Gaussian noise to the 1000-Hz and 200-Hz traces, with the noise's standard deviation equal to 1/10 of the  
1423 maximum spiking amplitude of the traces.

1424

1425

## 1426 DATA AVAILABILITY

1427 All data and results for a representative fish (Fish A) after ROI segmentation and VolPy analysis—including  
1428 extracted raw neural traces, ROI positions, and detected spikes—are publicly available at [https://mitprod-my.sharepoint.com/:f/g/personal/zgwang\\_mit\\_edu/EpNWh5wfTQhKj19x98XoWAwB8IEEceKJEC4p8UXJ592mmg?e=aQ3Xbw](https://mitprod-my.sharepoint.com/:f/g/personal/zgwang_mit_edu/EpNWh5wfTQhKj19x98XoWAwB8IEEceKJEC4p8UXJ592mmg?e=aQ3Xbw). Additionally, the raw recordings of Fish A during visual stimulation  
1429 experiments and the raw recordings of the fish shown in Fig. 2 during spontaneous activity imaging, along  
1430 with the CAD files for the sample holder and imaging chamber, can be accessed at the same repository. All  
1431 other raw datasets used in this study are available upon request.  
1432

1433

1434

1435

## 1436 CODE AVAILABILITY

1437 The codes used to control the microscope and to analyze the image datasets, as well as the custom-trained  
1438 Cellpose model, are available at <https://doi.org/10.5281/zenodo.14920628>.

1439

1440

## 1441 ACKNOWLEDGMENTS

1442 We thank Peter So and Florian Engert for kind suggestions and feedback on this project. We thank Yong  
1443 Qian for assistance in testing different GEVIs. We thank Adam E. Cohen and Urs Lucas Böhm for helpful  
1444 discussions. We thank Seungjae Han, Minho Eom, and Young-Gyu Yoon for testing our data with their  
1445 denoising algorithms. We thank Ruihan Zhang for help with data analysis. We thank Mriganka Sur for  
1446 generously lending us the resonant scanner. Z.W. acknowledges Alana Fellowship. J.Z. acknowledges  
1447 funding by NIH R21EY028381-01. W.G. was funded by a Picower Institute Innovation Fund. E.S.B. was  
1448 supported by Lisa Yang, Ashar Aziz, K. Lisa Yang and Hock E. Tan Center for Molecular Therapeutics at  
1449 MIT, John Doerr, Jed McCaleb, James Fickel, HHMI, NIH 1R01MH123977, NIH 1R01AG070831, NIH  
1450 RF1NS113287, NIH R01MH122971, NIH R01DA029639, NIH UF1NS107697, and NIH 1R01MH114031.

1451

1452

1453 **AUTHOR CONTRIBUTIONS**

1454 Z.W., J.Z., and E.S.B. conceived the project and made high-level design of the experiments. Z.W. designed  
1455 the microscope, ran the Zemax simulation, built the imaging hardware, and wrote the control software. J.Z.  
1456 designed and built the customized ultrafast camera and developed its acquisition software. Z.W. constructed  
1457 the transgenic GEVI fish lines with A.A. Z.W. performed the imaging experiments with J.Z. and L.Z. J.Z.,  
1458 Z.W., P.S., and L.Z. processed and analyzed the data. W.G. ran the clustering analysis. D.D. trained the  
1459 Cellpose model. A.A. performed the fish immunostaining experiment. T.H., S.R., J.Z., and Z.W. manually  
1460 annotated ROIs in the fish data. Z.W., J.Z., and E.S.B. wrote the paper with input from all the authors.  
1461 E.S.B. and M.A.W. supervised the project.

1462

1463

1464 **REFERENCES**

- 1465 1. Ahrens, M. B., Orger, M. B., Robson, D. N., Li, J. M. & Keller, P. J. Whole-brain functional imaging  
1466 at cellular resolution using light-sheet microscopy. *Nat. Methods* **10**, 413–420 (2013).
- 1467 2. Chen, T.-W. *et al.* Ultrasensitive fluorescent proteins for imaging neuronal activity. *Nature* **499**, 295–  
1468 300 (2013).
- 1469 3. Zhang, Y. *et al.* Fast and sensitive GCaMP calcium indicators for imaging neural populations. *Nature*  
1470 **615**, 884–891 (2023).
- 1471 4. Ahrens, M. B. *et al.* Brain-wide neuronal dynamics during motor adaptation in zebrafish. *Nature* **485**,  
1472 471–477 (2012).
- 1473 5. Tomer, R. *et al.* SPED light sheet microscopy: Fast mapping of biological system structure and  
1474 function. *Cell* **163**, 1796–1806 (2015).
- 1475 6. Prevedel, R. *et al.* Simultaneous whole-animal 3D imaging of neuronal activity using light-field  
1476 microscopy. *Nat. Methods* **11**, 727–730 (2014).
- 1477 7. Vladimirov, N. *et al.* Light-sheet functional imaging in fictively behaving zebrafish. *Nat. Methods* **11**,  
1478 883–884 (2014).

- 1479 8. Portugues, R., Feierstein, C. E., Engert, F. & Orger, M. B. Whole-brain activity maps reveal  
1480 stereotyped, distributed networks for visuomotor behavior. *Neuron* **81**, 1328–1343 (2014).
- 1481 9. Chhetri, R. K. *et al.* Whole-animal functional and developmental imaging with isotropic spatial  
1482 resolution. *Nat. Methods* **12**, 1171–1178 (2015).
- 1483 10. Royer, L. A. *et al.* Adaptive light-sheet microscopy for long-term, high-resolution imaging in living  
1484 organisms. *Nat. Biotechnol.* **34**, 1267–1278 (2016).
- 1485 11. Keller, P. J. & Ahrens, M. B. Visualizing whole-brain activity and development at the single-cell level  
1486 using light-sheet microscopy. *Neuron* **85**, 462–483 (2015).
- 1487 12. Levoy, M., Ng, R., Adams, A., Footer, M. & Horowitz, M. Light field microscopy. in *ACM  
1488 SIGGRAPH 2006 Papers on - SIGGRAPH '06* (ACM Press, New York, New York, USA, 2006).  
1489 doi:10.1145/1179352.1141976.
- 1490 13. Bai, L. *et al.* Volumetric voltage imaging of neuronal populations in the mouse brain by confocal light-  
1491 field microscopy. *Nat. Methods* **21**, 2160–2170 (2024).
- 1492 14. Kunst, M. *et al.* A cellular-resolution atlas of the larval zebrafish brain. *Neuron* **103**, 21-38.e5 (2019).
- 1493 15. Cong, L. *et al.* Rapid whole brain imaging of neural activity in freely behaving larval zebrafish ().  
1494 *Elife* **6**, (2017).
- 1495 16. Yoon, Y.-G. *et al.* Sparse decomposition light-field microscopy for high speed imaging of neuronal  
1496 activity. *Optica* **7**, 1457 (2020).
- 1497 17. Zhang, Z. *et al.* Imaging volumetric dynamics at high speed in mouse and zebrafish brain with confocal  
1498 light field microscopy. *Nat. Biotechnol.* **39**, 74–83 (2021).
- 1499 18. Wu, J. *et al.* Iterative tomography with digital adaptive optics permits hour-long intravital observation  
1500 of 3D subcellular dynamics at millisecond scale. *Cell* **184**, 3318-3332.e17 (2021).
- 1501 19. Hillman, E. M. C., Voleti, V., Li, W. & Yu, H. Light-Sheet Microscopy in Neuroscience. *Annu. Rev.  
1502 Neurosci.* **42**, 295–313 (2019).
- 1503 20. Stelzer, E. H. K. *et al.* Light sheet fluorescence microscopy. *Nature Reviews Methods Primers* **1**, 1–  
1504 25 (2021).

- 1505 21. Corsetti, S., Gunn-Moore, F. & Dholakia, K. Light sheet fluorescence microscopy for neuroscience.
- 1506 *J. Neurosci. Methods* **319**, 16–27 (2019).
- 1507 22. Power, R. M. & Huisken, J. A guide to light-sheet fluorescence microscopy for multiscale imaging.
- 1508 *Nat. Methods* **14**, 360–373 (2017).
- 1509 23. P I (physik Instrumente) L. P-726 PIFOC High-Load Focus Scanner. <https://www.pi-usa.us/en/products/piezo-flexure-nanopositioners/z-nanofocus-piezo-scanners-for-microscope-lenses/p-726-pifoc-high-load-objective-scanner-200380#specification>.
- 1512 24. P I (physik Instrumente) L. PIFOC® Objective & PI<sup>nano</sup>® Sample Scanners for Microscopy. <https://www.pi-usa.us/en/products/more-products/nanopositioning-piezo-flexure-stages/pifoc-objective-pinano-sample-scanners-for-microscopy>.
- 1515 25. Botcherby, E. J., Juskaitis, R., Booth, M. J. & Wilson, T. Aberration-free optical refocusing in high numerical aperture microscopy. *Opt. Lett.* **32**, 2007–2009 (2007).
- 1517 26. Botcherby, E. J., Juškaitis, R., Booth, M. J. & Wilson, T. An optical technique for remote focusing in microscopy. *Opt. Commun.* **281**, 880–887 (2008).
- 1519 27. Fahrbach, F. O., Voigt, F. F., Schmid, B., Helmchen, F. & Huisken, J. Rapid 3D light-sheet microscopy with a tunable lens. *Opt. Express* **21**, 21010–21026 (2013).
- 1521 28. Sparks, H. *et al.* Development a flexible light-sheet fluorescence microscope for high-speed 3D imaging of calcium dynamics and 3D imaging of cellular microstructure. *J. Biophotonics* **13**, e201960239 (2020).
- 1524 29. Dibaji, H. *et al.* Axial de-scanning using remote focusing in the detection arm of light-sheet microscopy. *Res Sq* (2023) doi:10.21203/rs.3.rs-3338831/v1.
- 1526 30. Yang, B. *et al.* Epi-illumination SPIM for volumetric imaging with high spatial-temporal resolution. *Nat. Methods* **16**, 501–504 (2019).
- 1528 31. Yang, B. *et al.* DaXi-high-resolution, large imaging volume and multi-view single-objective light-sheet microscopy. *Nat. Methods* **19**, 461–469 (2022).
- 1530 32. Sapoznik, E. *et al.* A versatile oblique plane microscope for large-scale and high-resolution imaging

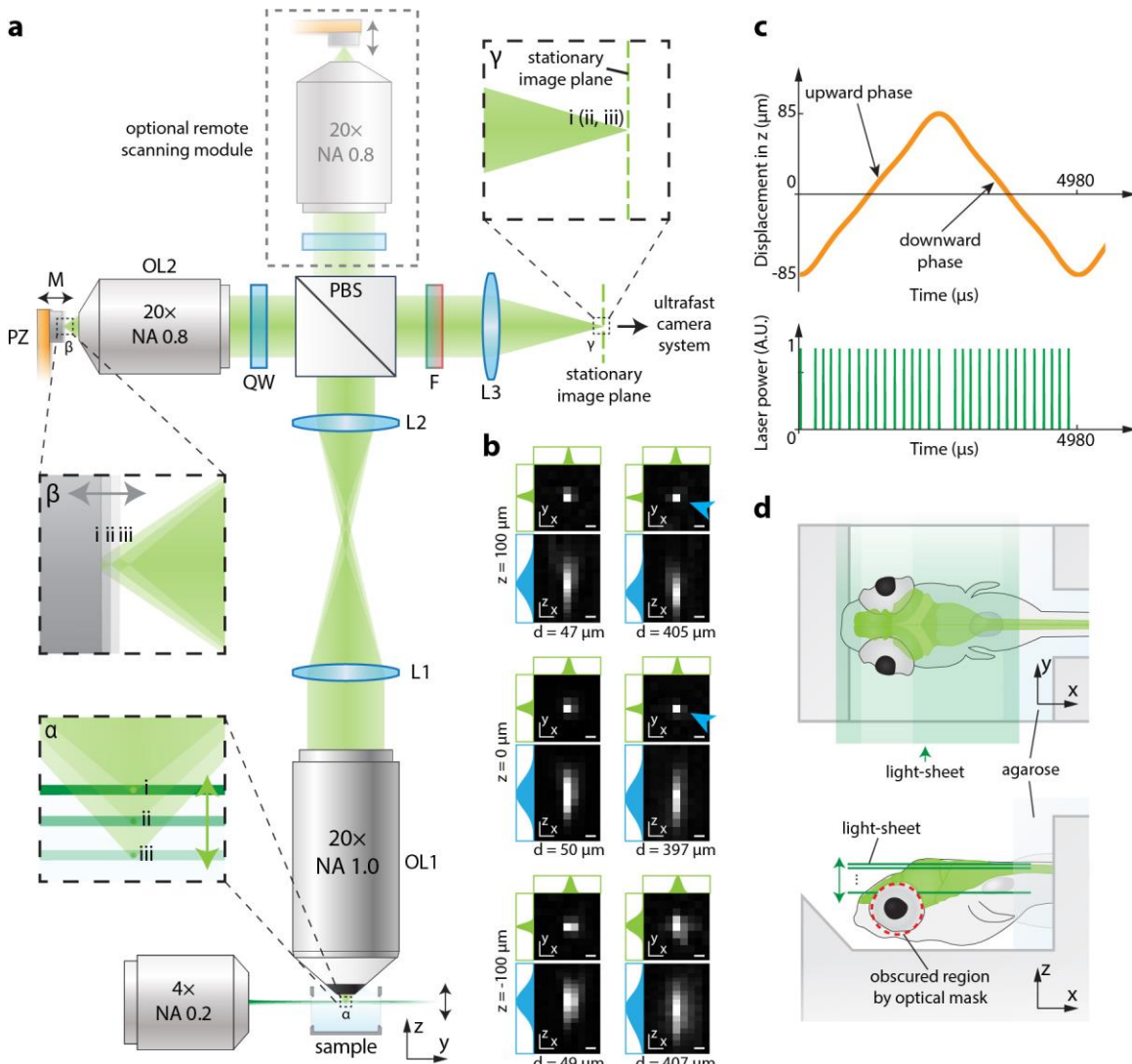
- 1531 of subcellular dynamics. *Elife* **9**, (2020).
- 1532 33. Hoffmann, M. & Judkewitz, B. Diffractive oblique plane microscopy. *Optica* **6**, 1166 (2019).
- 1533 34. Hoffmann, M., Henninger, J., Richter, L. & Judkewitz, B. Brain-wide imaging of an adult vertebrate  
1534 with image transfer oblique plane microscopy. *bioRxiv* 2022.05.16.492103 (2022)  
1535 doi:10.1101/2022.05.16.492103.
- 1536 35. Kumar, M., Kishore, S., Nasenbeny, J., McLean, D. L. & Kozorovitskiy, Y. Integrated one- and two-  
1537 photon scanned oblique plane illumination (SOPi) microscopy for rapid volumetric imaging. *Opt.  
1538 Express* **26**, 13027–13041 (2018).
- 1539 36. Creators Alfred Millett-Sikking<sup>1</sup> Nathaniel H. Thayer<sup>2</sup> Adam Bohnert<sup>2</sup> Andrew G. York<sup>2</sup> Show  
1540 affiliations 1. @Calico 2. @calico. *Calico/Remote\_refocus: Pre-Print*. doi:10.5281/zenodo.1146084.
- 1541 37. Voleti, V. *et al.* Real-time volumetric microscopy of in vivo dynamics and large-scale samples with  
1542 SCAPE 2.0. *Nat. Methods* **16**, 1054–1062 (2019).
- 1543 38. Bouchard, M. B. *et al.* Swept confocally-aligned planar excitation (SCAPE) microscopy for high speed  
1544 volumetric imaging of behaving organisms. *Nat. Photonics* **9**, 113–119 (2015).
- 1545 39. Dunn, T. W. *et al.* Brain-wide mapping of neural activity controlling zebrafish exploratory locomotion.  
1546 *Elife* **5**, e12741 (2016).
- 1547 40. Mu, Y. *et al.* Glia accumulate evidence that actions are futile and suppress unsuccessful behavior. *Cell*  
1548 **178**, 27-43.e19 (2019).
- 1549 41. Chen, X. *et al.* Brain-wide Organization of Neuronal Activity and Convergent Sensorimotor  
1550 Transformations in Larval Zebrafish. *Neuron* **100**, 876-890.e5 (2018).
- 1551 42. Greer, C. J. & Holy, T. E. Fast objective coupled planar illumination microscopy. *Nat. Commun.* **10**,  
1552 4483 (2019).
- 1553 43. Hill, A., Howard, C. V., Strahle, U. & Cossins, A. Neurodevelopmental defects in zebrafish (*Danio  
1554 rerio*) at environmentally relevant dioxin (TCDD) concentrations. *Toxicol. Sci.* **76**, 392–399 (2003).
- 1555 44. HiCAM Fluo. *lambertinstruments.com* <https://lambertinstruments.com/products/hicam-fluo> (2023).
- 1556 45. Kinetix sCMOS camera. *Teledyne Photometrics* <https://www.photometrics.com/products/kinetix->

- 1557 family/kinetix (2019).
- 1558 46. Phil Brooks, F., 3rd, Davis, H. C., Wong-Campos, J. D. & Cohen, A. E. Optical constraints on two-  
1559 photon voltage imaging. *Neurophotonics* **11**, 035007 (2024).
- 1560 47. Born, M. & Wolf, E. *Principles of Optics: Electromagnetic Theory of Propagation, Interference and*  
1561 *Diffraction of Light.* (CUP Archive, 2000).
- 1562 48. Creators Alfred Millett-Sikking1 Andrew York2 Show affiliations 1. @Calico 2. @calico.  
1563 *AndrewGYork/High\_na\_single\_objective\_lightsheet:* Work-in-Progress.  
1564 doi:10.5281/zenodo.3376243.
- 1565 49. Voltron and positron. *Janelia Research Campus* <https://www.janelia.org/open-science/voltron-and-positron>.
- 1567 50. Villette, V. *et al.* Ultrafast Two-Photon Imaging of a High-Gain Voltage Indicator in Awake Behaving  
1568 Mice. *Cell* **179**, 1590-1608.e23 (2019).
- 1569 51. Abdelfattah, A. S. *et al.* Sensitivity optimization of a rhodopsin-based fluorescent voltage indicator.  
1570 *Neuron* **111**, 1547-1563.e9 (2023).
- 1571 52. Kannan, M. *et al.* Dual-polarity voltage imaging of the concurrent dynamics of multiple neuron types.  
1572 *Science* **378**, eabm8797 (2022).
- 1573 53. Kawakami, K. Transposon tools and methods in zebrafish. *Dev. Dyn.* **234**, 244–254 (2005).
- 1574 54. Halpern, M. E. *et al.* Gal4/UAS transgenic tools and their application to zebrafish. *Zebrafish* **5**, 97–  
1575 110 (2008).
- 1576 55. Park, H. C. *et al.* Analysis of upstream elements in the HuC promoter leads to the establishment of  
1577 transgenic zebrafish with fluorescent neurons. *Dev. Biol.* **227**, 279–293 (2000).
- 1578 56. Abdelfattah, A. S. *et al.* Bright and photostable chemogenetic indicators for extended in vivo voltage  
1579 imaging. *Science* **365**, 699–704 (2019).
- 1580 57. Akitake, C. M., Macurak, M., Halpern, M. E. & Goll, M. G. Transgenerational analysis of  
1581 transcriptional silencing in zebrafish. *Dev. Biol.* **352**, 191–201 (2011).
- 1582 58. Scheer, N. & Campos-Ortega, J. A. Use of the Gal4-UAS technique for targeted gene expression in

- 1583 the zebrafish. *Mech. Dev.* **80**, 153–158 (1999).
- 1584 59. Asakawa, K. *et al.* Genetic dissection of neural circuits by Tol2 transposon-mediated Gal4 gene and  
1585 enhancer trapping in zebrafish. *Proc. Natl. Acad. Sci. U. S. A.* **105**, 1255–1260 (2008).
- 1586 60. Schreiter, E. R. *et al.* Optimization of Ace2N based voltage indicators. (3 2023)  
1587 doi:10.25378/janelia.22325446.v1.
- 1588 61. Hao, Y. A. *et al.* A fast and responsive voltage indicator with enhanced sensitivity for unitary synaptic  
1589 events. *Neuron* **112**, 3680-3696.e8 (2024).
- 1590 62. Hildebrand, D. G. C. *et al.* Whole-brain serial-section electron microscopy in larval zebrafish. *Nature*  
1591 **545**, 345–349 (2017).
- 1592 63. Vanwalleghem, G. C., Ahrens, M. B. & Scott, E. K. Integrative whole-brain neuroscience in larval  
1593 zebrafish. *Curr. Opin. Neurobiol.* **50**, 136–145 (2018).
- 1594 64. Stringer, C. & Pachitariu, M. Cellpose3: one-click image restoration for improved cellular  
1595 segmentation. (2024) doi:10.1101/2024.02.10.579780.
- 1596 65. Cai, C. *et al.* VolPy: Automated and scalable analysis pipelines for voltage imaging datasets. *PLoS*  
1597 *Comput. Biol.* **17**, e1008806 (2021).
- 1598 66. Linghu, C. *et al.* Spatial multiplexing of fluorescent reporters for imaging signaling network dynamics.  
1599 *Cell* **183**, 1682-1698.e24 (2020).
- 1600 67. Grossman, N. *et al.* Noninvasive deep brain stimulation via temporally interfering electric fields. *Cell*  
1601 **169**, 1029-1041.e16 (2017).
- 1602 68. Mah, L.-J., El-Osta, A. & Karagiannis, T. C. gammaH2AX: a sensitive molecular marker of DNA  
1603 damage and repair. *Leukemia* **24**, 679–686 (2010).
- 1604 69. Ricci, P. *et al.* Removing striping artifacts in light-sheet fluorescence microscopy: a review. *Prog.*  
1605 *Biophys. Mol. Biol.* **168**, 52–65 (2022).
- 1606 70. Taylor, M. A., Vanwalleghem, G. C., Favre-Bulle, I. A. & Scott, E. K. Diffuse light-sheet microscopy  
1607 for stripe-free calcium imaging of neural populations. *J. Biophotonics* **11**, e201800088 (2018).
- 1608 71. Miccio, L., Memmolo, P., Merola, F., Netti, P. A. & Ferraro, P. Red blood cell as an adaptive

- 1609 optofluidic microlens. *Nat. Commun.* **6**, 6502 (2015).
- 1610 72. Huisken, J. & Stainier, D. Y. R. Even fluorescence excitation by multidirectional selective plane  
1611 illumination microscopy (mSPIM). *Opt. Lett.* **32**, 2608–2610 (2007).
- 1612 73. Sancataldo, G. *et al.* Flexible multi-beam light-sheet fluorescence microscope for live imaging without  
1613 striping artifacts. *Front. Neuroanat.* **13**, 7 (2019).
- 1614 74. Glaser, A. K. *et al.* Multidirectional digital scanned light-sheet microscopy enables uniform  
1615 fluorescence excitation and contrast-enhanced imaging. *Sci. Rep.* **8**, 13878 (2018).
- 1616 75. Ricci, P. *et al.* Fast multi-directional DSLM for confocal detection without striping artifacts. *Biomed.*  
1617 *Opt. Express* **11**, 3111–3124 (2020).
- 1618 76. McInnes, L., Healy, J. & Melville, J. UMAP: Uniform Manifold Approximation and Projection for  
1619 Dimension Reduction. *arXiv [stat.ML]* (2018).
- 1620 77. Ester, M., Kriegel, H.-P., Sander, J. & Xu, X. A density-based algorithm for discovering clusters in  
1621 large spatial databases with noise. in *Proceedings of the Second International Conference on*  
1622 *Knowledge Discovery and Data Mining* 226–231 (AAAI Press, 1996).
- 1623 78. Baden, T. Circuit mechanisms for colour vision in zebrafish. *Curr. Biol.* **31**, R807–R820 (2021).
- 1624 79. Guggiana-Nilo, D. A. & Engert, F. Properties of the Visible Light Phototaxis and UV Avoidance  
1625 Behaviors in the Larval Zebrafish. *Front. Behav. Neurosci.* **10**, 160 (2016).
- 1626 80. Pnevmatikakis, E. A. & Giovannucci, A. NoRMCorre: An online algorithm for piecewise rigid motion  
1627 correction of calcium imaging data. *J. Neurosci. Methods* **291**, 83–94 (2017).
- 1628 81. Bartel, P., Janiak, F. K., Osorio, D. & Baden, T. Colourfulness as a possible measure of object  
1629 proximity in the larval zebrafish brain. *Curr. Biol.* **31**, R235–R236 (2021).
- 1630 82. Chien, M.-P. *et al.* Photoactivated voltage imaging in tissue with an archaerhodopsin-derived reporter.  
1631 *Sci. Adv.* **7**, (2021).
- 1632 83. Isa, T., Marquez-Legorreta, E., Grillner, S. & Scott, E. K. The tectum/superior colliculus as the  
1633 vertebrate solution for spatial sensory integration and action. *Curr. Biol.* **31**, R741–R762 (2021).
- 1634 84. Fornetto, C., Tiso, N., Pavone, F. S. & Vanzi, F. Colored visual stimuli evoke spectrally tuned neuronal

- 1635 responses across the central nervous system of zebrafish larvae. *BMC Biol.* **18**, 172 (2020).
- 1636 85. Tesmer, A. L., Fields, N. P. & Robles, E. Input from torus longitudinalis drives binocularity and spatial  
1637 summation in zebrafish optic tectum. doi:10.1186/s12915-021-01222-x.
- 1638 86. Randlett, O. *et al.* Whole-brain activity mapping onto a zebrafish brain atlas. *Nat. Methods* **12**, 1039–  
1639 1046 (2015).
- 1640 87. Chen, F. *et al.* Nanoscale imaging of RNA with expansion microscopy. *Nat. Methods* **13**, 679–684  
1641 (2016).
- 1642 88. Alon, S. *et al.* Expansion sequencing: Spatially precise *in situ* transcriptomics in intact biological  
1643 systems. *Science* **371**, (2021).
- 1644 89. Piatkevich, K. D. *et al.* A robotic multidimensional directed evolution approach applied to fluorescent  
1645 voltage reporters. *Nat. Chem. Biol.* **14**, 352–360 (2018).
- 1646 90. Shemesh, O. A. *et al.* Temporally precise single-cell-resolution optogenetics. *Nat. Neurosci.* **20**, 1796–  
1647 1806 (2017).
- 1648 91. Freifeld, L. *et al.* Expansion microscopy of zebrafish for neuroscience and developmental biology  
1649 studies. *Proc. Natl. Acad. Sci. U. S. A.* **114**, E10799–E10808 (2017).
- 1650 92. Shen, F. Y. *et al.* Light microscopy based approach for mapping connectivity with molecular  
1651 specificity. *Nat. Commun.* **11**, 4632 (2020).
- 1652 93. Tillberg, P. W. *et al.* Protein-retention expansion microscopy of cells and tissues labeled using  
1653 standard fluorescent proteins and antibodies. *Nat. Biotechnol.* **34**, 987–992 (2016).
- 1654 94. Newman, J. P. *et al.* A unified open-source platform for multimodal neural recording and perturbation  
1655 during naturalistic behavior. *bioRxiv* (2023) doi:10.1101/2023.08.30.554672.
- 1656 95. Lopes, G. *et al.* Bonsai: an event-based framework for processing and controlling data streams. *Front.*  
1657 *Neuroinform.* **9**, 7 (2015).
- 1658 96. Piatkevich, K. D. *et al.* Population imaging of neural activity in awake behaving mice. *Nature* **574**,  
1659 413–417 (2019).
- 1660

1661 **MAIN FIGURES**

1662

1663 **Figure 1. Remote-scanning light-sheet microscopy optimized for voltage imaging of neurons**  
 1664 **distributed across the entire larval zebrafish brain.**

1665 (a) Overview and operational principles of our remote scanning light-sheet microscope design **optimized**  
 1666 **for imaging of the voltage of neurons distributed across the entire larval zebrafish brain.** At the bottom, a  
 1667 sample (an infinitely small fluorescent bead, for purposes of explanation in this figure) in a water chamber  
 1668 is illuminated from one side by a rapidly scanning light sheet from an excitation objective lens. The  
 1669 fluorescence excited by the light sheet is collected orthogonally through a 20 $\times$  high numerical aperture (NA  
 1670 = 1.0) water-immersion objective lens (OL1). The fluorescence light passes through a 4f imaging system  
 1671 composed of two tube lenses (L1 and L2) before entering a polarized beam splitter (PBS). The PBS deflects  
 1672 fluorescence of particular polarization into a quarter wave plate (QW) and a remote objective lens (OL2,

1673 air, 20 $\times$ , NA = 0.8). The remote objective then focuses the fluorescence into real images. These images are  
1674 reflected by a mirror (M) that is translated by a piezo (PZ), and re-imaged by the remote objective. After  
1675 transmitting through the quarter wave plate again, the fluorescence rotates polarization by 90 degrees. The  
1676 fluorescence then passes through the polarized beam splitter and an emission filter (F), before being  
1677 refracted by a tube lens (L3) into real images. The remote piezo actuator (PZ) moves the mirror in synchrony  
1678 with the light sheet, ensuring images of different z-planes at the sample remain in focus at the stationary  
1679 focal plane of L3. These stationary, focused images are directed to an ultrafast camera system for recording.  
1680 The green dashed line at L3's focal plane indicates a stationary image plane of the microscope. An optional  
1681 second remote scanning module (illustrated in the dashed gray box above the PBS) can be added to the  
1682 setup for enhanced light efficiency.

1683 To better illustrate this imaging process, small views at the sample (dashed box  $\alpha$ ), the remote mirror  
1684 (dashed box  $\beta$ ), and the focused images at the focal plane of tube lens L3 (dashed box  $\gamma$ ) are enlarged and  
1685 shown. We show this imaging process at three different time points (i, ii, iii). The enlarged view of dashed  
1686 box  $\alpha$  shows that, at the three time points (i, ii, iii), the light sheet (green horizontal lines, different shades  
1687 indicate different time points) excites an infinitely small fluorescent bead (green dots) at three different z  
1688 locations, and the emitted fluorescence (green cones, only the part entering OL1 is drawn) is collected by  
1689 OL1. Enlarged view of dashed box  $\beta$  shows that, at different time points (i, ii, iii), the remote mirror (gray,  
1690 different shades indicate different time points) translates and reflects the fluorescence light (green cones)  
1691 back to OL2. The mirror's translational motion is synchronized with the light sheet scanning. Enlarged  
1692 view of the dashed box  $\gamma$  shows that the fluorescence light (green cones, overlapped here) at different time  
1693 points (i, ii, iii) is focused on the same image plane (dashed green line).

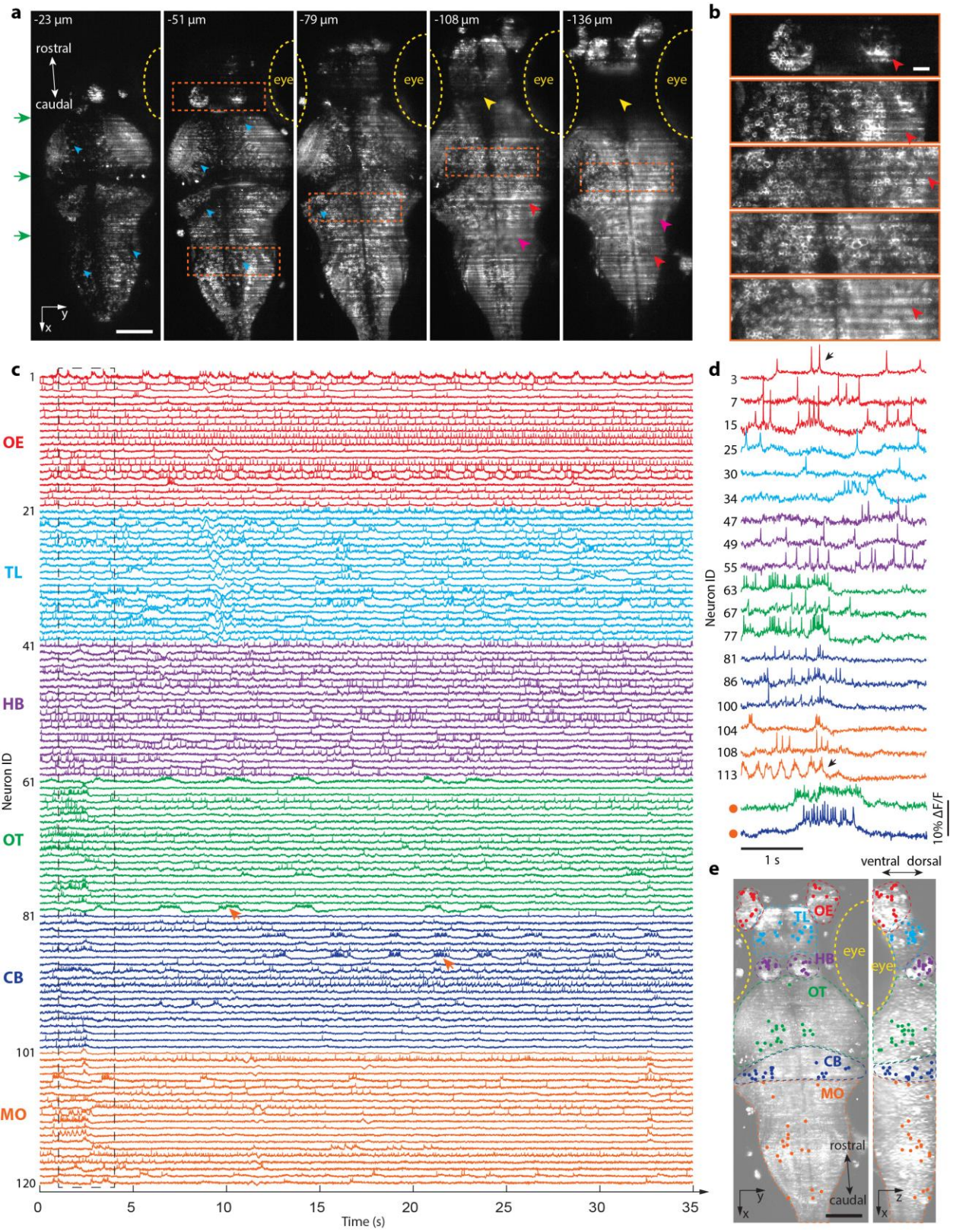
1694 **(b)** The measured point spread functions (PSFs) at different lateral (xy) and axial (z) locations within the  
1695 microscope's 3D-FOV. Each sub-panel displays the xy cross-section (PSF<sub>xy</sub>, top) and the xz cross section  
1696 (PSF<sub>xz</sub>, bottom) of the PSF. We fitted the PSF<sub>xz</sub> using a 2D Gaussian function. The x-axis and y-axis line  
1697 profiles (green) that cross the center of the Gaussian function are shown at the top and left side of the PSF<sub>xy</sub>.  
1698 We fitted the z-axis line profile that crosses the brightest pixel on PSF<sub>xz</sub> using a one-dimensional double  
1699 Gaussian function. The fitted curve (blue) is displayed on the left side of PSF<sub>xz</sub>.

1700 The three rows of sub-panels correspond to PSFs at three axial (z) locations (z=100  $\mu$ m, z=0  $\mu$ m, and z=-  
1701 100  $\mu$ m). At each z, PSFs near the center (left) and the periphery (right) of the 2D-FOV are shown, with  
1702 their distances from the 2D-FOV center denoted as  $d$ . The PSFs were captured as accumulations of 40- $\mu$ s  
1703 exposure images while the microscope's focal plane scanned across a 206  $\mu$ m thick volume at 200.8 Hz.  
1704 Cyan arrows indicate sub-optimally sampled PSF<sub>xy</sub> due to large pixel size (0.73  $\mu$ m). Scale bar: 1  $\mu$ m.

1705   **(c)** Illustration of the synchronization of focal plane scanning (top, orange curve) and flashed light-sheet  
1706 illumination (bottom, green lines). The axial (z) displacement of the microscope's focal plane during a scan  
1707 cycle (4.98 ms) is depicted as the orange curve. The green lines represent 40- $\mu$ s light-sheet pulses for the  
1708 excitation of individual axial planes of the sample. The timing of these pulses was calibrated to ensure the  
1709 imaged z-planes were evenly spaced along the z-axis. The scan cycle consists of an upward phase when the  
1710 microscope's focal plane travels upwards in z, and a downward phase when the focal plane travels  
1711 downwards in z. During each scan cycle, thirty evenly spaced z-planes of the brain were sampled once in  
1712 an interleaved acquisition sequence.

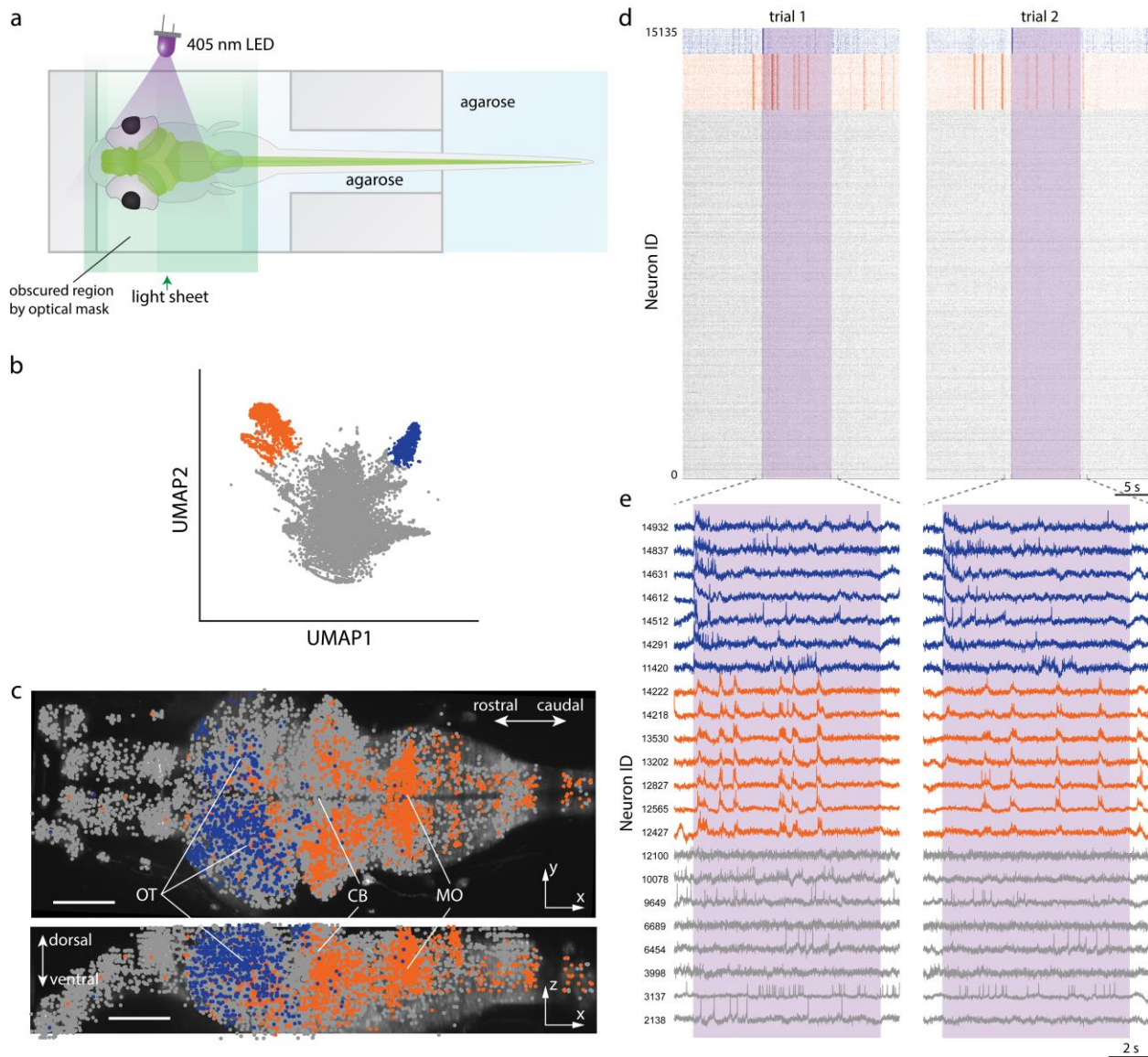
1713   **(d)** Illustration of a mounted larval zebrafish for light-sheet imaging. A larval zebrafish with pan-neuronal  
1714 labeling is immobilized on a 3-D printed holder, with its body restrained in agarose gel and its head exposed.  
1715 A light sheet, illuminated from one side, scans the fish's brain along the z-axis. Excitation light at the fish's  
1716 eye areas is obscured using a circular opaque optical mask (red dashed line). The top view (top of the panel)  
1717 and the side view (bottom of the panel) of the fish are shown.

1718



1720 **Figure 2. Imaging the voltage of neurons across the entire larval zebrafish brain at cellular resolution.**  
1721 **(a)** Stitched raw images from a brain-wide voltage imaging experiment showing 5 zebrafish brain sections  
1722 out of a total of 30. Each section was imaged with 40- $\mu$ s excitation time at a 200.8 Hz imaging rate. From  
1723 left to right, green arrows indicate the direction of light-sheet illumination, cyan arrows show examples of  
1724 unlabeled hollow regions, yellow dashed lines show contours of fish's eyes, yellow arrows indicate brain  
1725 regions that are shadowed by the eyes, red arrows highlight "stripe" patterns of light-sheet illumination,  
1726 magenta arrows indicate blurred regions. Scale bar: 100  $\mu$ m. **(b)** Enlarged views of the areas highlighted  
1727 by dashed rectangles in (a). Single neurons are visually distinguishable in these areas, showcasing the  
1728 microscope's cellular resolution at various depths in the zebrafish brain. Scale bar: 20  $\mu$ m. **(c)** Spontaneous  
1729 activity traces of 120 exemplar neurons from 6 brain regions. Different colors signify traces from various  
1730 regions (referred to in panel e), with olfactory epithelium (OE) in red, telencephalon (TL) in cyan, habenula  
1731 (HB) in purple, optic tectum (OT) in green, cerebellum (CB) in blue, and medulla oblongata (MO) in orange.  
1732 Orange arrows indicate two randomly selected examples of burst activity. **(d)** Zoom-in views of selected  
1733 traces enclosed by the dashed rectangle and the two burst examples in (c). **(e)** Locations of the putative  
1734 neurons (colored dots) whose activity traces are shown in (c), superimposed on the dorsal (left) and lateral  
1735 (right) maximum intensity projections (MIPs) of the imaged brain. The putative neurons' locations are  
1736 marked with the same colors as those of their corresponding activity traces in (c). Brain regions are  
1737 annotated using dashed lines of different colors, indicated as in (c). Scale bar: 100  $\mu$ m.

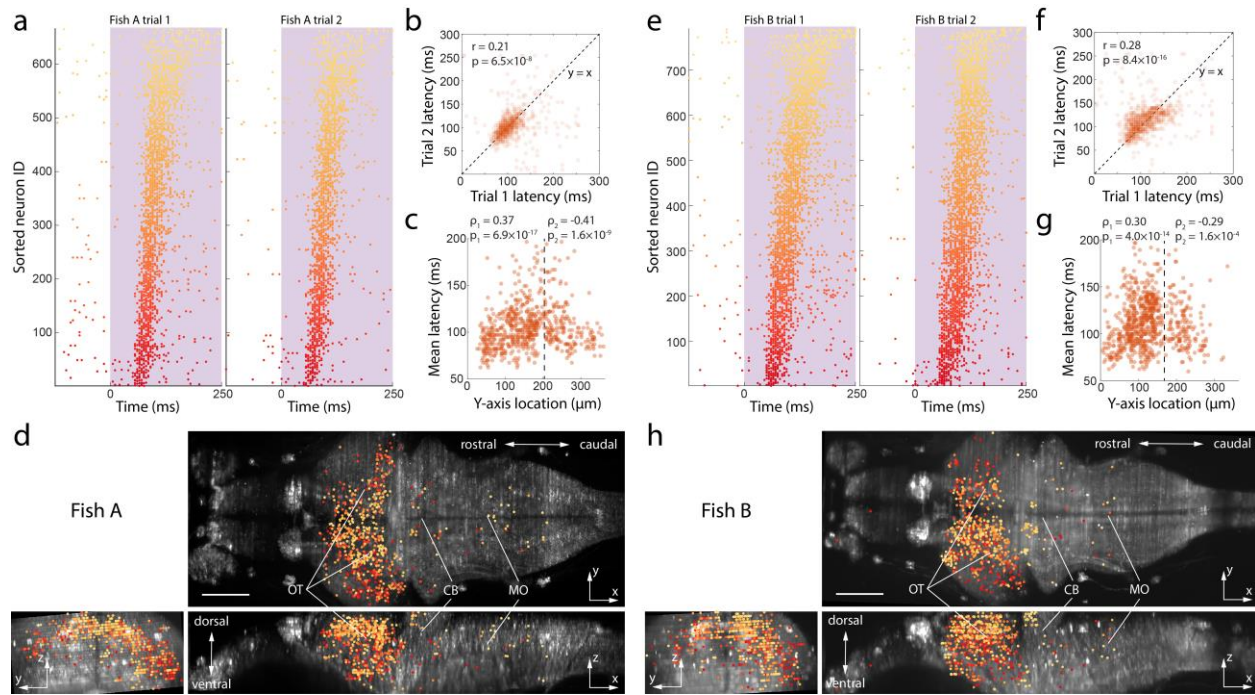
1738



1741 **Figure 3. Imaging the activity of neurons distributed throughout an entire zebrafish brain during**  
 1742 **visual stimulation.** (a) Light stimulation turns on at a lateral side (here illustrated from the right side, but  
 1743 it can also be from the left side) of the fish for 10s during each trial. (b) Spiking activities of all putative  
 1744 neurons in Fish B transformed to a 2D space with UMAP. Neurons in each color group have similar firing  
 1745 patterns. (c) Neurons' spatial locations in Fish B. Group 1 neurons (blue) are concentrated in the optic  
 1746 tectum, Group 2 neurons (orange) are mostly located in the hindbrain, Group 3 (gray) neurons are  
 1747 distributed across the brain. OT: optic tectum. CB: cerebellum. MO: medulla oblongata. Scale bar: 100  $\mu$ m.  
 1748 (d) Neuron spike raster plots for Fish B. Four distinct activity patterns are observed in each Fish: Group 1  
 1749 neurons (blue) have increased activity immediately after UV stimulation onset. Group 2 neurons (orange)

1750 have multiple episodes of increased activity throughout the trials. Group 3 neurons (gray) have spontaneous  
 1751 activities throughout the trials. (e) Representative traces of neurons' putative subthreshold and spiking  
 1752 activity from (d).

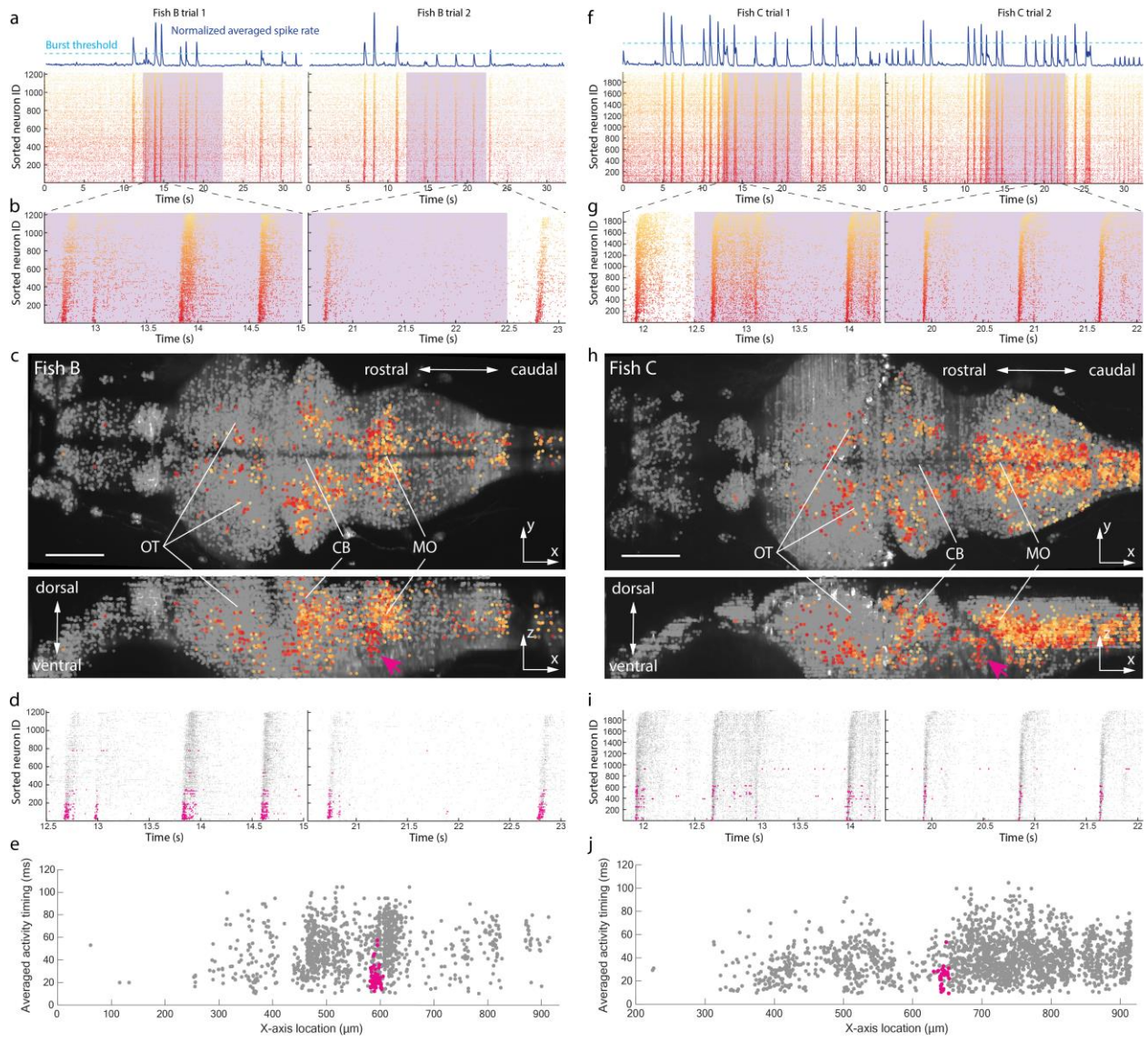
1753



1754

1755 **Figure 4. Spatial mapping of neurons' firing at different times in stimulus-evoked sequences.** (a) The  
 1756 sequential order of Fish A's Group 1 neurons' peak rate latencies in trial 1 is similar in trial 2. Neuron IDs  
 1757 are sorted based on their peak spiking rate latencies averaged across trials 1 and 2. (b) Fish A Group 1  
 1758 neurons' peak spiking rate latencies for trial 1, measured relative to UV onset, have a positive correlation  
 1759 with those of trial 2, as determined by Pearson's correlation ( $r$  and  $p$  values provided). (c) Neuron firing  
 1760 latency vs. neuron location along the y-axis (from left lateral to right lateral in the brain). During the UV  
 1761 stimulus, neurons located more laterally fired earlier than neurons located more medially. The dashed line  
 1762 represents the midline separating the left and right lateral halves of the brain. Spearman's rank correlation  
 1763 was calculated independently for the left and right halves, with  $\rho$  and  $p$  values provided. (d) Group 1 neurons'  
 1764 spatial positions color coded by their firing latency. The majority of Group 1 neurons are located on the  
 1765 lateral-left side of the optic tectum. OT: optic tectum. CB: cerebellum. MO: medulla oblongata. Scale bar:  
 1766 100  $\mu\text{m}$ . (e-h) As in (a-d), for Fish B.

1767



1768

1769 **Figure 5. Spatial mapping of the timing of activity within burst sequences, across the zebrafish brain.**

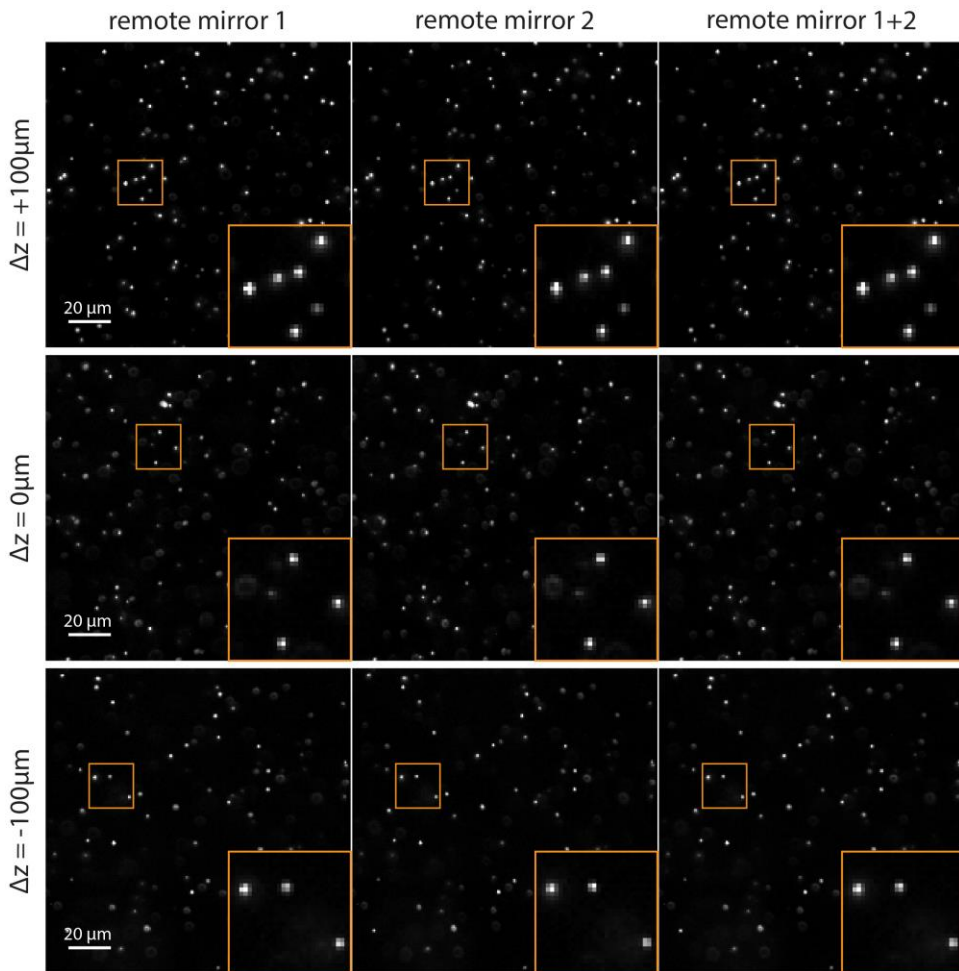
1770 (a) Raster plot showing bursting in Group 2 neurons during the light stimulation experiments in Fish B.  
 1771 These neurons correspond to the orange group in Figure 3b's UMAP plot. We define a burst as a period  
 1772 when the average spike rate, taken over an interval of 70 ms, is larger than 5 times the mean spike rate, over  
 1773 the whole trial. The start of each burst was defined as the first time point in the burst when the average  
 1774 spike rate surpassed this threshold. Neurons were sorted by their activation timing, averaged across all burst  
 1775 events. The two trials were separated by a 20 min dark session. The UV stimulus period is indicated in  
 1776 purple. (b) Magnified views of the boxed areas in (a), illustrating a consistent sequence of neural activation  
 1777 during bursts. This sequential order is color-coded from deep red (early) to light orange (late). (c) 3-D  
 1778 locations of neurons from (a), superimposed on the dorsal (top) and lateral (bottom) brain views (MIPs) of  
 1779 Fish B. The neuron firing sequence is color-coded using the same gradient of colors as in (b). The magenta

1780 arrow highlights a putative physical cluster of early firing neurons. OT: optic tectum. CB: cerebellum. MO:  
1781 medulla oblongata. Scale bar: 100  $\mu$ m. (d) The putative physical cluster of neurons highlighted by the  
1782 magenta arrow in (c) fired earlier during each burst event. (e) Group 2 neurons' x-axis locations and activity  
1783 timing averaged across all bursts in two trials were plotted as dots, with the putative physical cluster of  
1784 neurons highlighted by the magenta arrow in (c) shown in magenta, the rest of the neurons in gray. (f-j) as  
1785 in (a-e), for Fish C.

1786

1787

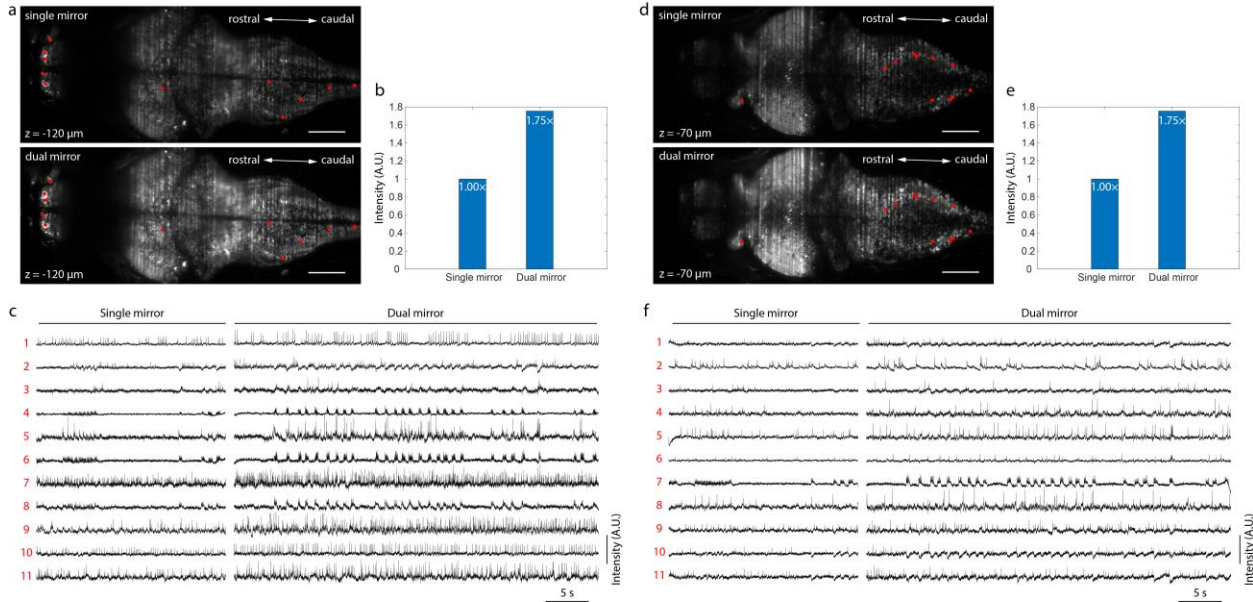
1788

1789 **SUPPLEMENTARY FIGURES**

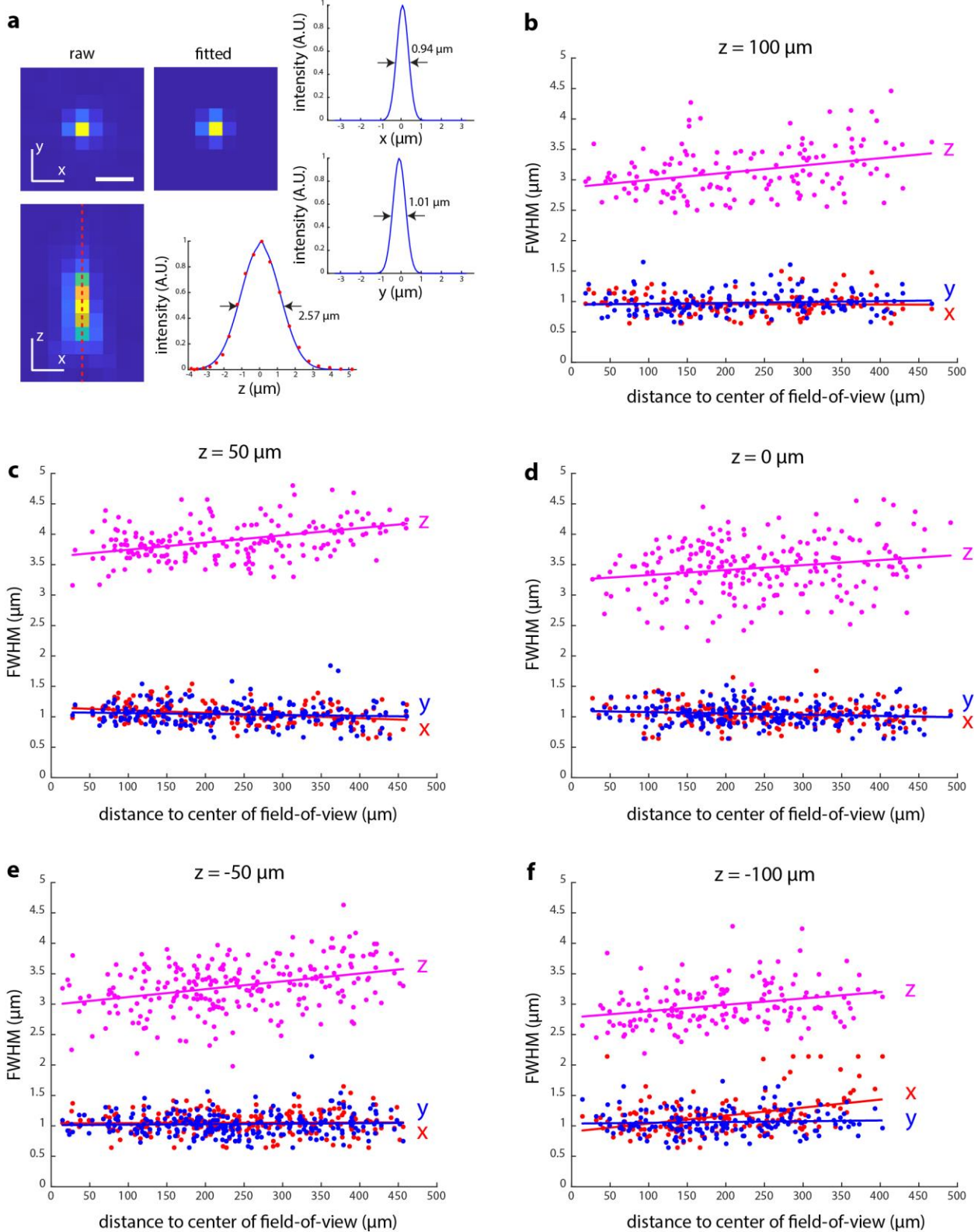
1790

1791 **Figure S1. High-precision alignment of images from two remote scanning mirrors across a 200- $\mu\text{m}$**   
1792 **axial field-of-view.** Left column, images of a fluorescent bead sample captured at three axial positions (top,  
1793  $\Delta z = +100\mu\text{m}$ , middle,  $\Delta z = 0\mu\text{m}$ , bottom,  $\Delta z = -100\mu\text{m}$ ) using remote scanning mirror 1. Middle column,  
1794 images of the fluorescent bead sample captured at the same axial positions as the left column using remote  
1795 scanning mirror 2. Right column, overlay of images of the fluorescent bead sample at the three axial  
1796 positions from both remote scanning mirrors. A magnified view of the smaller orange boxed area is shown  
1797 in the bottom right corner of each image. Image intensities were normalized for display.

1798



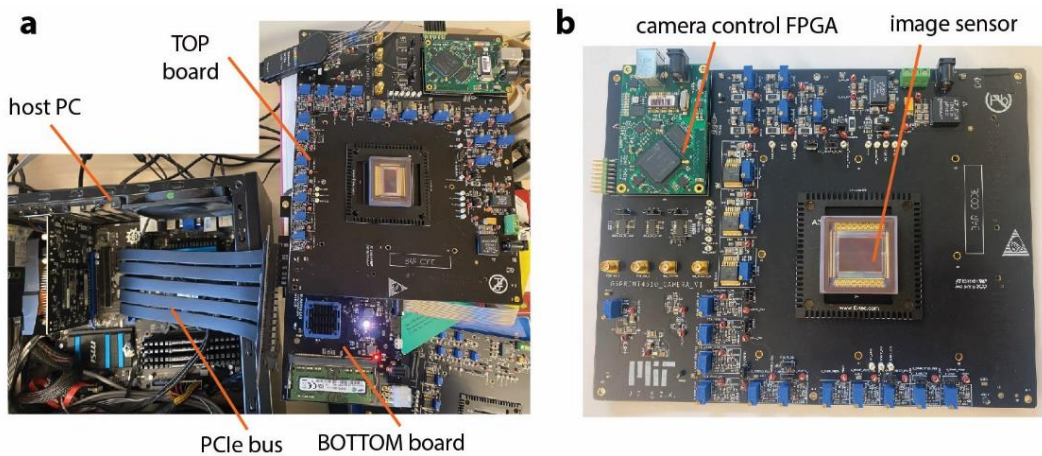
1800 **Figure S2. Dual remote scanning mirrors enhanced image intensity and signal amplitudes.** (a) Raw  
 1801 images of a randomly selected zebrafish brain plane (out of 30) acquired with single (top) and dual (bottom)  
 1802 remote scanning mirrors. Red spots mark 11 randomly selected neurons in the plane exhibiting neural  
 1803 activity. Scale bar: 100  $\mu$ m. (b) The use of dual remote scanning mirrors increased the image intensity of  
 1804 this plane by 75%. (c) Intensity traces of the same neurons (highlighted by red spots in (a)) were compared  
 1805 between using single and dual remote scanning mirrors. (d-f) The same analysis as in (a-c) was performed  
 1806 for another randomly selected plane of the same zebrafish brain.



1808 **Figure S3. Characterization of system point spread functions (PSFs) over the entire imaging field-of-**  
 1809 **view. (a)** Measuring the full-width-at-half-maximum (FWHM) of a PSF. On the left, the raw xy and xz

1810 sections that intersect the brightest voxel of the 3D PSF are shown. The xy section is fitted by a 2D Gaussian  
1811 function. The fitted image is displayed in indicated panel. On the right, x and y cross-section profiles of the  
1812 fitted Gaussian function are shown, and FWHM values are marked. The axial (z) FWHM is determined by  
1813 fitting the PSF's axial line profile with a double Gaussian function. **(b-f)** Visualization of the FWHM  
1814 measurements of PSFs at varying radial positions and depths.

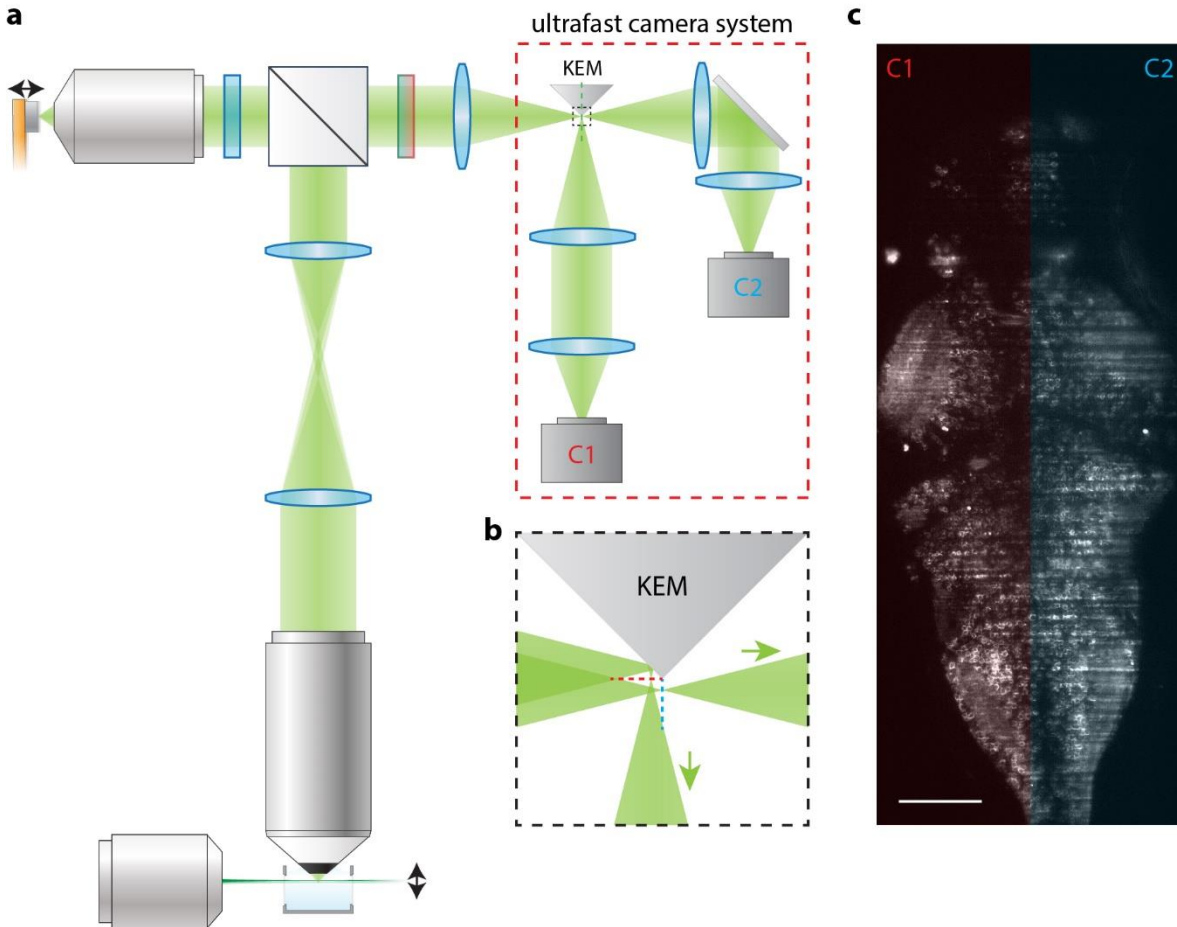
1815



1816

1817 **Figure S4. Customized high-speed camera system. (a)** The camera system is a two board stack design.  
1818 The TOP board **(b)** hosts the image sensor and uses an FPGA (Xilinx Spartan 6, Opal kelly XEM6010) to  
1819 handle camera control and trigger synchronization. The BOTTOM board uses an FPGA (Xilinx Kintex-7)  
1820 with external DDR RAM to buffer and transfer high-bandwidth data (2.6GBps) to the host computer  
1821 through a PCIe bus.

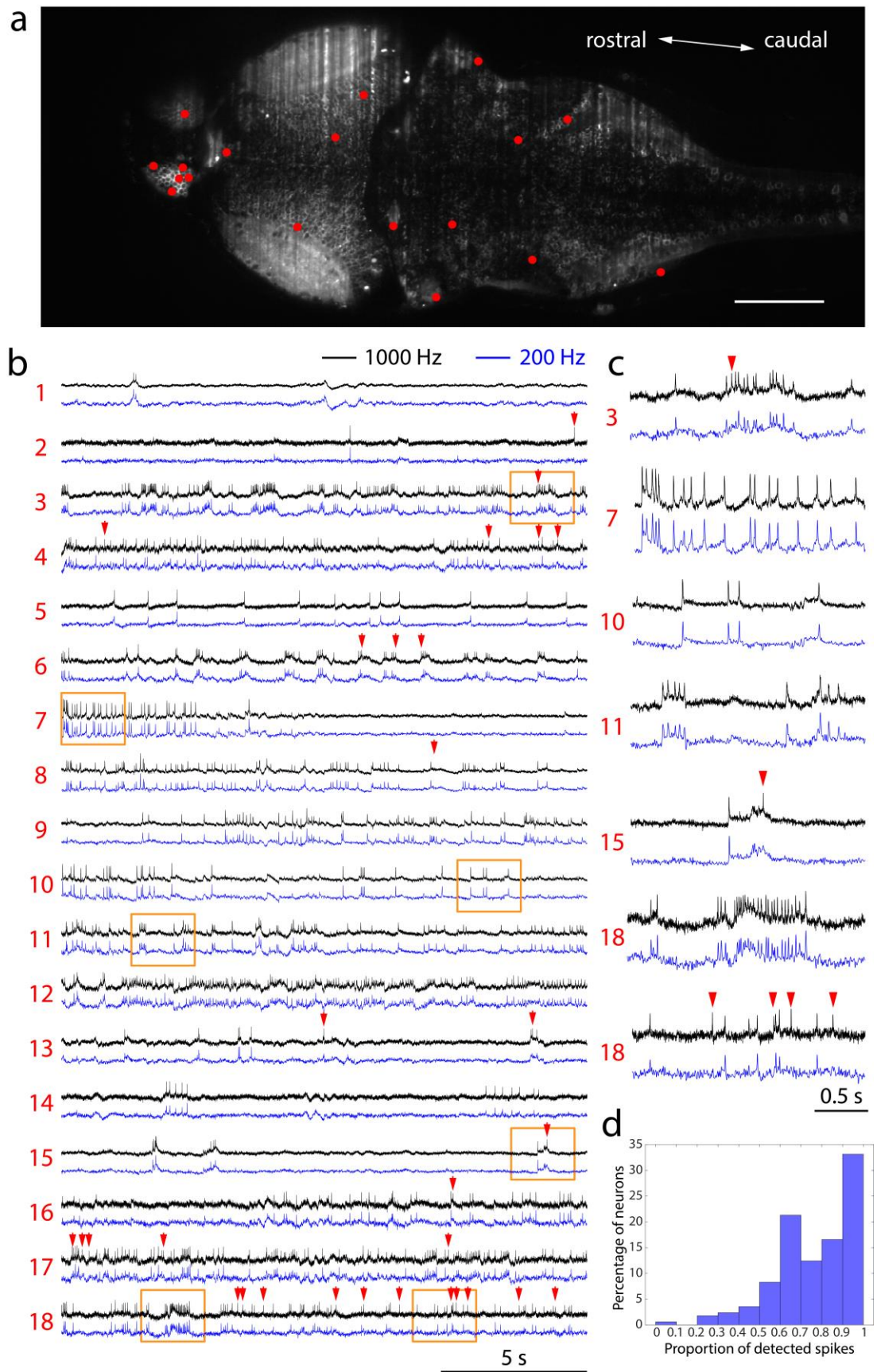
1822



1823

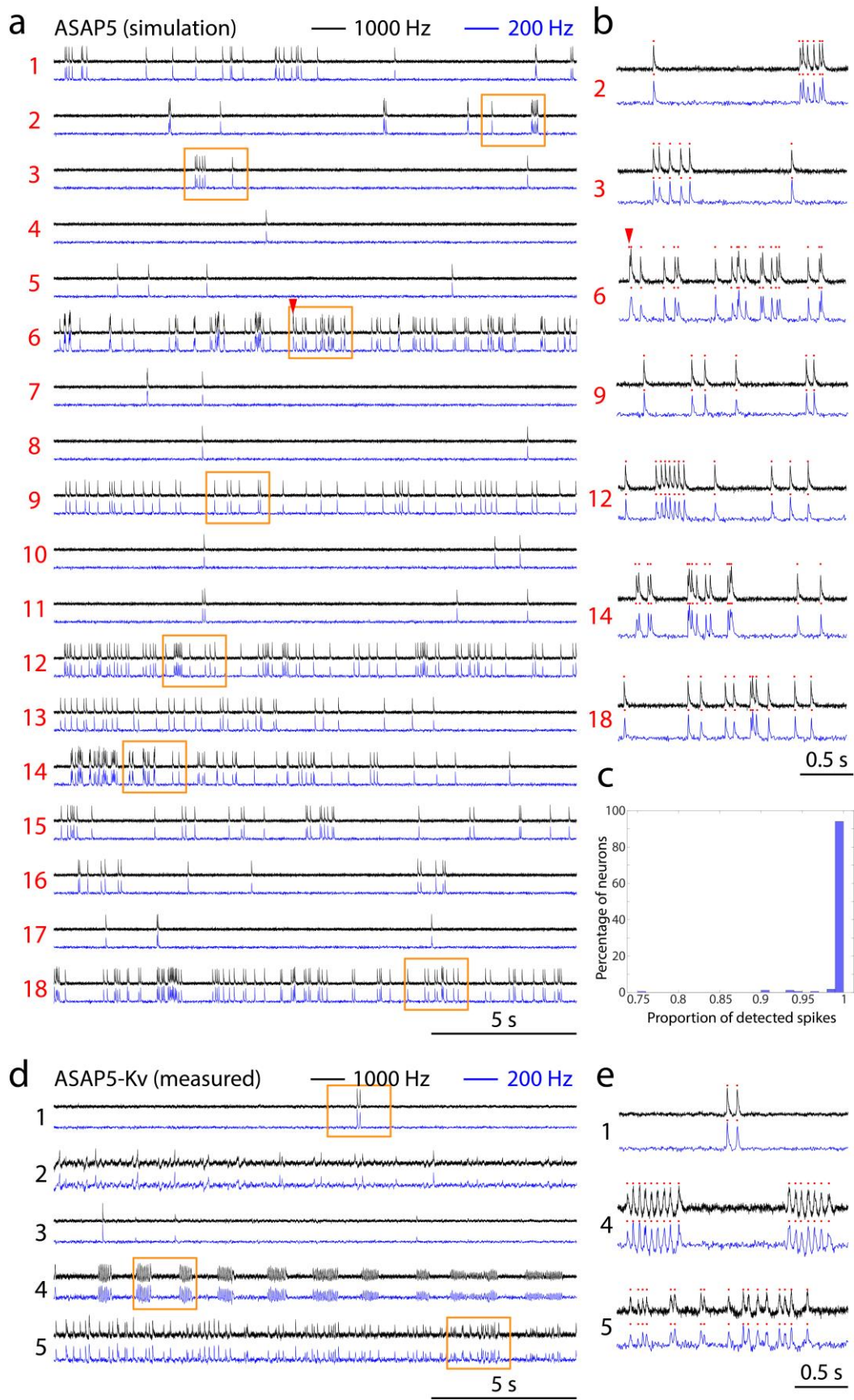
1824 **Figure S5. Overview of the ultrafast camera system.** (a) Images from the high-speed light-sheet  
 1825 microscope are recorded by an ultrafast camera system (red dashed line box) consisting of an image splitter  
 1826 and two ultrafast cameras. Focused images from the microscope are divided by a knife-edge mirror (KEM)  
 1827 into two halves. These split images are then relayed through two identical lens pairs to the ultrafast cameras  
 1828 (C1 and C2) for recording. (b) Enlarged view of the areas in the black dashed box in (a). The KEM splits  
 1829 an image by deflecting only its upper half to a different light path. (c) Stitching raw images from cameras  
 1830 C1 and C2 produces a full section image of the zebrafish brain. Scale bar: 100  $\mu$ m.

1831



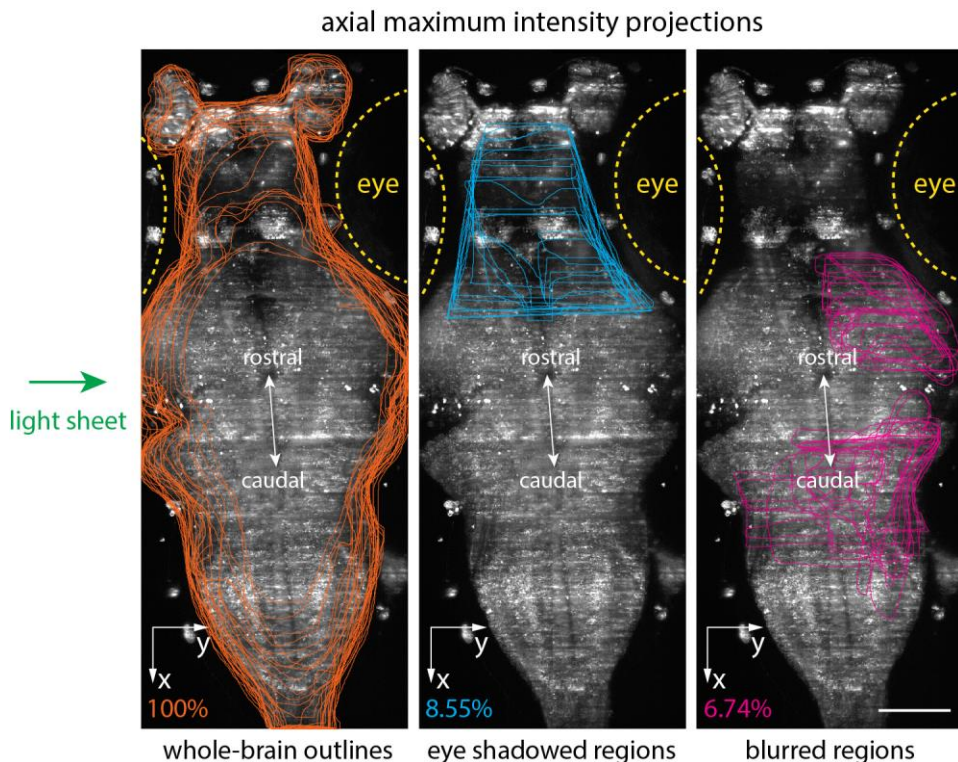
1833 **Figure S6. Quantification of spike detection rate using the Positron2-Kv indicator at a 200-Hz**  
1834 **imaging rate.** (a) Raw image of an imaged zebrafish brain plane. Red spots mark randomly selected  
1835 neurons (out of a total of 201 neurons that showed spikes and were not affected by moving stripe artifacts)  
1836 whose traces are shown below in (b). Scale bar: 100  $\mu\text{m}$ . (b) Neural traces extracted from the original  
1837 recording at a 1-kHz imaging rate with a 40- $\mu\text{s}$  exposure time (black traces) are compared with the neural  
1838 traces extracted from a 200-Hz video downsampled from the 1-kHz recording. Red arrows indicate  
1839 locations where spikes were missed in the 200-Hz traces. Orange boxes highlight regions magnified in (c).  
1840 (c) Magnified views of the orange-boxed regions in (b). (d) Histogram showing the percentage of neurons  
1841 categorized by their spike detection rates (defined as the number of detected spikes divided by the number  
1842 of all spikes) in the 200-Hz neural traces.

1843



1845  
 1846 **Figure S7. Quantification of spike detection rate using the ASAP5-Kv indicator at a 200-Hz**  
 1847 **imaging rate.** (a) Simulated neural traces at a 1-kHz imaging rate (black traces) are compared with the  
 1848 neural traces down sampled to a 200-Hz imaging rate. The red arrow indicates a location where a spike  
 1849 was missed in the 200-Hz traces. Orange boxes highlight regions magnified in (b). All traces were flipped  
 1850 vertically and normalized by their maximum amplitude for display. (b) Magnified views of the orange-  
 1851 boxed regions in (a). Red dots indicate detected spikes. (c) Histogram showing the percentage of neurons  
 1852 categorized by their spike detection rates in the 200-Hz neural traces, based on simulation results. (d)  
 1853 Measured ASAP5-Kv neural traces in larval zebrafish at a 1-kHz imaging rate (black traces) are  
 1854 compared with the neural traces down sampled to a 200-Hz imaging rate. All traces were flipped  
 1855 vertically and normalized by their maximum amplitude for display. Orange boxed areas are shown in  
 1856 magnified views in (e). Red dots in (e) indicate detected spikes.

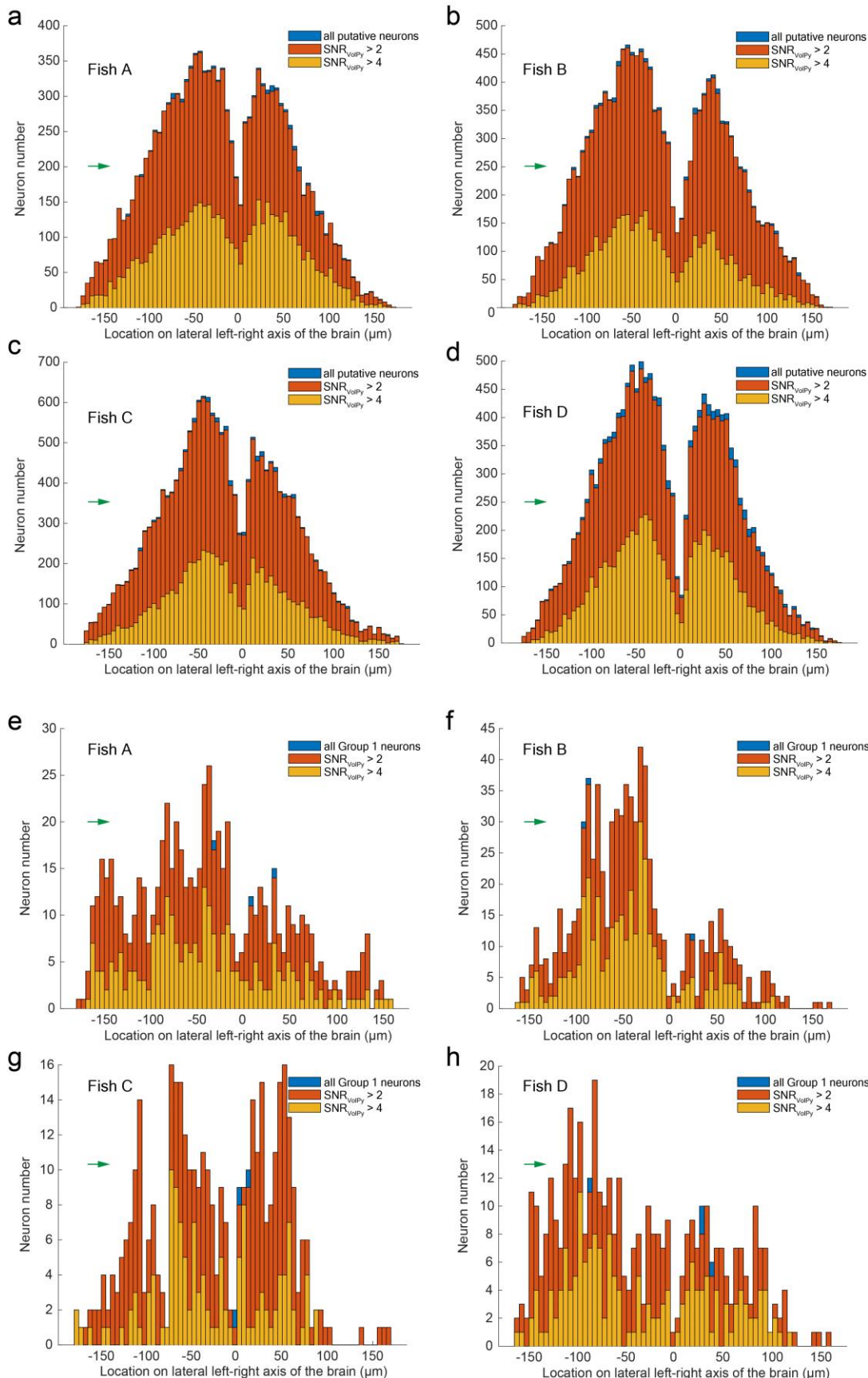
1857



1858  
 1859 **Figure S8. Quantifying the eye shadowed regions and the blurred regions as percentages of the**  
 1860 **imaged whole brain.** Contours of the whole brain (orange), the regions that were shadowed by eyes (cyan),  
 1861 and the blurred regions where single cells cannot be resolved (magenta), were drawn on individual z-plane  
 1862 images (30 planes in total, 5.86  $\mu\text{m}$  z step size) of the whole zebrafish brain. To draw these contours, we  
 1863 visually examined the raw image of each z-plane and drew the 2-D contours of the whole brain (orange),

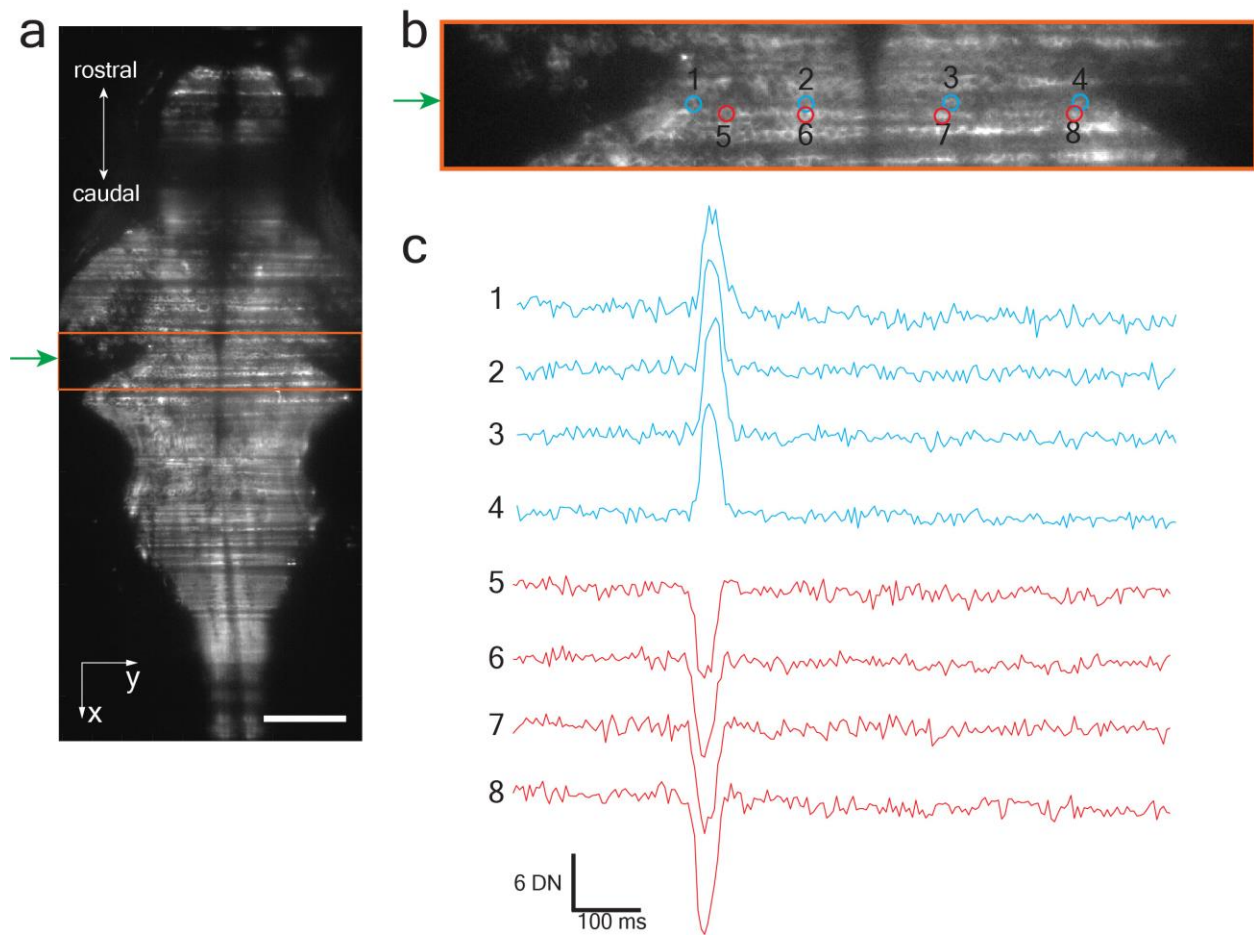
1864 the dark region shadowed by the fish's eye (cyan), and the regions where we could not visually distinguish  
1865 single cells (magenta). These 2-D contours were projected along the z axis and displayed on the axial  
1866 maximum intensity projections (MIPs) of the imaged brain. Yellow dashed lines indicate the fish's eyes.  
1867 Within the imaged brain (left, orange contours), 8.55% (middle, cyan contours) of the full brain region was  
1868 shadowed by fish's eyes, 6.74% (right, magenta contours) was too blurred to visually resolve single cells.  
1869 The light sheet (green arrow) was illuminated towards the left side of the brain. Scale bar: 100  $\mu$ m.

1870



1872 **Figure S9. Histograms show the distribution of all putative neurons and all Group 1 neurons along**  
1873 **the lateral left-right axis of the brains of Fish A-D.** (a-d) For each of the fish A-D, three histograms were  
1874 plotted: one for all putative neurons, and two for putative neurons that passed two SNR<sub>VolPy</sub> thresholds  
1875 (SNR<sub>VolPy</sub>>2, SNR<sub>VolPy</sub>>4). Green arrows indicate the direction of light-sheet illumination. Location 0 on  
1876 the horizontal axis in these histograms represents the midline of the brain, a boundary between the left and  
1877 right hemispheres where the density of GEVI-labeled neurons is lower. (e-h) The same histograms for all  
1878 Group 1 neurons of Fish A-D.

1879



1880

1881 **Figure S10. Representative pulse-like artifacts on the temporal traces of ROIs affected by the stripe**  
1882 **artifacts cast by small moving objects in light-sheet imaging.** (a) Raw image frame from a video of a z-

1883 plane of the larval zebrafish brain. The light sheet is illuminated from the left side of the brain (green arrow).

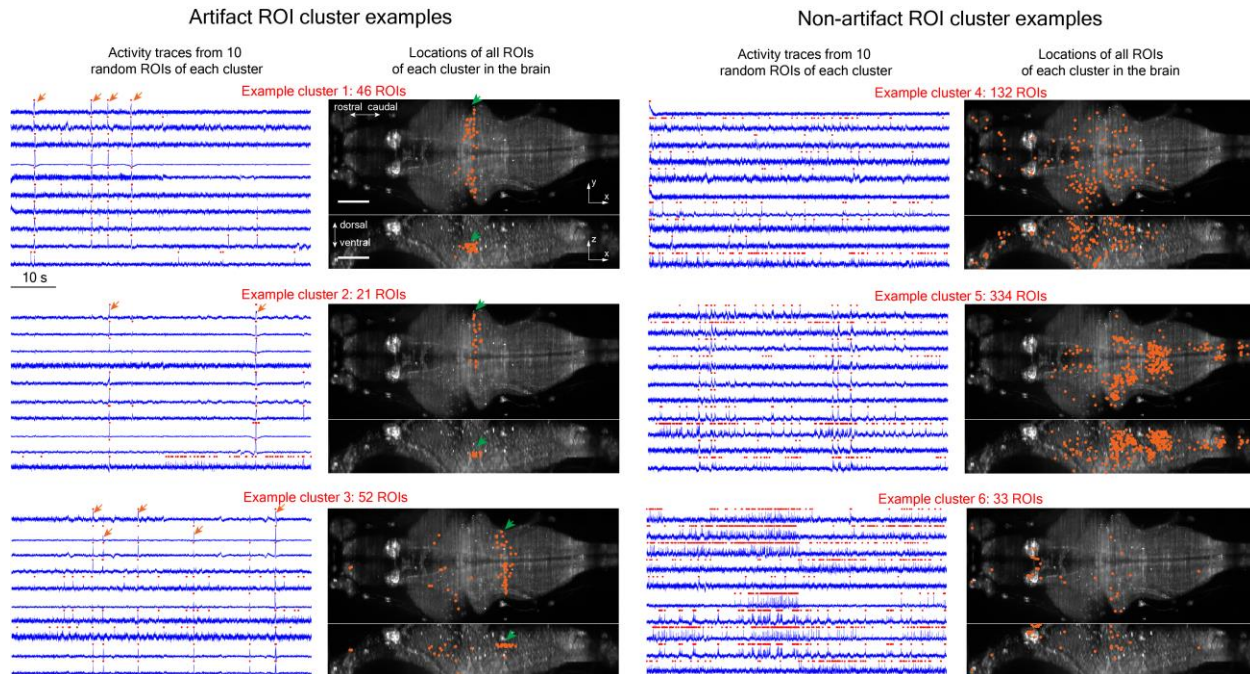
1884 Scale bar: 100  $\mu$ m. (b) Zoom-in view of the orange boxed region in (a). The raw temporal traces from

1885 arbitrarily annotated circular ROIs (cyan and red) are extracted. ROIs with the same color lay on the same

1886 artifact stripe. (c) Extracted raw temporal traces from the ROIs in (b). The traces from the cyan ROIs

1887 exhibited a synchronous positive-going pulse-like artifact, while the traces from the red ROIs exhibited a  
1888 synchronous negative-going pulse-like artifact. These pulse-like artifacts had a duration width of ~50 ms,  
1889 much longer than that of an action potential spike. DN: digital number, measurement of the pixel intensity.  
1890 Also see Supplementary Video 1.

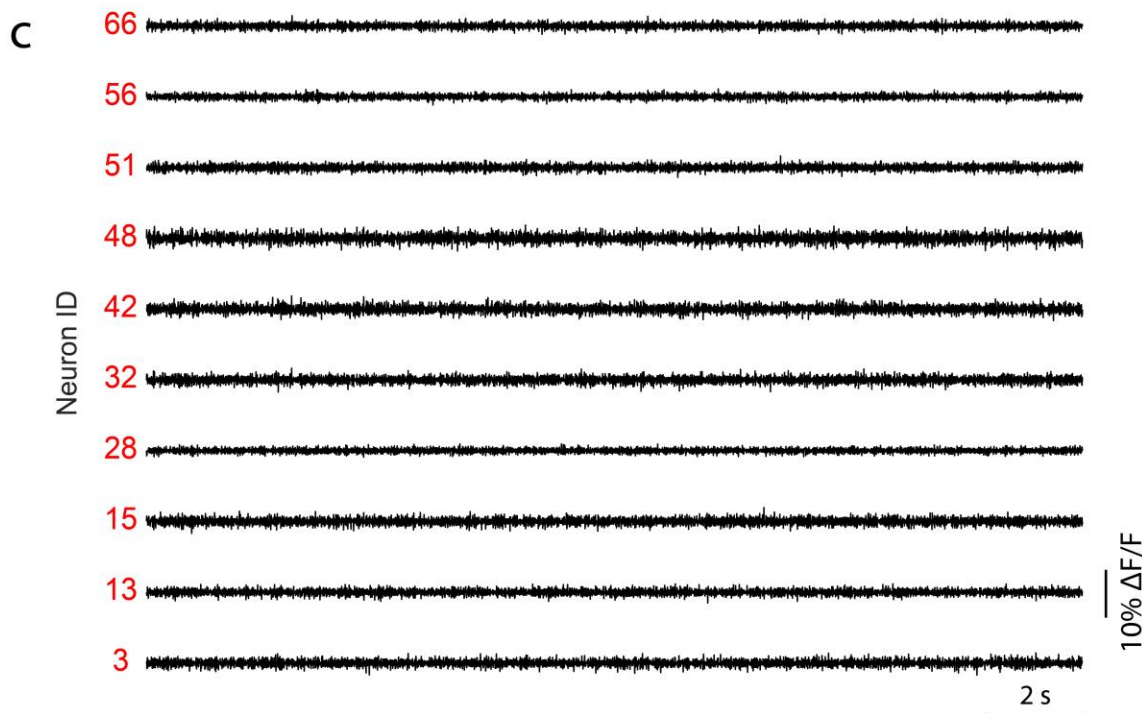
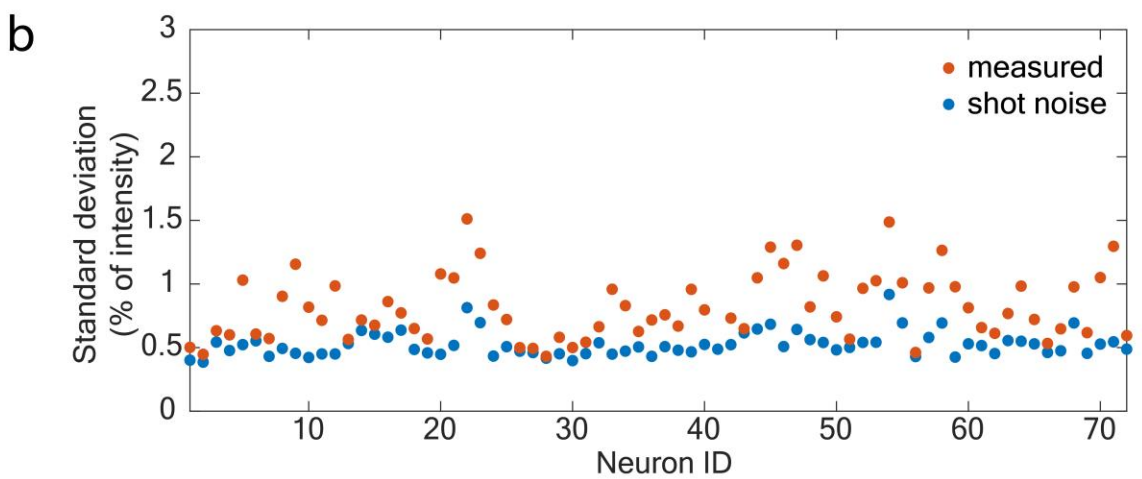
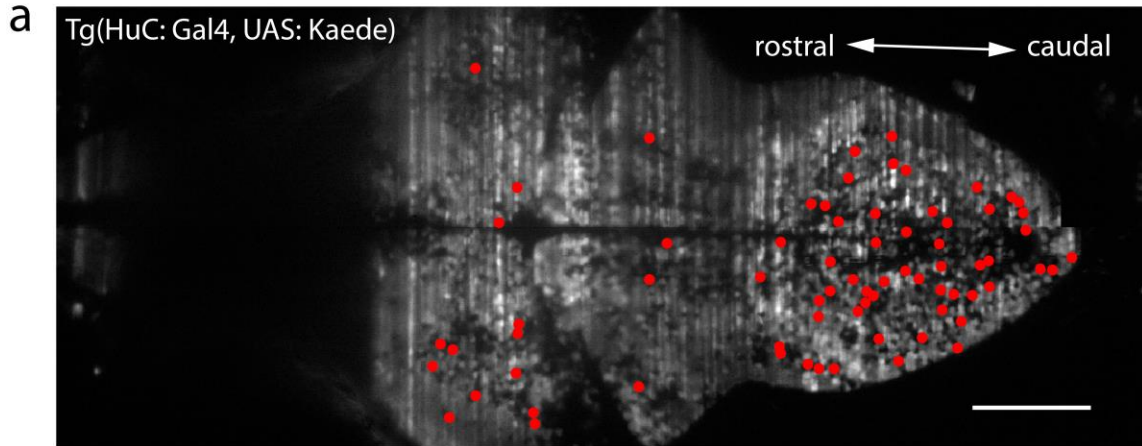
1891



1892

1893 **Figure S11. Temporal traces and spatial distributions of randomly selected ROI clusters from Fish**  
1894 **B that were contaminated (left column) and not contaminated (right column) by moving stripe**  
1895 **artifacts.** In each panel, the left side displays the temporal traces of 10 randomly selected ROIs within the  
1896 cluster, plotted in blue. Detected spikes are marked as red dots on the traces. Orange arrows highlight  
1897 putative synchronous pulse-like artifacts. On the right side of each panel, the spatial locations of the ROIs  
1898 (orange dots) within the cluster are overlaid on the axial and lateral maximum intensity projections of the  
1899 zebrafish brain. Green arrows indicate ROI clusters with spatial distributions resembling the shape of  
1900 moving stripe artifacts along the illumination direction. Clusters exhibiting both synchronous pulse-like  
1901 artifacts in their temporal traces and spatial distribution patterns similar to the stripe artifacts (example  
1902 cluster 1-3 in the left column) were excluded from further analysis. Scale bar: 100  $\mu$ m.

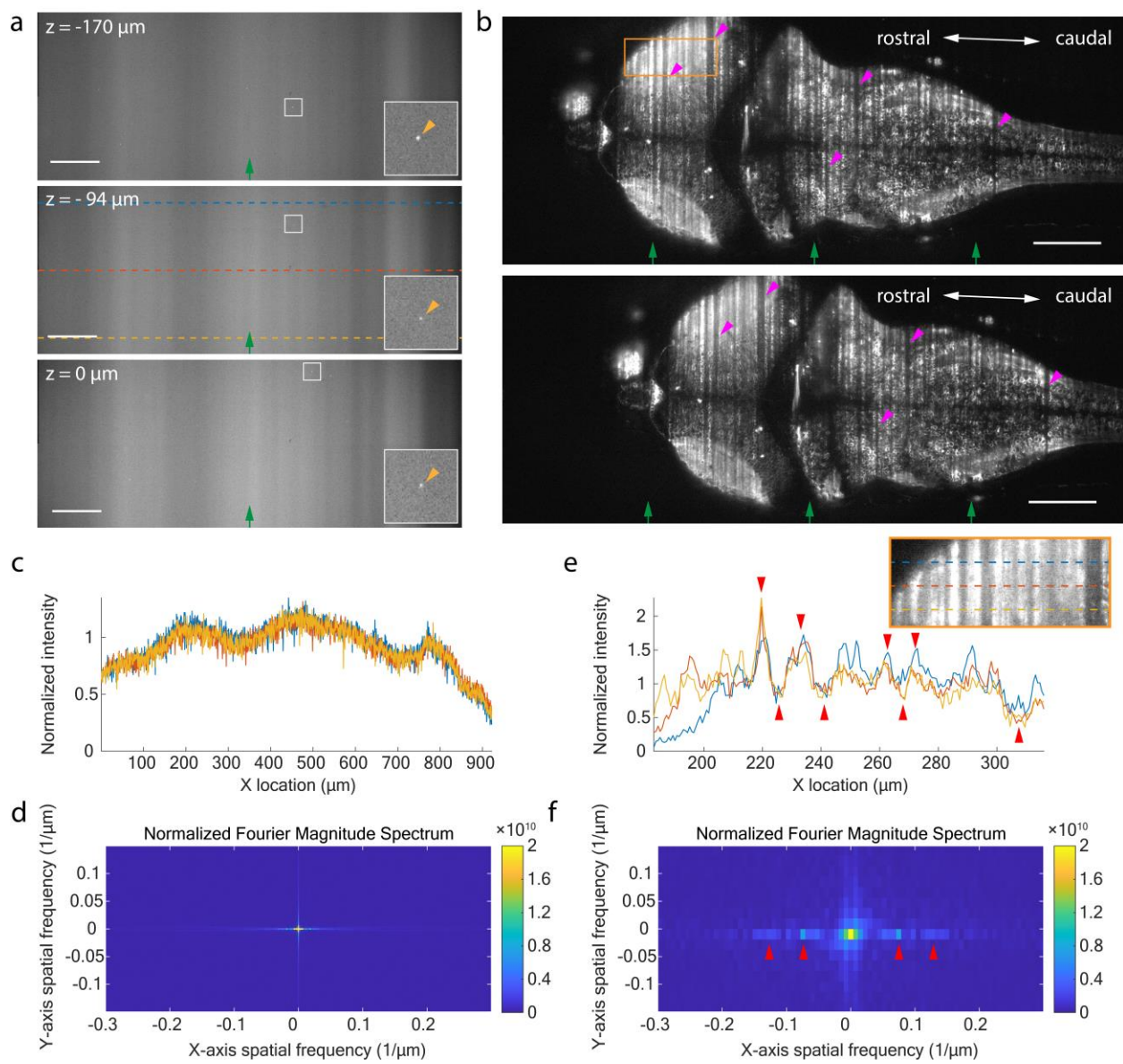
1903



1905 **Figure S12. Quantification of the baseline noise using pan-neuronal Kaede fish.** (a) A randomly  
 1906 selected single-plane image (out of 30) of the Kaede fish brain was analyzed. Neurons (red spots) indicated  
 1907 were randomly selected across the areas in the plane that did not visually overlap with any moving stripe  
 1908 in the raw video, for signal trace analysis. Scale bar: 100  $\mu\text{m}$ . (b) To quantify the baseline noise, we  
 1909 calculated the standard deviation of the signal traces of the neurons marked in (a) and plotted the standard  
 1910 deviations (orange dots) as percentages relative to the baseline intensity. The theoretical shot noise of each  
 1911 signal trace was also plotted (blue dots). (c) Signal traces of 10 neurons randomly selected from the 72  
 1912 analyzed neurons.

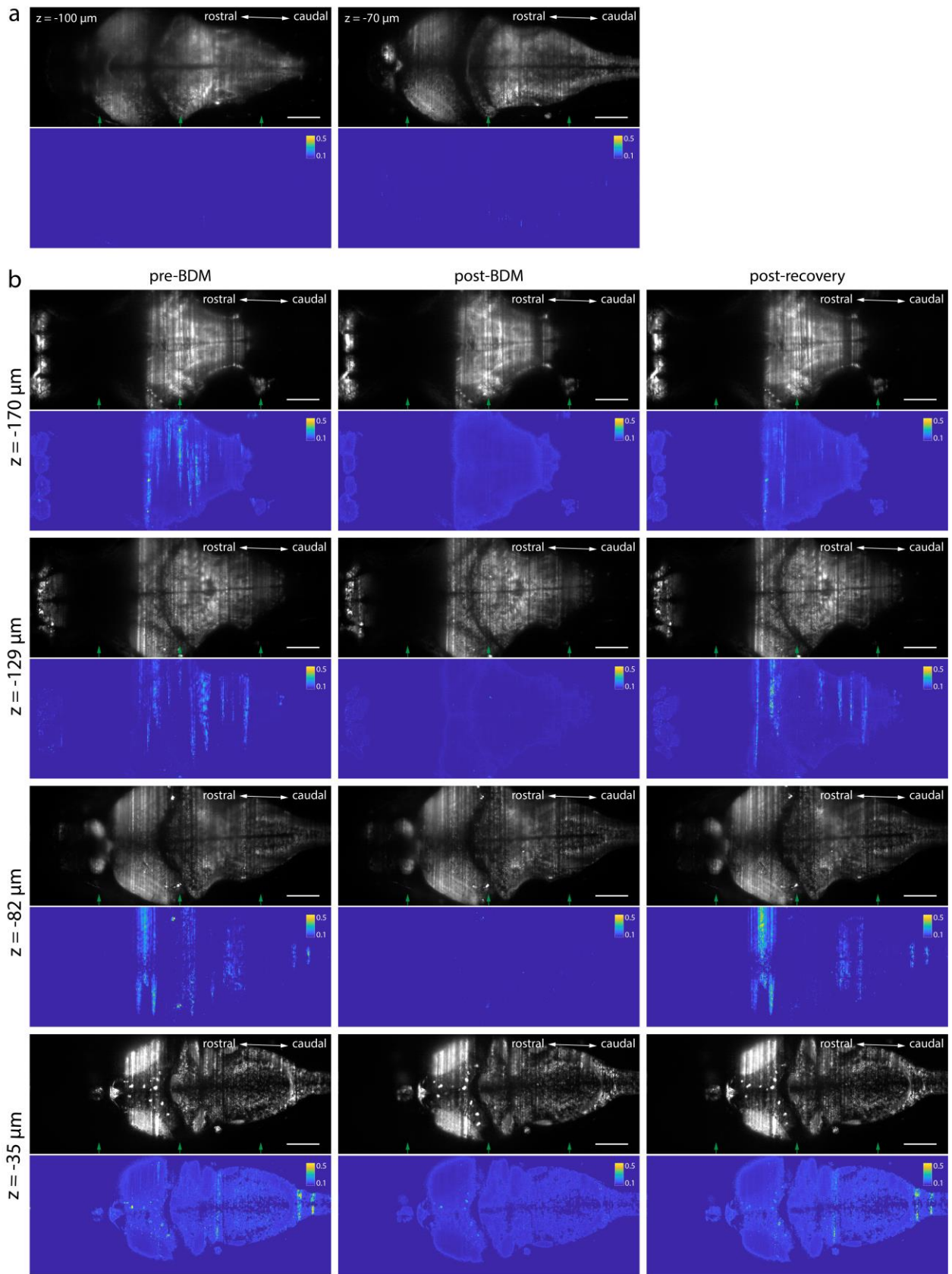
1913

1914



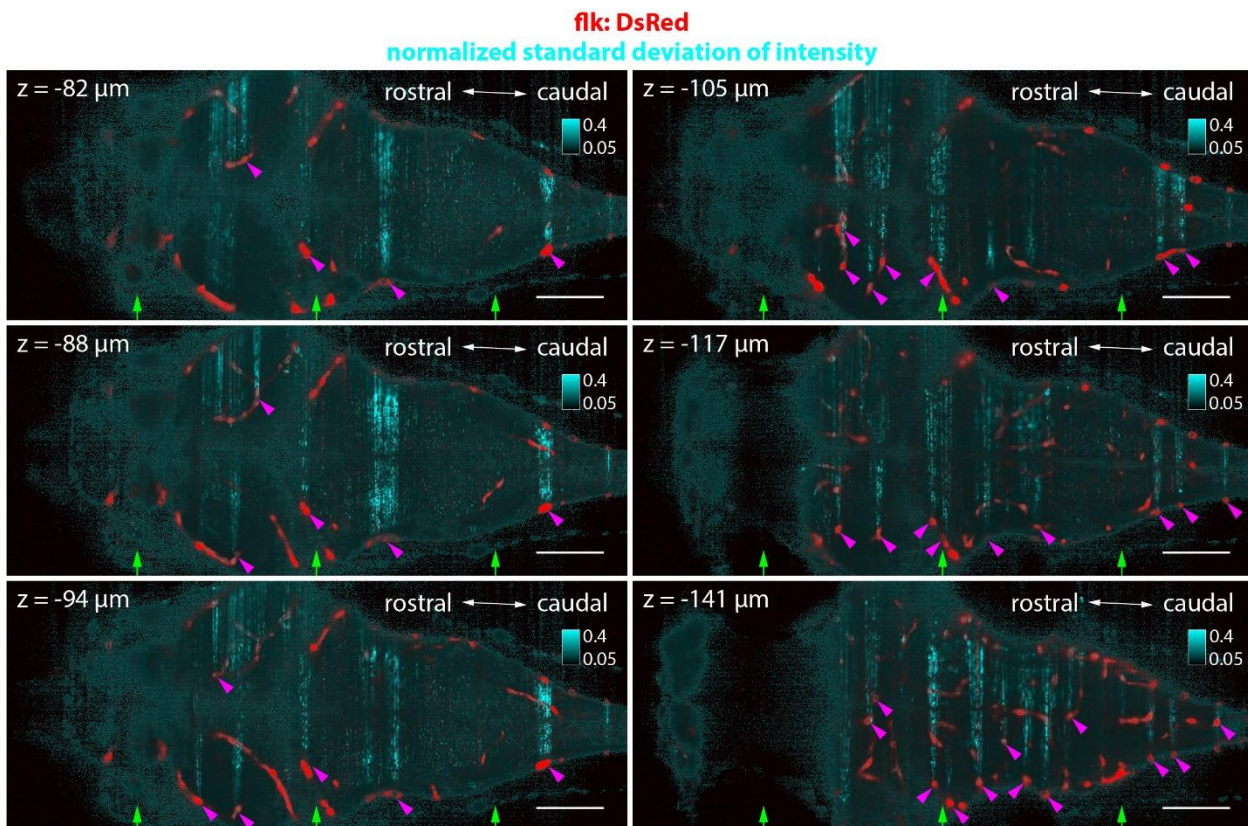
1915

1916 **Figure S13. Control experiments indicated that the stripe artifacts did not come from the setup and**  
1917 **were associated with the animal.** (a) Raw light-sheet images of a JF525-dye containing agarose sample.  
1918 Single-plane images at different depths (z) are shown. Green arrows denote the direction of light sheet  
1919 illumination. The agarose also contained sparse 200-nm diameter fluorescent beads, whose focused, sharp  
1920 images (orange arrows) can be seen in the enlarged boxes (they are too small to be seen easily, in the  
1921 zoomed-out images). The intensity profiles along three lines (blue, red, and orange dashed lines) in the  
1922 central image were plotted in (c). Scale bar: 100  $\mu\text{m}$ . (b) Comparison of raw single-plane images of a  
1923 zebrafish brain as the fish was moved along the x-axis (horizontal axis in these images). Stationary stripe  
1924 artifacts (magenta arrows) remained fixed in position with respect to the brain, but not with respect to the  
1925 microscope, suggesting these stationary stripes were associated with the fish itself. Green arrows denote  
1926 the direction of light sheet illumination. The orange-boxed area in the top image was used for profile plot  
1927 and Fourier analysis in (e-f). The orange-boxed area avoids areas with fine neuron soma boundaries, which  
1928 possess high spatial frequencies that can potentially complicate the Fourier analysis of stripe artifacts. Scale  
1929 bar: 100  $\mu\text{m}$ . (c) Intensity profiles along three lines (blue, red, and orange) in the central image of panel (a)  
1930 were plotted, illustrating the variation of intensity along the x-axis in the agarose image. These profiles  
1931 were normalized by their mean values. (d) Magnitude spectrum of the two-dimensional Fourier transform  
1932 of the central agarose image shown in panel (a), normalized by its mean value. (e) Intensity profiles along  
1933 three lines (blue, red, and orange dashed lines) within the orange-boxed area (zoomed in at the top right  
1934 corner) of the top image in panel (b). These profiles were normalized by their mean values. Red arrows  
1935 show the locations of bright and dark stripes. (f) Magnitude spectrum of the two-dimensional Fourier  
1936 transform of the orange-boxed area in panel (b), normalized by its mean value. Red arrows highlight high  
1937 spatial frequency components corresponding to stripe artifacts.



1939 **Figure S14. Imaging of fixed fish and BDM-treated fish suggested that moving stripe artifacts were**  
 1940 **dependent on the animal, presumably on blood flow.** (a) Fixed fish showed no moving stripe artifacts in  
 1941 raw videos. The top panel displays two randomly selected planes of a fixed brain, with green arrows  
 1942 indicating the direction of light-sheet illumination. Below each single-plane image, the corresponding  
 1943 normalized temporal standard deviation map (NTSDM, see Methods for more details) is shown to visualize  
 1944 any moving stripes. No bright stripe was seen on the maps. Scale bar: 100  $\mu\text{m}$ . (b) BDM treatment removed  
 1945 moving stripes in the live zebrafish brain. Each row presents the raw images of a randomly selected plane  
 1946 (out of 30) of a zebrafish brain and their corresponding normalized temporal standard deviation maps  
 1947 (NTSDM) before the BDM-treatment (left), after the BDM-treatment (middle), and post recovery (right).  
 1948 A total of four planes of the same zebrafish brain are shown. Moving stripe patterns that were visible before  
 1949 BDM treatment (left column) disappeared after the BDM treatment (middle column). After the fish  
 1950 recovered in fresh water, the moving stripe patterns appeared again (right column). Scale bar: 100  $\mu\text{m}$ .

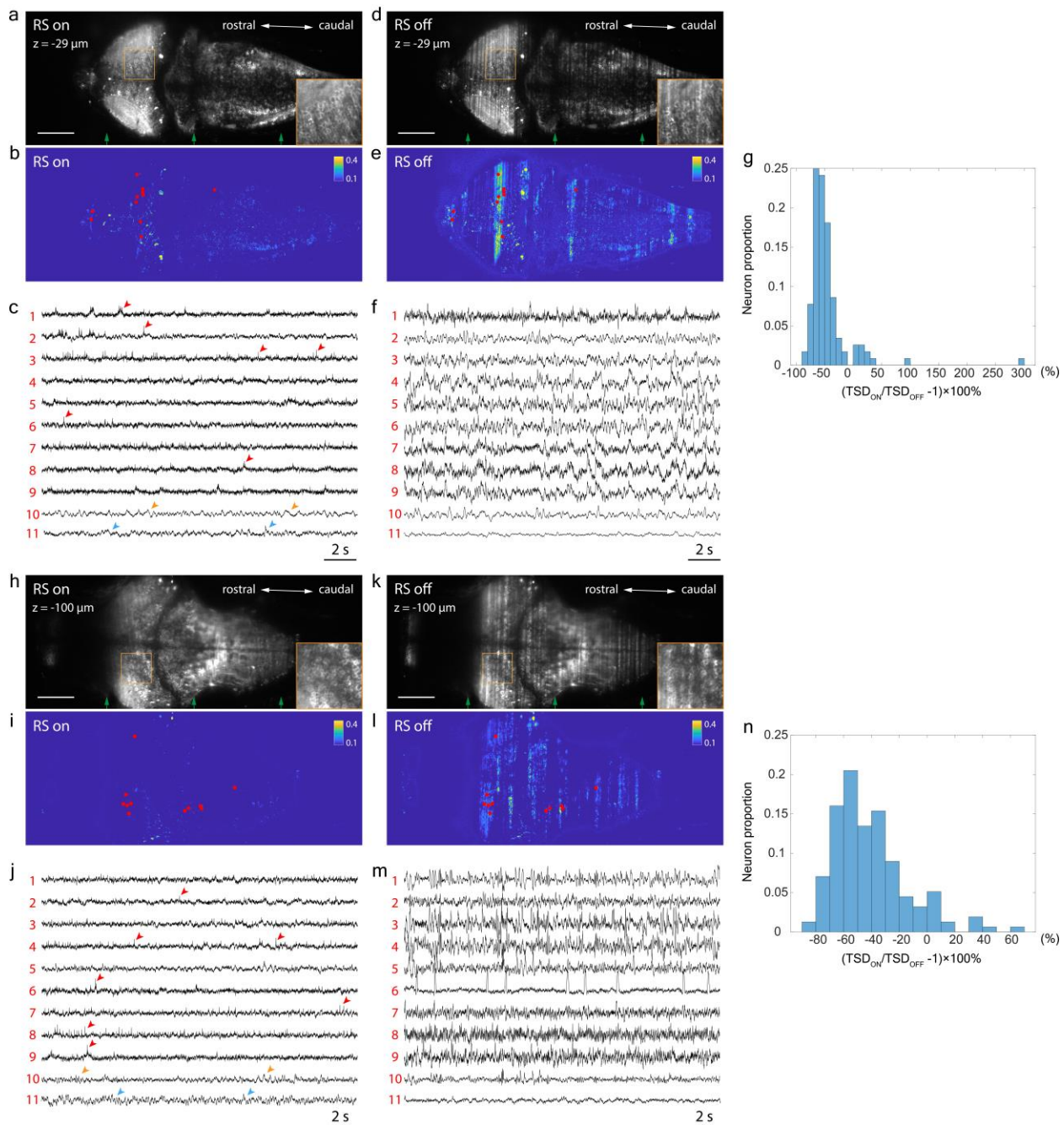
1951



1952 **Figure S15. The spatial correspondence between the blood vessels and the moving stripes suggests**  
 1953 **that the moving stripe artifacts were caused by blood flow.** This figure shows six randomly selected  
 1954 planes (out of 30) of a zebrafish brain that expressed both pan-neuronal Positron2-Kv indicator and a red

1956 vascular marker (flk:DsRed). In each plane, blood vessels (red) were overlaid with the map of moving  
 1957 stripes (cyan), which were represented by the normalized temporal standard deviation map (NTSDM, see  
 1958 **Methods**) of the fluorescence intensity in the GEVI channel. These overlaid images show a consistent  
 1959 spatial relationship, with each moving stripe originating near a corresponding blood vessel (magenta  
 1960 arrows). Green arrows denote the direction of light-sheet illumination. Scale bar: 100  $\mu$ m.

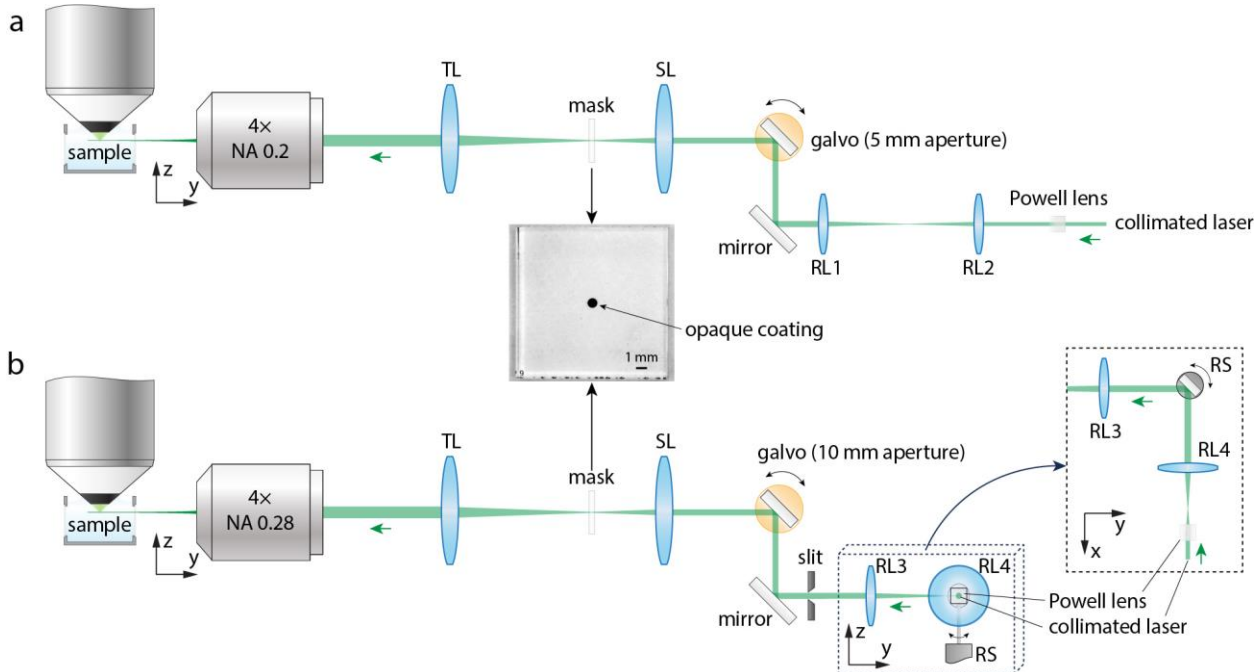
1961



1962

1963 **Figure S16. Removing stripe artifacts using a resonant mirror scanner.** (a) Raw image of a randomly  
1964 selected plane (out of 20) of a zebrafish brain expressing pan-neuronal Positron2-Kv indicator, with  
1965 resonant scanner scanning (RS on). Green arrows indicate the direction of light-sheet illumination. A  
1966 magnified view of the orange boxed region is shown in the bottom right corner. Scale bar: 100  $\mu$ m. (b) The  
1967 normalized temporal standard deviation map (NTSDM) of the brain plane shown in (a). Red spots indicate  
1968 representative neurons whose traces are shown in (c,f) for comparison between conditions when the  
1969 resonant scanner was on vs. off. (c) Intensity traces of the neurons labeled with red spots in (b). Three kinds  
1970 of representative traces are shown. Traces 1-9: the resonant scanner scanning (RS on) reduced temporal  
1971 artifacts in the traces of >90% moving-stripe-affected neurons. Red arrows indicate spikes that became  
1972 detectable after stripe artifact removal. Trace 10: for less than 10% of the moving stripe-affected neurons,  
1973 resonant scanner scanning did not efficiently remove the temporal artifacts in their traces (orange arrows),  
1974 probably due to the small pivoting angle (32.5 degrees) limited by the numerical aperture (NA=0.28) of the  
1975 illumination objective lens. Trace 11: a small subset of neurons (<1% of all imaged neurons) that did not  
1976 exhibit moving-stripe-induced artifacts in their traces when the resonant scanner was off showed temporal  
1977 artifacts (blue arrows) in their traces when the resonant scanner was active. (d-f) Results from the same  
1978 plane as in (a-c), without resonant scanner scanning (RS off). (g) Histogram displaying the distribution of  
1979 temporal standard deviation (TSD) differences in the traces of neurons with the resonant scanner on ( $TSD_{ON}$ )  
1980 versus off ( $TSD_{OFF}$ ). Only the neurons within the plane in (a-f) and affected by moving stripe artifacts when  
1981 the scanner was off were included in this analysis. (h-n) Results of the same analysis and comparison as in  
1982 (a-g), but for a different randomly selected plane of the same zebrafish brain.

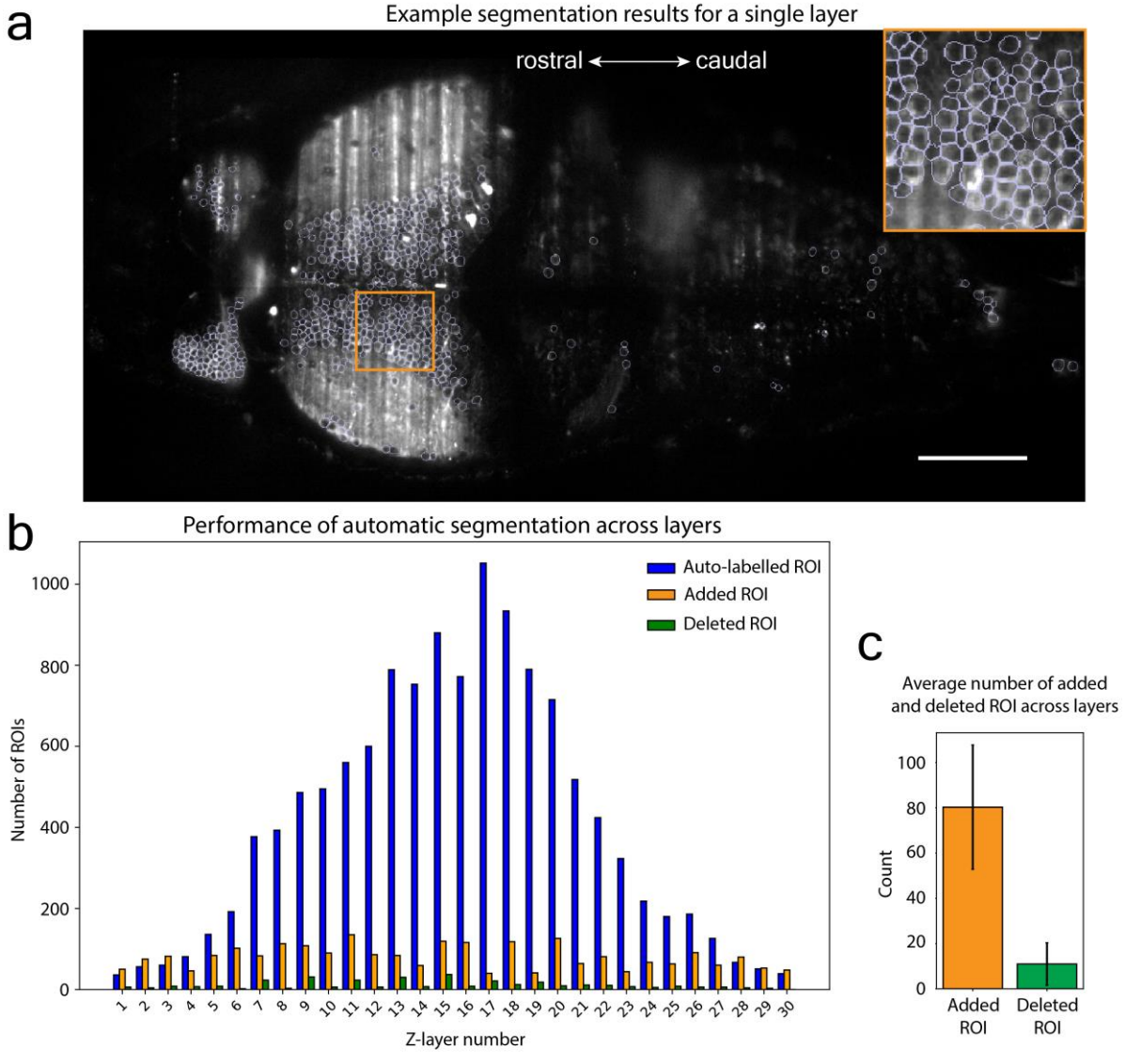
1983



1984

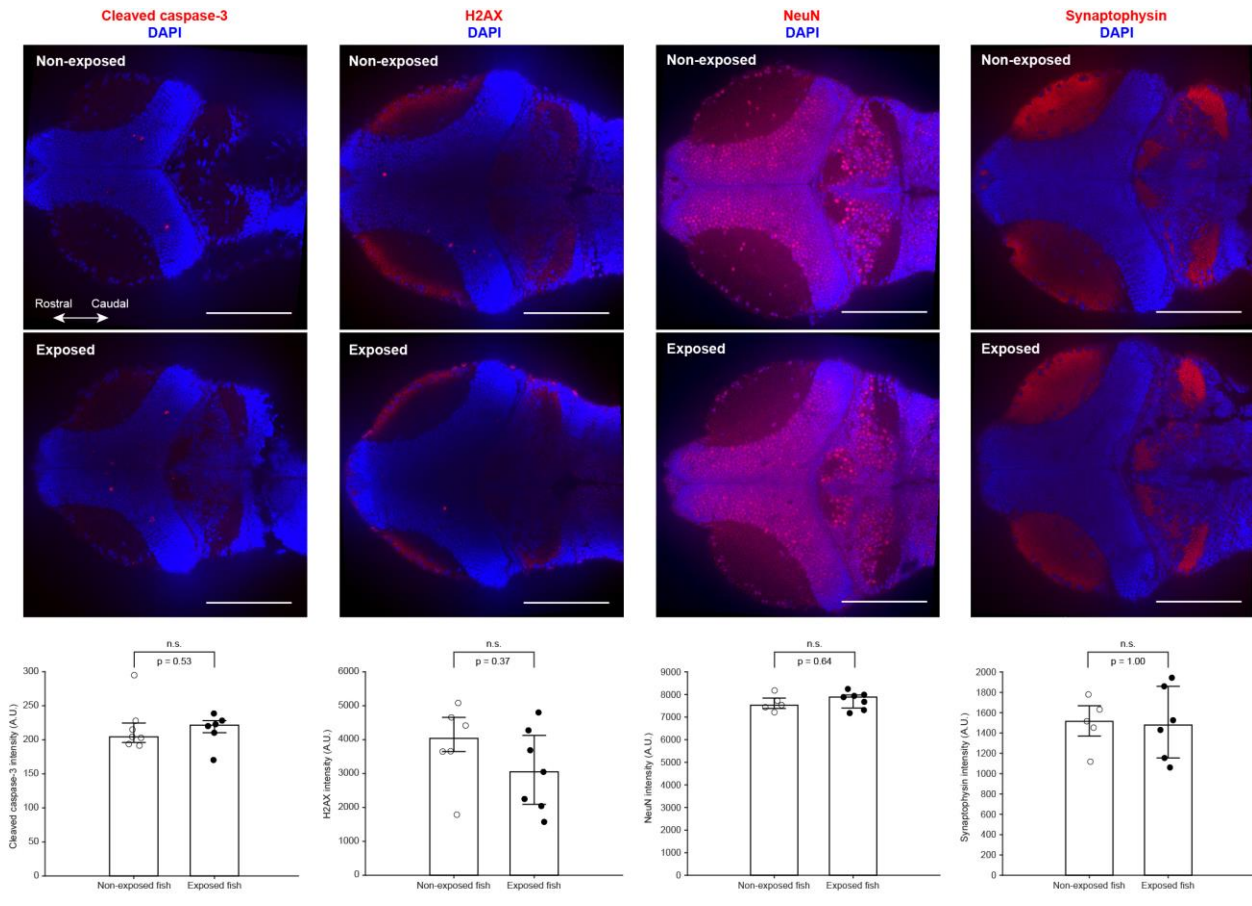
1985 **Figure S17. Schematic diagram of the excitation light path.** (a) Excitation light path (configuration 1)  
1986 without light-sheet pivoting capability. A collimated laser illuminated from the right side, first passing  
1987 through a Powell lens and then a pair of relay lenses (RL1, RL2). After being deflected by the galvo scanner,  
1988 the excitation light passed through a scan lens (SL) to form an enlarged light sheet near its focal plane. This  
1989 enlarged light sheet finally passed through a  $0.25\times$  microscope composed of a tube lens (TL) and a  $4\times$   
1990 objective lens, to illuminate the sample. We placed an optical mask at the scan lens's focal plane to prevent  
1991 the excitation light from directly entering the fish's eye. (b) Excitation light path (configuration 2) with  
1992 light-sheet pivoting capability for stripe artifact removal. This configuration is in general the same as  
1993 configuration 1, except that 1) a resonant mirror scanner was inserted between the relay lenses (RL3, RL4)  
1994 to pivot the light sheet in the focal plane, 2) the galvo scanner had a larger aperture (10mm diameter) to  
1995 deflect the excitation light that was rapidly scanned by the resonant scanner across  $\sim 8$  mm range on the  
1996 galvo scanner, 3) the illumination objective was changed from a Nikon 4x lens ( $f=50\text{mm}$ ,  $\text{NA}=0.2$ ) to an  
1997 Olympus 4x lens, which has a smaller focal length (45mm) and larger numerical aperture ( $\text{NA} = 0.28$ ), 4)  
1998 the relay lenses had different focal lengths (RL3,  $f=100\text{mm}$ , RL4,  $f=75\text{mm}$ ) to match the aperture size of  
1999 the resonant mirror scanner, and 5) an adjustable slit was added between the galvo and RL3 to control the  
2000 thickness and divergence of the light sheet. A top view of the resonant scanner part of the light path,  
2001 including the resonant scanner, the relay lens pair, and the Powell lens, is in the dashed box on the right  
2002 side of the panel.

2003

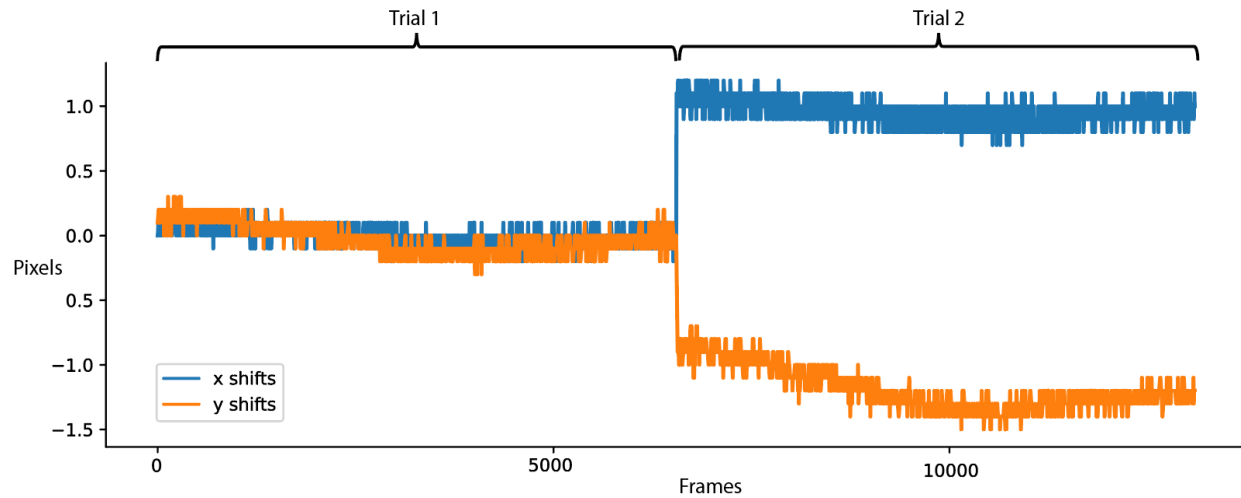


2004

2005 **Figure S18. Performance of our automatic ROI segmentation model.** (a) The segmentation results for  
2006 a randomly selected single z-layer (out of 30) from a single unlabeled fish. The ROI contours (light purple  
2007 lines) are overlaid on the image. A magnified view of the orange boxed area is shown in the top right corner.  
2008 Scale bar: 100  $\mu$ m. (b) Segmentation performance of the model on an entire fish. Blue bar: the number of  
2009 ROIs labeled by the model; orange bar: the number of ROIs added by the experimenter, indicating ROIs  
2010 that the model missed; green bar: the number of ROIs deleted by the experimenter, indicating ROIs that the  
2011 model falsely labeled. Z-layers are numbered according to their spatial depth in the brain. Smaller numbers  
2012 correspond to deeper layers. (c) On average, the experimenter added  $80.2 \pm 27.5$  ROIs (mean  $\pm$  standard  
2013 deviation, n=30 layers) and removed  $10.9 \pm 9.4$  (mean  $\pm$  standard deviation, n=30 layers) ROIs from the  
2014 model's output.



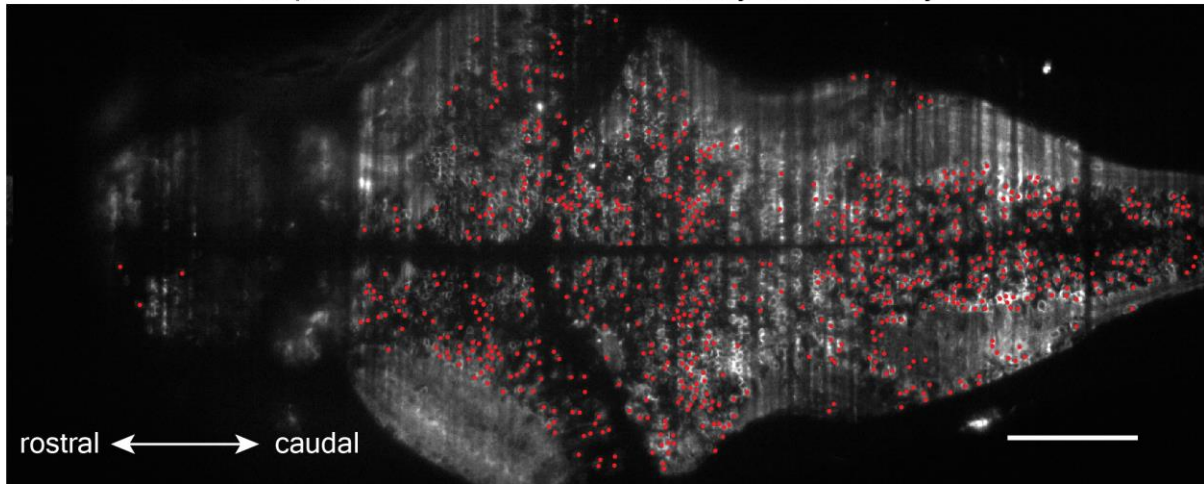
**2016** **Figure S19. Light-sheet exposure as in our voltage imaging experiments did not alter the levels of**  
**2017 four markers in fish brains.** Each column corresponds to a specific cellular and/or synaptic health marker:  
**2018** the apoptotic marker cleaved caspase-3, the DNA damage marker H2AX, the neuronal nucleus marker  
**2019** NeuN, and the synaptic marker synaptophysin, as we have used in previous neurotechnology safety studies  
**2020** (Linghu et al. 2020; Grossman et al. 2017). At the top of each column, representative single-plane  
**2021** immunostaining images display the markers (red) and nuclear DAPI staining (blue) in the brains of exposed  
**2022** fish and non-exposed fish. At the bottom, bar plots show the marker intensities between exposed and non-  
**2023** exposed fish. For the non-exposed and exposed groups in each column, from left to right, n = 7,6,6,7,5,7,5,6  
**2024** fish, respectively. No significant differences were observed for any marker, as determined by the Wilcoxon  
**2025** rank-sum test. n.s., not significant. P-values for each test are provided. Scale bar: 100  $\mu$ m.  
**2026**



2027

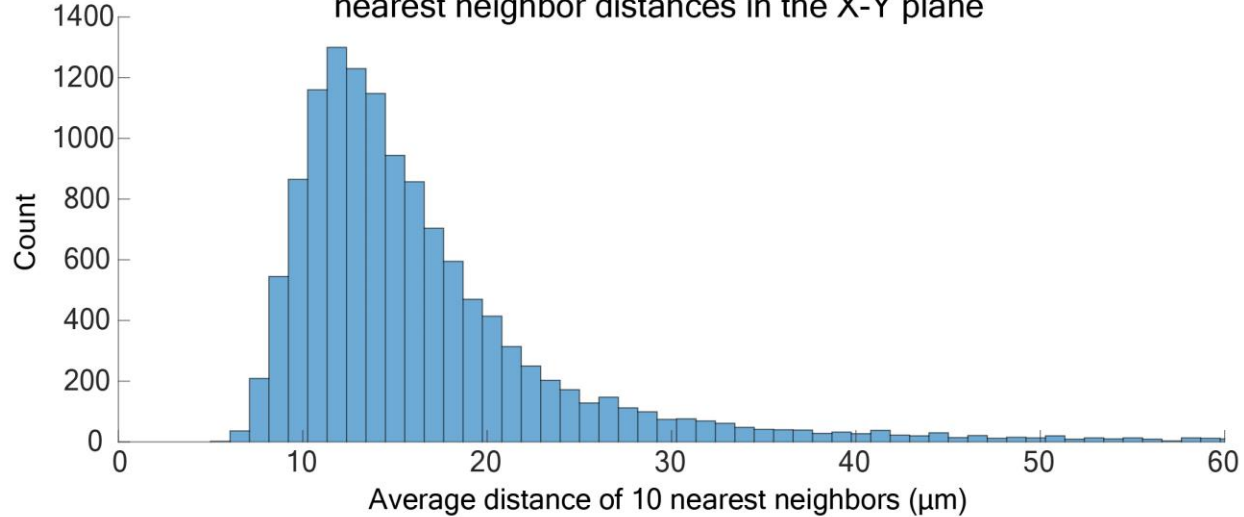
2028 **Figure S20. Motion correction result for a randomly selected brain layer.** The corrected drift in at each  
 2029 layer, as measured by the motion correction algorithm NoRMCorre (Pnevmatikakis and Giovannucci 2017),  
 2030 within an imaging trial (35 s) was less than 1 pixel (0.73  $\mu$ m), and the drift between two trials was < 2  
 2031 pixels. To align the neuron positions of two trials, trial 2 used the first frame of trial 1 as reference for  
 2032 motion correction. The abrupt changes of the curves at the start of trial 2 reflect a slight drift of the sample  
 2033 in x and y axes during the 20-min dark session between the two trials.

a Locations of putative neurons of a randomly selected layer in Fish A



b

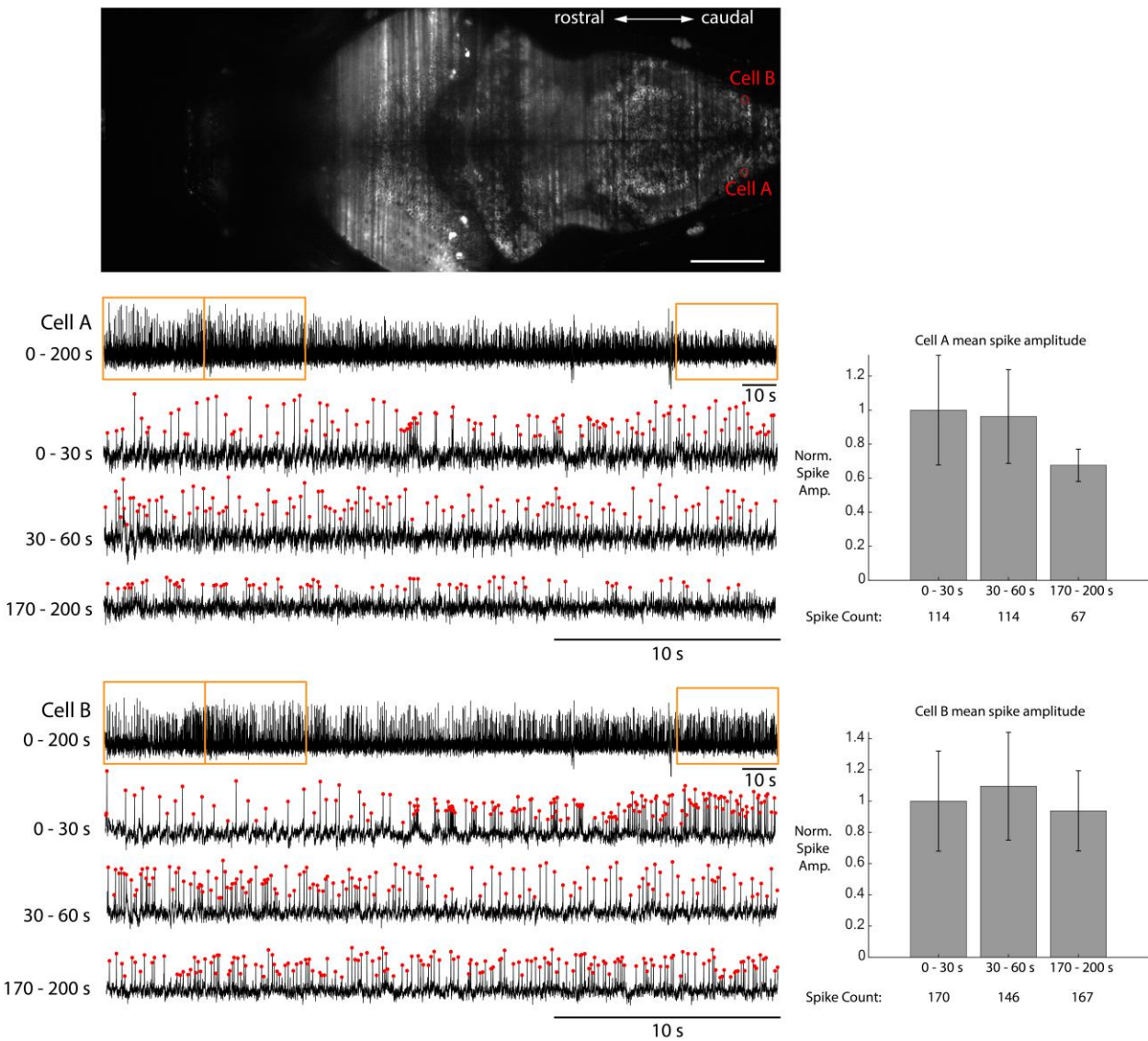
Histogram of all putative neurons' nearest neighbor distances in the X-Y plane



2034

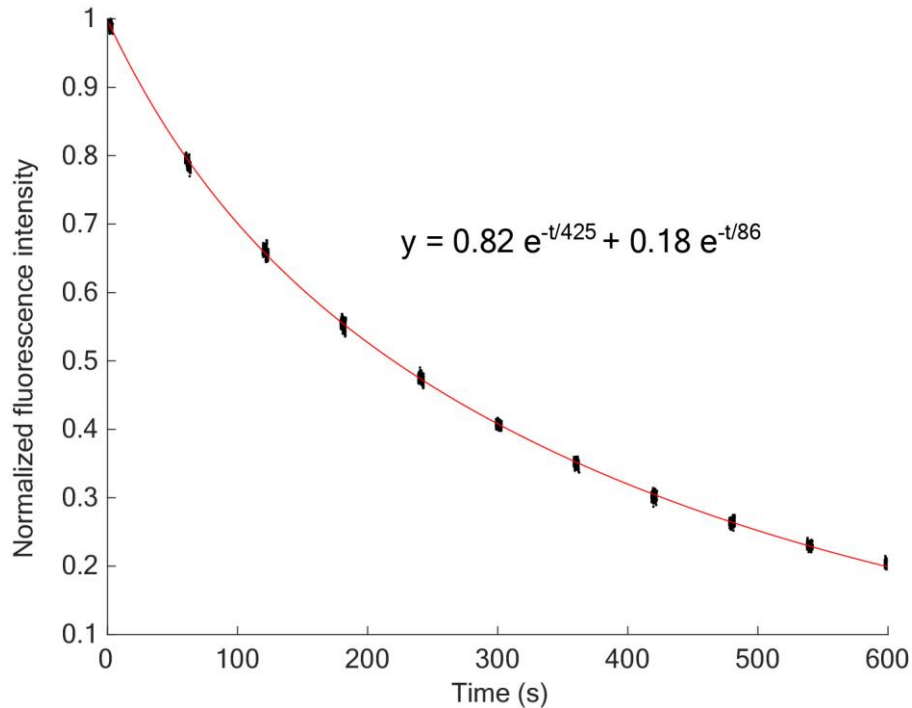
2035 **Figure S21. A quantification of putative neuron density across the x-y planes in Fish A.** We calculated  
2036 the average distance of each putative neuron's centroid to its 10 nearest neighbors' centroids along the X-  
2037 Y directions within 30 individual z-planes of Fish A. The average distance was  $17.8 \pm 15.2 \mu\text{m}$  (mean  $\pm$   
2038 SD, n = 12935 neurons). (a) The locations of putative neurons (red dots) of a randomly selected layer in  
2039 Fish A are shown. Scale bar: 100  $\mu\text{m}$ . (b) Histogram illustrating the counts of putative neurons in Fish A,  
2040 categorized by their mean distances to the ten nearest neighboring ROIs.

2041



2042

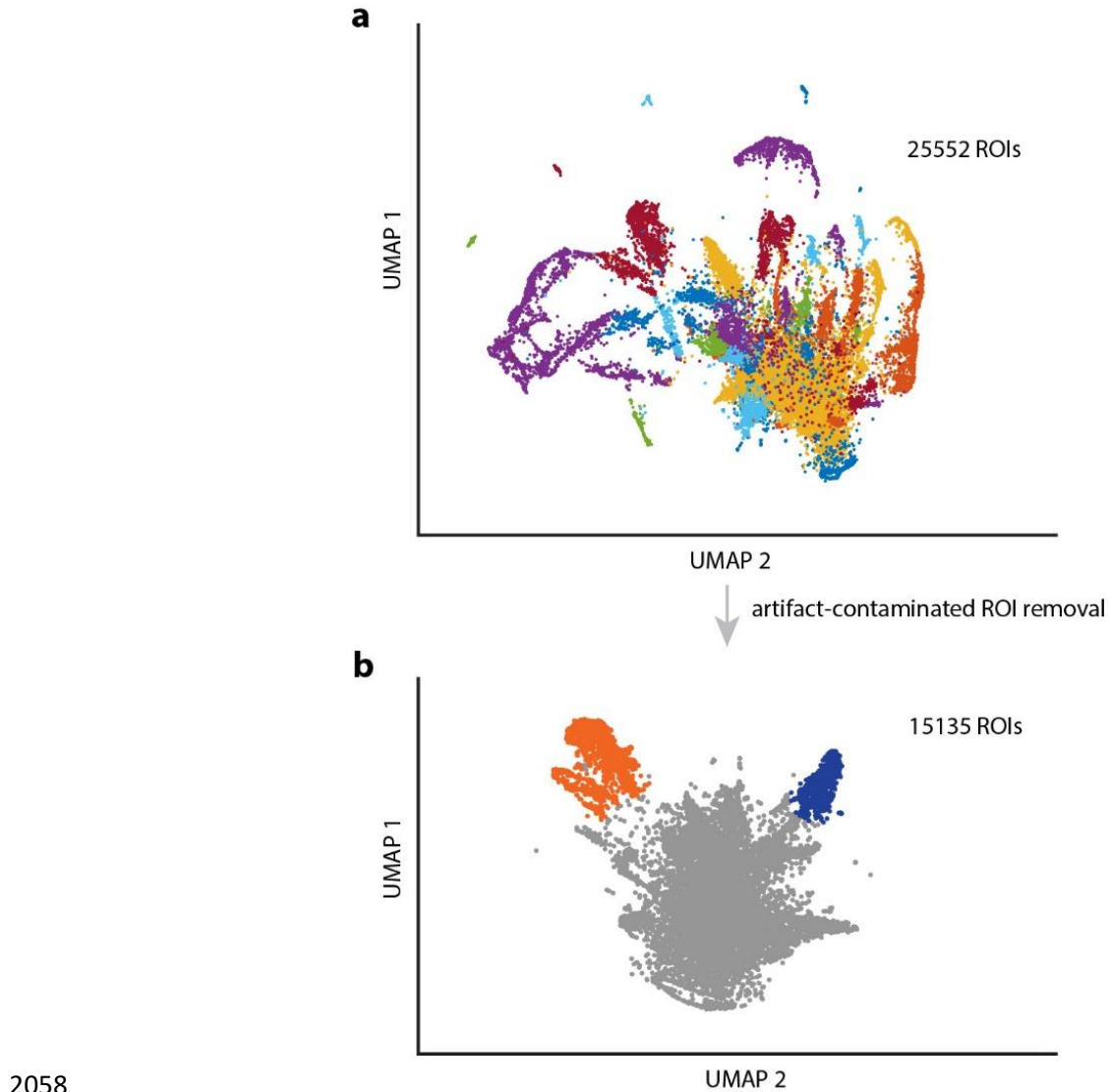
2043 **Figure S22. Voltage activity from a 200-s long imaging trial.** The top panel displays a raw image of a  
 2044 randomly selected brain layer (out of a total of 30), with two cells (Cell A and Cell B, arbitrarily selected)  
 2045 marked for neural trace analysis. Below, the full 200-s neural traces of Cell A and Cell B are shown. The  
 2046 first 60 s and the last 30 s of the traces (highlighted with orange boxes in the top trace) are displayed with  
 2047 expanded time scales. Red dots show spikes detected by VolPy. On the right side of the neural traces, bar  
 2048 plots display the spike counts and normalized mean spike amplitudes  $\pm$  standard deviations for each section  
 2049 (0-30s, 30-60s, and 170-200s). Scale bar in the top panel: 100  $\mu$ m.



2050

2051 **Figure S23. Normalized photobleaching curve of a zebrafish brain expressing Positron2-Kv indicator**  
 2052 **stained with JF525.** The fish brain was continuously illuminated by a 515-nm light sheet that was scanned  
 2053 at 200.8Hz, with a total average power of 10.4 mW. To save storage space, we recorded videos of the brain  
 2054 for 4.5 s at 1-min intervals. The measured fluorescent intensities averaged across the imaged brain volume  
 2055 at different time points were plotted as black dots, with a double-exponential fitted curve shown in red. The  
 2056 formula of the fitted curve was also shown.

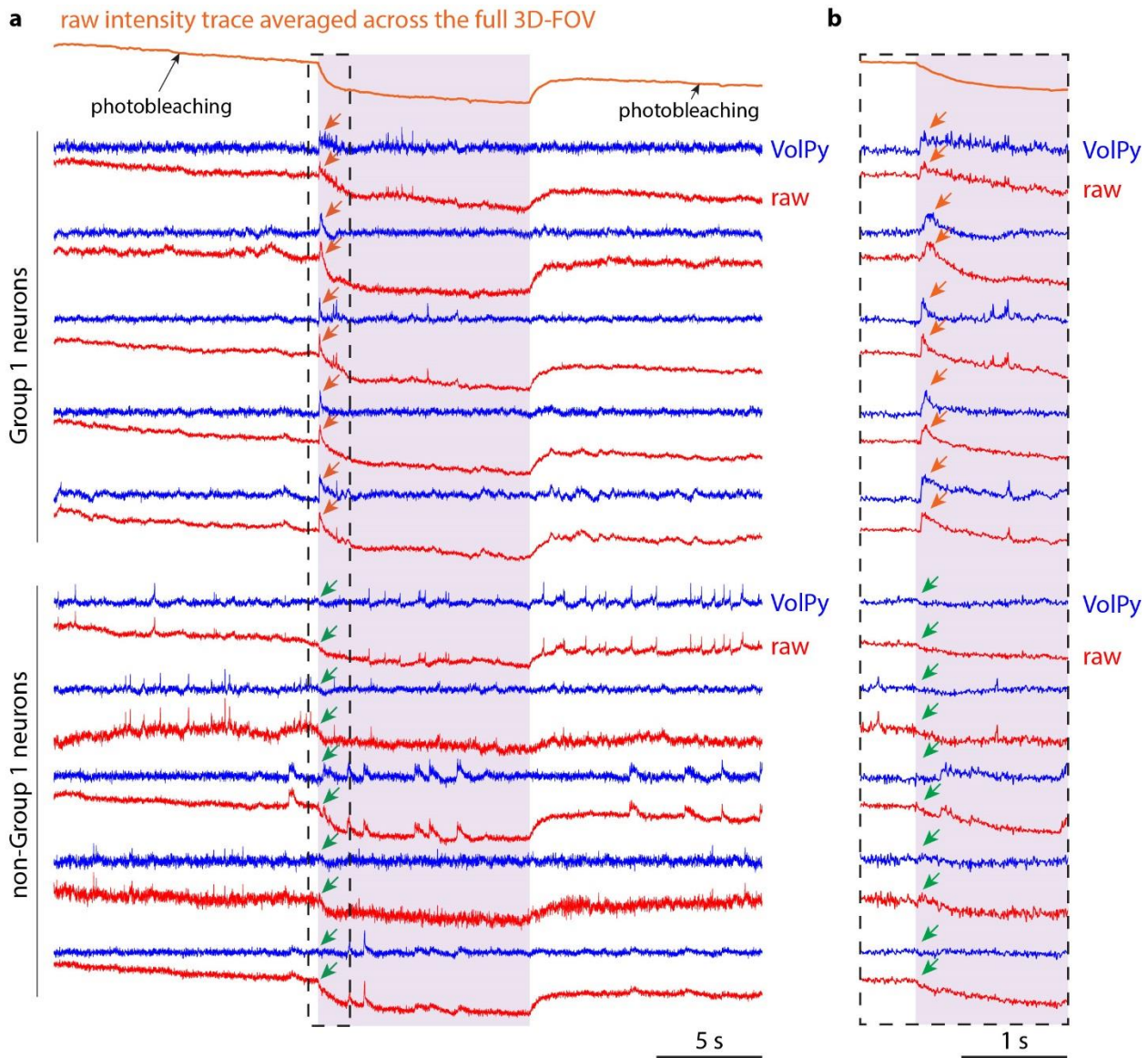
2057



2058

2059 **Figure S24. 2D UMAP visualizations of ROIs before and after the removal of artifact-contaminated**  
 2060 **ROIs in Fish B.** (a) 25552 ROIs were mapped into 2D space using the UMAP algorithm based on their  
 2061 temporal traces. Different colors represent different clusters. (b) After identifying and removing the ROIs  
 2062 whose temporal traces are contaminated by the stripe artifacts, 15135 ROIs remained and were considered  
 2063 as putative neurons. The putative neurons were then clustered into three groups (indicated in three colors)  
 2064 for subsequent analysis.

2065

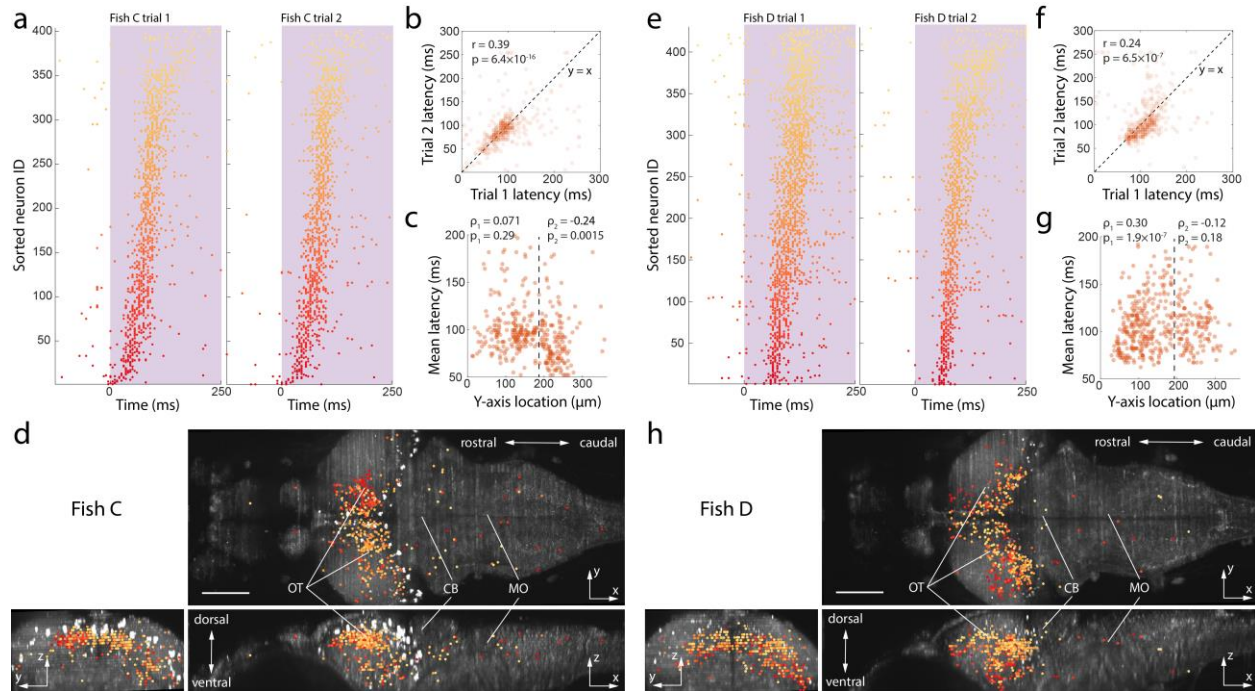


2066

2067 **Figure S25. Photoswitching effects in VolPy-extracted temporal traces, and raw temporal traces, of**  
 2068 **neurons in Group 1 (i.e., neurons that have increased activity in response to the onset of the light**  
 2069 **stimulus) and neurons not in Group 1. (a)** Comparison of the VolPy (blue) and raw (red) traces of neurons.  
 2070 Purple color indicates the period of light stimulus. Due to photoswitching effects of the voltage indicators,  
 2071 the fluorescence intensity of the whole zebrafish brain decayed upon the onset of the light stimulus, and  
 2072 recovered after the light stimulus was turned off (top of the panel, orange curve). For Group 1 neurons,  
 2073 following the light stimulus onset, increased activity (orange arrows) can be observed in both the raw  
 2074 temporal traces and the VolPy-extracted temporal traces. Other neurons have photoswitching induced  
 2075 fluorescent changes in their raw traces at the onset of the light stimulus, but do not show increased activity

2076 (green arrows). (b) Enlarged view of the dashed box in (a). For Group 1 neurons, a time delay can be  
 2077 observed between the onset of the light stimulus and their increased activity (orange arrows).

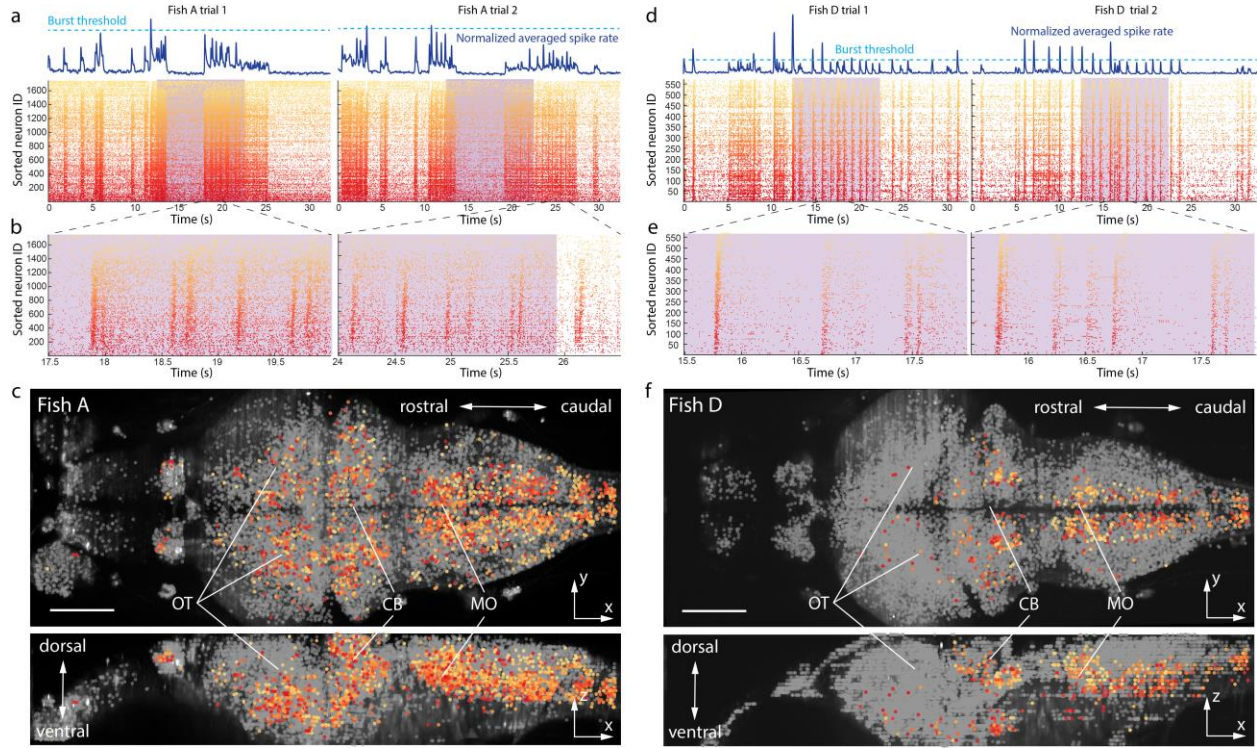
2078



2079

2080 **Figure S26. Spatial mapping of neurons' firing at different times in stimulus-evoked sequences in**  
 2081 **Fish C and Fish D. (a)** The sequential order of Fish C's Group 1 neurons' peak rate in trial 1 is similar in  
 2082 trial 2. Neuron IDs are sorted based on their peak spiking rate latencies averaged across trials 1 and 2. **(b)**  
 2083 Fish C Group 1 neurons' peak spiking rate latencies for trial 1, measured relative to UV onset, have a  
 2084 positive correlation with those of trial 2, as determined by Pearson's correlation ( $r$  and  $p$  values provided). **(c)**  
 2085 Neuron firing latency vs. neuron location along the y-axis (left lateral to right lateral in the brain). During  
 2086 UV stimulus, neurons located more laterally fire earlier than neurons located more medially. The dashed  
 2087 line represents the midline separating the left and right lateral halves of the brain. Spearman's rank  
 2088 correlation was conducted independently for the left and right halves, with  $\rho$  and  $p$  values provided. **(d)**  
 2089 Group 1 neurons' spatial positions color coded by their firing latency. The majority of Group 1 neurons are  
 2090 located on the lateral-left side of the optic tectum. OT: optic tectum. CB: cerebellum. MO: medulla  
 2091 oblongata. Scale bar: 100  $\mu\text{m}$ . **(e-h)** same as (a-d) for Fish D.

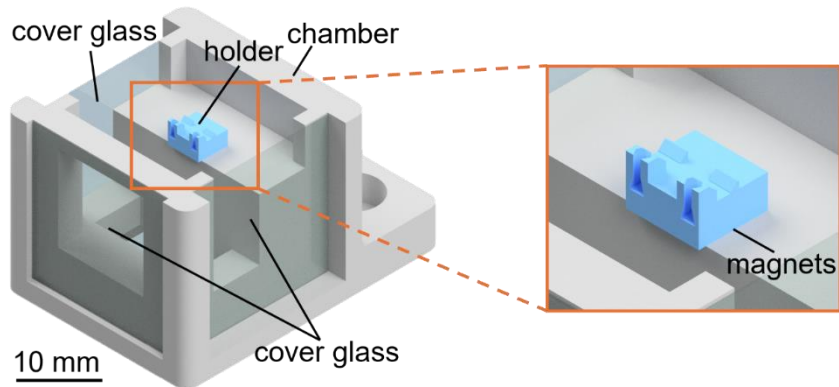
2092



2093

2094 **Figure S27. Spatial mapping of the timing of activity within burst sequences, across the brains of Fish**  
 2095 **A and Fish D.** (a) Raster plot showing bursting in Group 2 neurons during the light stimulation  
 2096 experiments in Fish A. We define a burst as a period when the average spike rate, taken over an interval of  
 2097 70 ms, is larger than 5 times the mean spike rate, over the whole trial. The start of each burst was defined  
 2098 as the first time point in the burst when the average spike rate surpassed this threshold. Neurons were sorted  
 2099 by their activation timing, averaged across all burst events. The two trials were separated by a 20 min dark  
 2100 session. The UV stimulus period is indicated in purple. (b) Magnified views of the boxed areas in (a),  
 2101 illustrating a consistent sequence of neural activation during bursts. This sequential order is color-coded  
 2102 from deep red (early) to light orange (late). (c) 3-D locations of neurons from (a), superimposed on the  
 2103 dorsal (top) and lateral (bottom) brain views (MIPs) of Fish A. The neuron firing sequence is color-coded  
 2104 using the same gradient of colors as in (b). OT: optic tectum. CB: cerebellum. MO: medulla oblongata.  
 2105 Scale bar: 100  $\mu$ m. (d-f) same as (a-c) for Fish D.

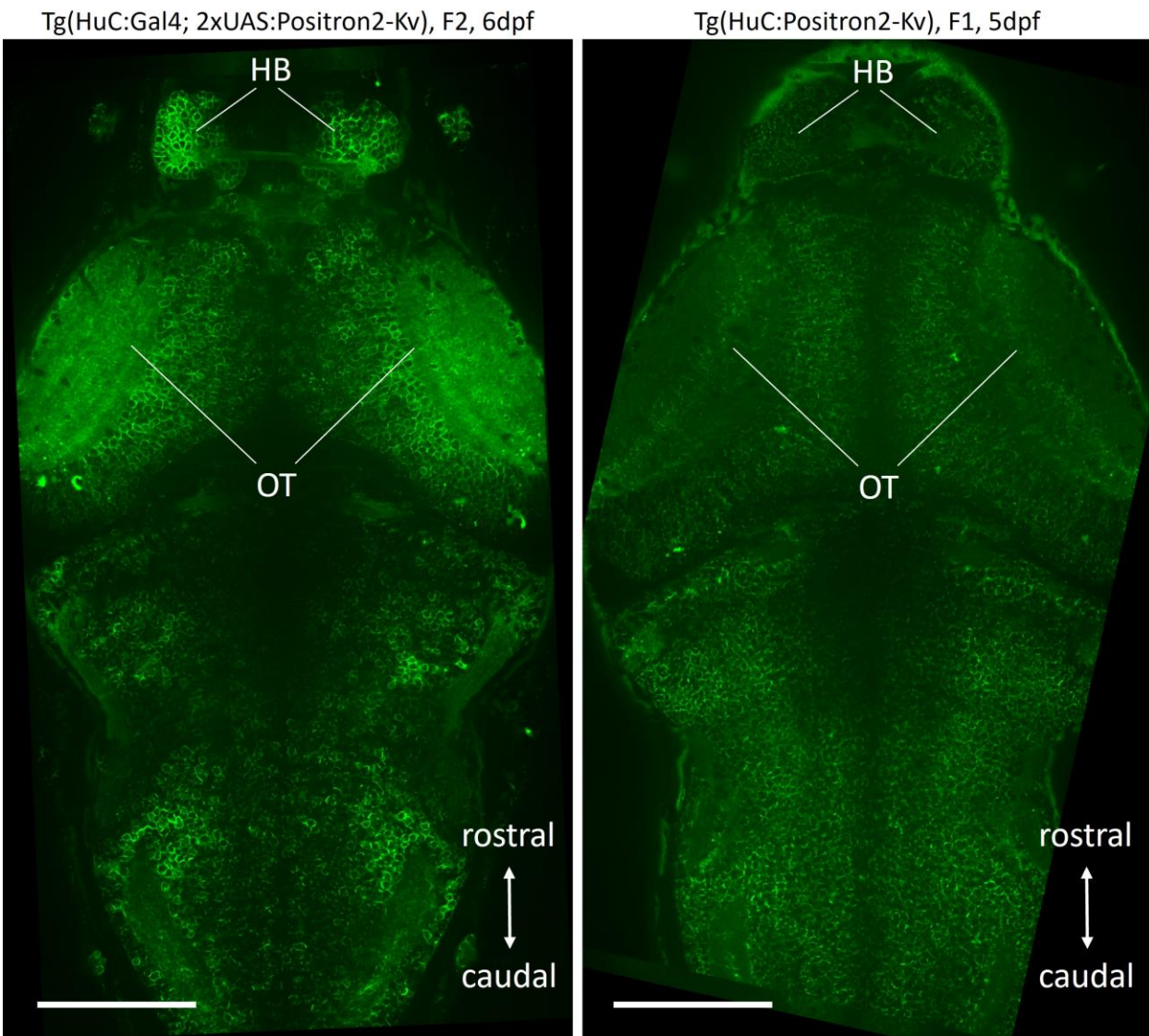
2106



2107

2108 **Figure S28. Illustration of the fish holder (blue) and chamber (gray).** The holder was attached to the  
2109 chamber using two magnets. There were two slots on the holder where the fish could be mounted, depending  
2110 on which side the light sheet came from.

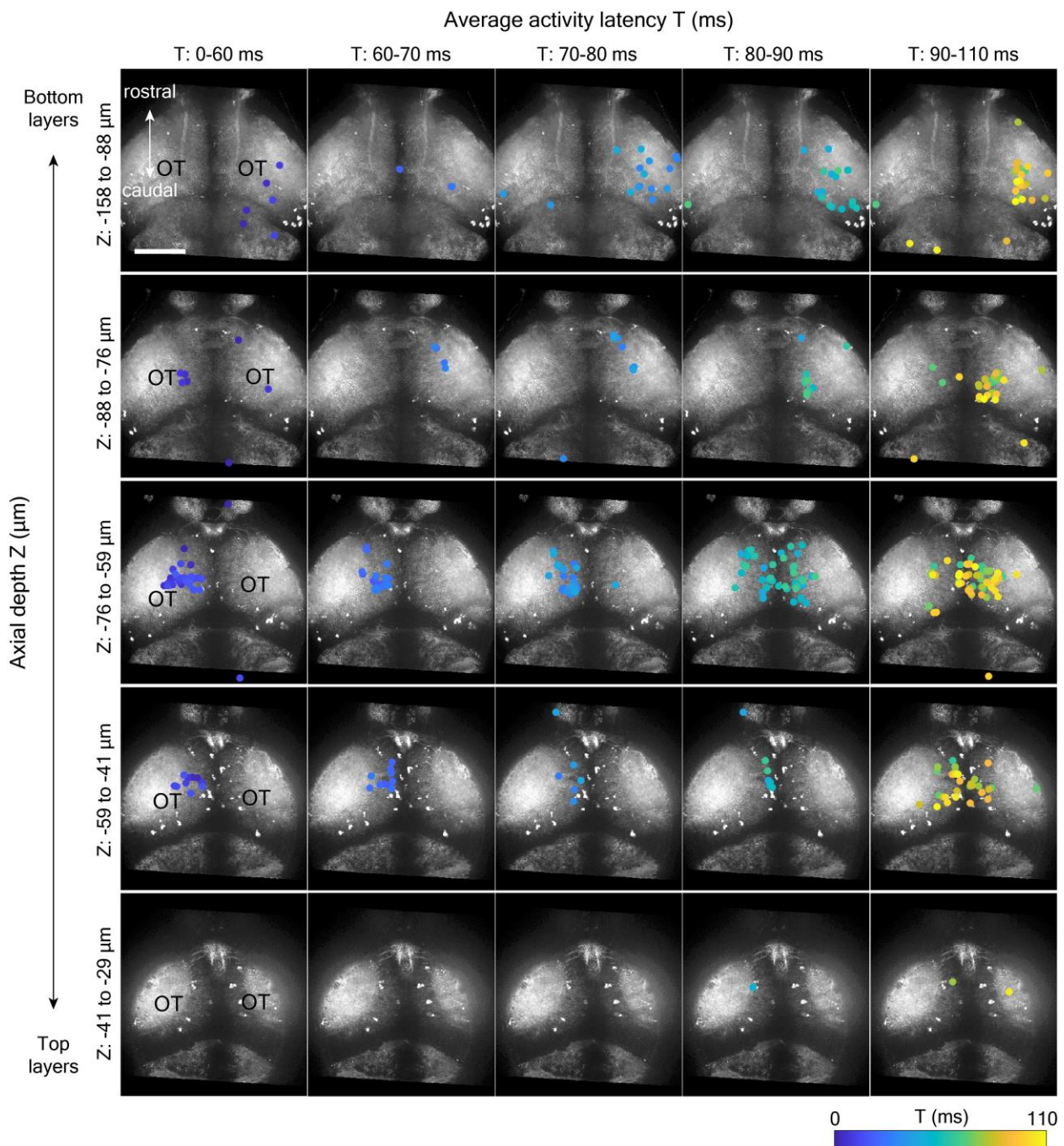
2111



2113 **Figure S29. Comparison of Positron2-Kv expression in zebrafish brains using different promoters.**  
 2114 Confocal microscopy images of zebrafish brains expressing Positron2-Kv using Gal4/2×UAS (left, F2  
 2115 generation at 6 dpf) and HuC (right, F1 generation at 5 dpf) promoters. Images were acquired using the  
 2116 same microscope settings and displayed using the same intensity scale. OT: optic tectum. HB: habenula.  
 2117 Scale bar: 100 μm.

2118

2119



2120

2121 **Figure S30. Locations of Fish C's UV-responding neurons (Group 1 neurons) overlaid with confocal**  
 2122 **images of the optic tectum region.** Each row shows a z-section of the brain of a certain depth range, as  
 2123 indicated on the left of the row. Within each row, from left to right, neurons falling within different activity  
 2124 latency windows (indicated on top of each column) are shown. The depth ranges and latency windows were  
 2125 chosen arbitrarily to better visualize the spatial-temporal correlations of UV-elicited neural activity.  
 2126 Neurons are plotted as dots in colors coded by their activity latency. The bright white dots are occasional

2127 neurons, visible in these z-projections but found here and there in all fish, with very high expression levels  
2128 of GEVIs, for unknown reasons. OT, optic tectum. Scale bar: 100  $\mu$ m.

2129

2130 **SUPPLEMENTARY VIDEOS**

2131 **Supplementary Video 1. A representative stripe artifact (shown in Figure S10).** The light sheet  
2132 illuminates the sample from the left side (green arrow). The location of the stripe artifact is indicated by  
2133 the white arrows. Scale bar: 100  $\mu$ m.

2134 **Supplementary Video 2. BDM treatment removed moving stripes in the live zebrafish brain (shown  
2135 in Figure S14b).** This video shows the raw light-sheet recordings of four randomly selected planes (out of  
2136 30) of the same zebrafish brain during a BDM-treatment experiment. The fish had pan-neuronal Positron2-  
2137 Kv expression and was imaged at 6dpf. Moving stripes that were visible before BDM treatment (pre-BDM)  
2138 disappeared after the BDM treatment (post-BDM). After the fish recovered in fresh water (recovered), the  
2139 moving stripe patterns appeared again. Green arrows on the left side indicate the direction of light-sheet  
2140 illumination. Scale bar: 100  $\mu$ m.